Design, Analysis, Prototyping, and Evaluation of a Robotic System for Remote Ultrasound Diagnosis

by

Farshid Najafi

A Thesis submitted to the Faculty of Graduate Studies of

The University of Manitoba

in partial fulfilment of the requirements of the degree of

Doctor of Philosophy

Department of Mechanical and Manufacturing Engineering

University of Manitoba

Winnipeg, Manitoba, Canada

THE UNIVERSITY OF MANITOBA

FACULTY OF GRADUATE STUDIES

*****

COPYRIGHT PERMISSION

Design, Analysis, Prototyping, and Evaluation of a Robotic System for Remote Ultrasound Diagnosis

By

Farshid Najafi

A Thesis/Practicum submitted to the Faculty of Graduate Studies of The University of Manitoba in partial fulfillment of the requirement of the degree

Of

Doctor of Philosophy

Abstract

This thesis presents design, analysis, prototyping, and performance evaluation of a robotic system to assist physicians to perform ultrasound examinations on patients located in remote areas. The research is inspired by the desire that uniform healthcare should be available to all citizens including those living in remote and isolated areas with less access to medical experts. The system, presented in this thesis, consists of a force-reflecting hand-controller located at the physician side, and a robotic wrist located at the patient side. The physician manipulates the hand-controller to control the position of the robotic wrist holding an ultrasound probe on the patient's body. The physician observes captured ultrasound images while feeling the palpation forces between the remote probe and the patient's body.

The robotic wrist utilizes a novel combination of asymmetric parallel mechanisms, universal telescoping joints, ball screws, cable drives, and ball splines. The unique characteristics of the device are: kinematically decoupled degrees of freedom, one-to-one position correspondence with the corresponding haptic device to make the usage of the system intuitive and to reduce physician's training time, singularity-free workspace (a conical workspace with a vertex angle as much as 50°), base-mounted actuators to reduce inertia and simplify device sterilization, and remote center-of-motion to facilitate three dimensional ultrasound imaging. The weight of the moving elements is 2.5 kg. The sliding motion of the wrist is able to apply palpating forces up to 24 N. The maximum velocities of the ultrasound probe during examination for pitch, yaw, rotational, and palpating motions are 27 deg/s, 32 deg/s, 68 deg/s, and 3 mm/s, respectively.

The hand-controller consists of symmetric parallel mechanisms, universal joints, and miniature cable drives. The novel characteristics of the device are: static balancing with a tension spring to reduce operator's fatigue and to enhance the safety of remote examination, kinematically decoupled degrees of freedom each corresponding to a motion of the ultrasound probe, large and singularity-free workspace (a conical workspace with a vertex angle as much as 50°), base-mounted actuators, and fixed center-of-motion to enhance operator's performance. The weight of the moving elements is 452 gr.

In collaboration with Winnipeg Children Hospital, an ultrasound technologist successfully performed ultrasound imaging of kidney, heart, spleen, and liver using the robotic devices developed in this thesis.

Acknowledgements

First, I would like to express my sincere gratitude to my advisor, Professor Nariman Sepehri, whose support, and encouragements over the years of graduate studies have made this work possible.

I would like to thank to Professors Witold Kinsner, Pourang Irani, Qingjin Peng, Wai-Keung Fung, and Brian Surgenor (external examiner) as my committee members, for the time they spent reading and examining this thesis. Their valuable suggestions helped significantly improve the quality of my work.

I wish to sincerely thank the technical support of Mr. Stan Gebczyk for constructing the prototypes system. I am very grateful to Mr. Sam Aminian of the Children's Heart Centre in Winnipeg, Manitoba for his time and expertise in performing ultrasound diagnostic evaluations using the developed prototype system.

I would like to thank the University of Manitoba for Graduate Fellowship, the Institute of Robotics and Intelligent System (IRIS) Network Centre of Excellence, Precarn, Canadian Space Agency, Manitoba TeleHealth, and Technology Transfer Office of the University of Manitoba who provided financial support for this thesis.

My thanks also go to my lab-mates and friends Dr. Mark Karpenko, Mr. Ehsan Jalayeri, Dr. Ali Reza Forouzesh, and Dr. Reza Ghorbani for their supports. I have always enjoyed our daily technical discussions.

My deepest gratitude goes to my wife, Dr. Niloufar Choubdar, for her love, devotion, support, and encouragements. No word describes my heartfelt thanks to my mother, Leila Khalaj Hedayati, my father, Najaf Najafi, and my brother, Dr. Farid Najafi for a long-life of support and encouragements.

Dedication

To My wife, mother and father, with love

Table of Contents

List of Figures

List of Tables

List of Abbreviations

RCM Remote center-of-motion

FCM Fixed center-of-motion

DoF Degree of freedom

RMS Root mean square

List of symbols

$\{X_0Y_0Z_0\}$: fixed coordinate system

$\{X_1Y_1Z_1\}$: moving coordinate system

$\{X_2Y_2Z_2\}$: moving coordinate system

$\{X_mY_mZ_m\}$: moving coordinate system attached to ultrasound probe or hand-grip

β_1: angle between Z_0 and Z_1

u_{Z_0}: unit vector along Z_0

u_{Z_2}: unit vector along Z_2

β_2: angle between Z_1 and Z_3

X_t: axis of pantograph input link

Y_t: axis of pantograph input link

$S(s_x, s_y, s_z)$: unit vector normal to X_t and Z_1

α: angle between X_t and X_0

r: radial displacement of ultrasound probe

$\theta_1 = \theta_1^m$: rotational angle of wrist's motor about axis X_t

$\theta_2 = \theta_2^m$: rotational angle of wrist's motor about axis Y_t

θ_3: rotational angle of ultrasound probe about its axis

θ_4: rotational angle that provides radial displacement of probe

θ_3^m: rotational angle of wrist's motor which provides rotation of probe

θ_4^m: rotational angle of wrist's motor to provide radial displacement, r, of probe

$T_{4\times4}$: homogenous transformation matrix between frames $\{X_0Y_0Z_0\}$ and $\{X_mY_mZ_m\}$

b_{ij}: elements of homogenous transformation matrix $T_{4\times4}$

ϕ_1: deflection angle of upper universal joint of universal telescoping joint

ϕ_2: deflection angle of lower universal joint of universal telescoping joint

ψ: angle between ultrasound probe axis and Z_0

n: number of starts on ball screw

P: pitch of ball screw

$[\vec{\omega}\ \vec{\mathrm{V}}]$: velocity state of ultrasound probe described in $\{X_0 Y_0 Z_0\}$

$[J]_{(6\times 4)}$: Jacobian matrix of robotic wrist and haptic device

$\dot{\theta}_1^m$: rotational velocity of wrist's motor about axis X_t

$\dot{\theta}_2^m$: rotational velocity of wrist's motor about axis Y_t

$\dot{\theta}_3^m$: rotational velocity of ultrasound probe about its axis

$\dot{\theta}_4^m$: rotational velocity of wrist's motor to provide radial velocity, $\dot{r}$, of probe

I: inertia matrix of prototyped wrist

K_p: proportional controller gain

K_v: derivative controller gain

K: spring stiffness for haptic static balancing

I_i $(\mathrm{i}=1,2)$: area moment of inertia

I_{ixx} (i=1,2): mass moment inertia of beam

E: modulus of elasticity

b_i $(i=1,2)$: width of beam

h_i $(\mathrm{i}=1,2)$: height of beam

ω_n: open-loop mechanical bandwidth

ω_{in} $(\mathrm{i}=1,2)$: open-loop mechanical bandwidth of beam

m_i $(i=1,2)$: mass of beam

θ_1^m: rotational angle of haptic's motor about X_0

θ_2^m: rotational angle of haptic's motor about Y_0

θ_3^m: rotational angle of haptic's motor about Z_0

θ_4^m: rotational angle of hand-grip about Z_m

$\dot{\theta}_1^m$: rotational velocity of first eight-bar mechanism about axis X_0

$\dot{\theta}_2^m$: rotational velocity of second eight-bar mechanism about axis Y_0

$\dot{\theta}_3^m$: rotational velocity of hand-grip about its axis

$\dot{\theta}_4^m$: rotational velocity of haptic's motor to provide radial velocity, $\dot{r}$

θ_3^r : output position of cable reducer

θ_3^u : output position of universal joint

r : radial displacement of hand-grip

$\dot{r}$: radial velocity of hand-grip

ψ : deflection angle of universal joint in haptic device

β : angle between Z_1 and Z_2

t_{ij} : elements of homogenous transformation between $\{X_0Y_0Z_0\}$

n : cable reduction ratio of haptic device

d_3 : diameter of driver pulley in haptic device

T_3^m : motor torque of haptic device

T_3^r : output torque of cable reducer of haptic device

T_3^u : output torque of universal joint of haptic device

F_3 : applied force to user's hand along the axis of hand-grip

d_1 : diameter of pulley connected to motor

d_2 : diameter of pulley connected to the input shaft of the universal joint

d_3 : diameter of the driver pulley of the cable drive

d_4 : diameter of the driven pulley of the cable drive

T_1 : high tension force of cable reducer

T_2 : low tension force of cable reducer

F_1 : high tension force of cable drive

F_2 : low tension force of cable drive

A : cross section of cable

μ : coefficient of friction in cable-pulley assembly

γ_r : wrap angle of cable reducer

γ_f: wrap angle of cable drive

$\Delta\theta_3^u$: angular position error due to universal joint

$\Delta\theta_3^r$: angular position error due to cable reducer

$\Delta\theta_3^{total}$: total position error

η: relative output force error

$F_{surface}$: surface force

K: virtual surface stiffness

B: virtual surface damping

α: force coefficient to provide surface force when penetrating inside surface

β: damping ratio to remove surface force when moving away from surface

Chapter 1

Introduction

This Chapter presents a background on medical ultrasound imaging, and highlights the need for providing ultrasound examination services for people in remote areas. It then presents a survey on existing robotic systems for remote ultrasound imaging, and challenges remained in the design of more improved systems. Thesis objectives and scope are outlined last.

1.1 Motivation

This work was motivated by the fact that uniform healthcare should be available to all citizens. The most advanced medical equipments and professionals are generally located in large urban hospitals. Under the current situation, access to medical experts for patients living in sparsely populated areas often results in inconvenience and/or inefficient use of medical resources. Although, a wide variety of patient's vital parameters such as blood pressure, temperature, heart, and respiration rates can be measured by an on-site nurse, accurate assessment of many clinical conditions such as interpretation of the abdominal pain must be conducted by an experienced clinician. Ultrasound examination offers quick and reliable non-invasive diagnosis. However, the main drawback of the current ultrasound techniques is that the quality of the examination is highly dependent on the operator's skills, which are often lacking in small medical centers and isolated areas. Most commonly, patients travel to see a medical expert at the urban hospitals, which takes hours of travel for a relatively short examination.

Remote examination is a promising approach for addressing some of the issues associated with the problem of distance between the patients and clinicians. It offers the advantage of cost-saving, availability of expertise, remote accessibility and timeliness. Remote examination has so far been implemented mainly as consultation. It includes the ability to observe, talk, and listen to patients, or to read ultrasound images taken from a patient located in a remote clinical center. Remote examination could further employ robotic devices to enable clinicians to manipulate diagnostic tools such as an ultrasound probe. This thesis aims to develop a complete robotic system to enable physicians to perform ultrasound examinations on patients located in remote and isolated areas.

1.2 Medical Ultrasound Imaging

In scanning with ultrasound, high frequency sound waves are transmitted to the areas of interest and the returning echoes are recorded. In free-hand scanning, the physician, based on her/his experience and knowledge, manipulates the transducer on the patient's organ and mentally transforms the 2-D images into a 3-D tissue structure and makes the diagnosis (Figure 1-1). The main manipulation techniques consist of pitch, yaw, and rotational scanning fashions (see Figure 1-2) (Fenster and Downey 1996).

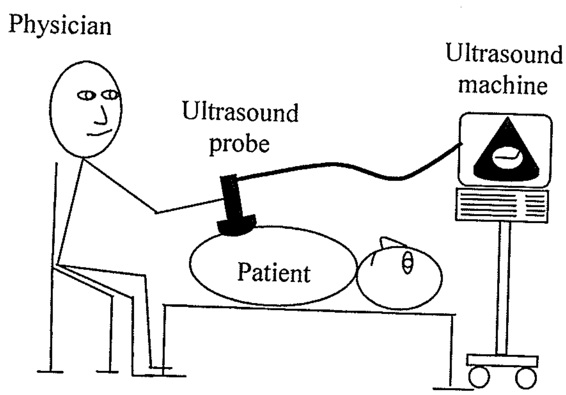

Figure 1-1. Conventional ultrasound imaging whereby physician and patient are at the same place.

In pitch and yaw scanning (Figures 1-2a and 1-2b), the transducer is pivoted on a point on the patient's body, and the physician moves the transducer in a circular motion about this point while maintaining the contact with the body. In rotational scanning, Figure 1-2c, the transducer rotates about its longitudinal axis. The combination of the three major motions generates a conical workspace in which the tip of the ultrasound probe is located at the cone vertex as remote center-of-motion (RCM). Studies by

Delgorge et al. (2005) showed that 60° vertex angle is adequate for most ultrasound examinations.

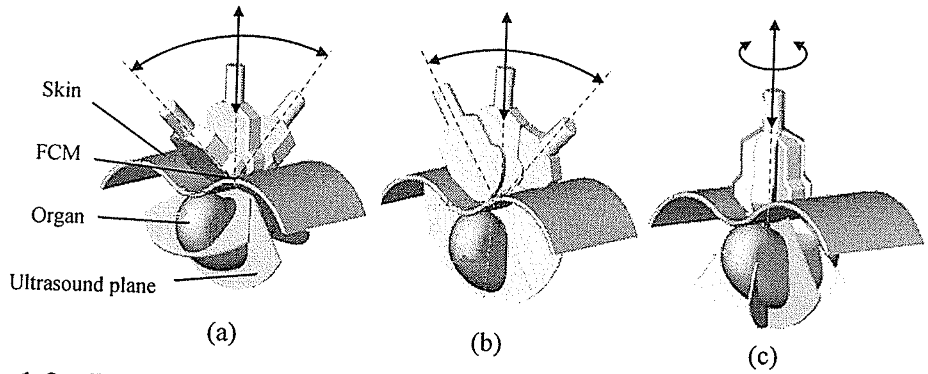

Figure 1-2. Free-hand ultrasound examination: (a) pitch scanning; (b) yaw scanning; (c) rotational scanning.

1.3 Remote Ultrasound Imaging

The elements of a system for remote ultrasound imaging are located in two sides: physician side and patient side. They are separated from each other by a distance barrier but connected together through a proper communication system such as Internet, satellite links, and fiber optics lines (Figure 1-3). The physician side consists of a physician, a force reflecting hand-controller (haptic device[1]) and display systems. The patient side includes a patient, a robotic arm, an ultrasound machine, and a camera. The physician and the patient can talk to, and see each other via voice and video links. The physician is able to manipulate the robotic arm holding an ultrasound probe via the haptic device to capture and observe desirable ultrasound images from an internal organ. The haptic device allows the physician to feel and adjust the interaction forces between remote probe and patient's body to maintain proper contact between probe and patient in order to achieve continuous and meaningful ultrasound images for diagnostic purposes.

Success in proper design and implementation of such a robotic system will offer a new solution to improve the availability of ultrasound examination services for people living in remote and isolated areas.

[1] Haptic device refers to devices which interface to the user via the sense of touch by applying forces, vibrations and/or motions to the user.

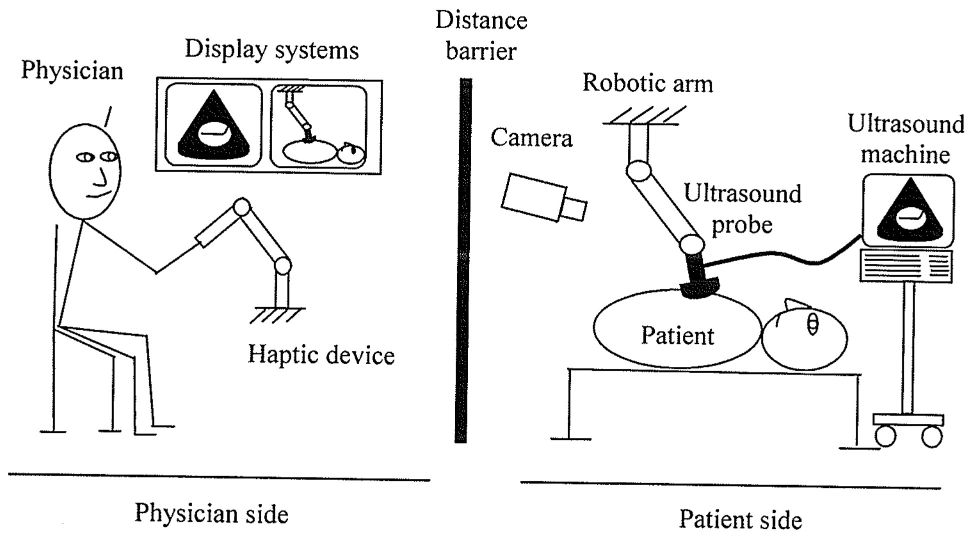

Figure 1-3. Remote ultrasound imaging using robotic system.

1.4 Survey on Existing Robotic Systems for Ultrasound Imaging

1.4.1 Robotic Wrist

A comprehensive study of robotic wrist designs for general purposes can be found in the book by Rosheim (1989). Selected wrist designs that are relevant to this thesis are reported here.

The wrist by Rosheim (1989) has 3 DoFs (degrees of freedom) with linear actuators. This provides spherical motion of an end-effector. However, its center-of-motion is inside the mechanism. For ultrasound imaging the center-of-motion should be located outside the mechanism.

The parallel wrist[2] by Vischer and Clavel (2000) provides a 3-DoF rotational motion about a fixed point. The mechanical design of the wrist offers simplicity of manufacturing due to placing all the joints of one kinematic chain in one plane. However, the fixed point is enclosed within the mechanism at some configurations which could result in having contact between the moving elements and the patient's body, if it is used

[2] A manipulator is said to be 'serial' if its kinematic structure takes the form of an open-loop chain. It is said 'parallel' if it is made up of a closed-loop chain (Tsai 1999).

for ultrasound imaging. Additionally, the roll motion is limited to $\pm 60^{\circ}$. Another version of this mechanism, called Pantoscope, can provide infinite roll motion; however, the actuator corresponding to this degree of freedom is floating[3].

The 2-DoF spherical mechanism by Hong (2002) can have both interior and exterior remote center-of-motions (RCM[4]). However, these types of mechanisms are shown to have singular configurations[5] inside their workspace (Ouerfelli and Kumar 1994).

Double pointing wrist by Stanisic and Duta (1990) is a singularity-free device. It uses two pivoted circular sliders located in perpendicular planes. Although, a singularity-free workspace is an asset, the wrist does not have a RCM. Dexterous spherical wrist by Wiitala and Stanisic (2000) describes a device in which all links move on sphere. There is no RCM in the wrist structure.

Carricato and Castelli (2004) introduced a fully decoupled 2-DoF parallel wrist in which each motor is responsible for one orientation of the moving platform about an axis. Kinematic decoupling simplifies design and implementation of control algorithms. Asada and Granito (1985) presented a 3-DoF spherical wrist with no singular configuration in its workspace. Similarly, the 3-DoF Agile eye mechanism by Gosselin and Hamel (1994) is composed of three spherical chains made of revolute joints, but has a rotation center inside the mechanism. Hamlin and Sanderson (1994) used a six-bar pantograph in different configurations to make modular, reconfigurable parallel manipulators with novel spherical joints. However, their mechanism cannot be used for ultrasound imaging.

The concept of remote ultrasound imaging was first appeared in the article by Sublett, Dempsey and Weaver (1995) who presented the design and implementation of a digital image capture and distribution system that supports remote ultrasound examinations. The task was accomplished with cooperation between a radiologist and a technician manipulating an ultrasound probe on the patient at the remote site.

---

[3] If an actuator is not attached to a fixed base, it is called a floating actuator.

[4] Remote center-of-motion (RCM) is a point located outside the mechanism and the end-effector of the mechanism spherically moves about that point.

[5] A manipulator is said to be in a singular configuration when the Jacobian matrix losses its full rank. Singular configurations can be found by setting the determinant of the Jacobian matrix to zero (Tsai, 1999). For robot manipulators, Jacobian matrix is defined as the matrix that transforms the joint rates in actuator space to the velocity state in the end-effector space.

The European project TeleinVivo (Kontaxakis et al. 2000) aimed at developing a transportable telemedicine workstation to be used in isolated areas such as islands, rural areas, and crisis situation areas. The station consists of a portable PC with telecommunication capabilities and a light, portable 3-D ultrasound machine. With a 3-D ultrasound probe a volume of data acquired by the operator close to the patient can be sent to an expert who can examine the data in much the same way that he would examine a patient. Operators still have to perform the examination on the patient but they are guided by the medical expert.

Degoulange et al. (1998) developed an articulated robotic arm based on serial configuration for moving an ultrasound probe on patient's body. Due to its serial configuration, all electric actuators are floating which makes the robot heavier compared with non-floating actuation system.

Salcudean et al. (2000) developed an ultrasound robot in order to reduce the joint fatigue of the ultrasound technicians (Figure 1-4). The authors used a pantograph to generate a conical motion about a fixed point on the patient's body using a serial configuration and floating actuators. The whole manipulator is statically balanced by adding counterbalance weights. Counterbalance weights increase the overall inertia of the system. Furthermore, in providing palpating motion for abdominal ultrasound examination, the whole manipulator must be moved up and down.

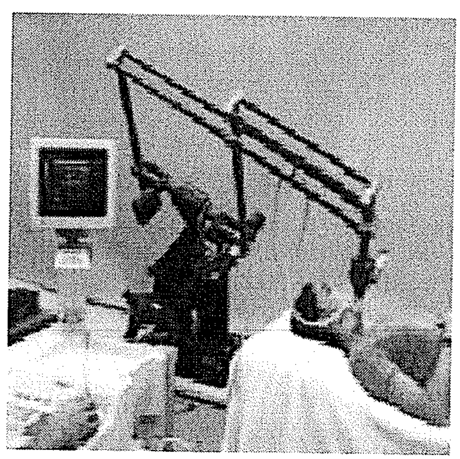

Figure 1-4. Robot-assisted diagnostic ultrasound (Sacudean et al. 2000).

Masuda et al. (2001) designed and constructed a robot for tele-echography that rests on the patient's body during examination (Figure 1-5). There is no reasonable access to the patient in an emergency case. Furthermore, for orienting the probe about a fixed point on the abdomen, all joints must move in a coordinated manner.

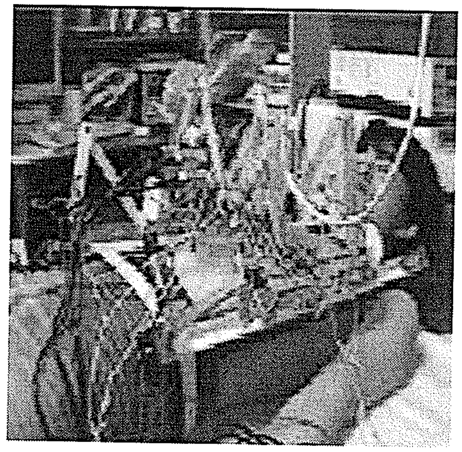

Figure 1-5. Robotic system for tele-echography: robotic mechanism holding an ultrasound probe on patient's body (Masuda et al. 2001).

Koizumi et al. (2008) developed a system for remote ultrasound imaging consisting of circular guides connected in a serial configuration with floating actuators (Figure 1-6). The system has a RCM but appears to be bulky.

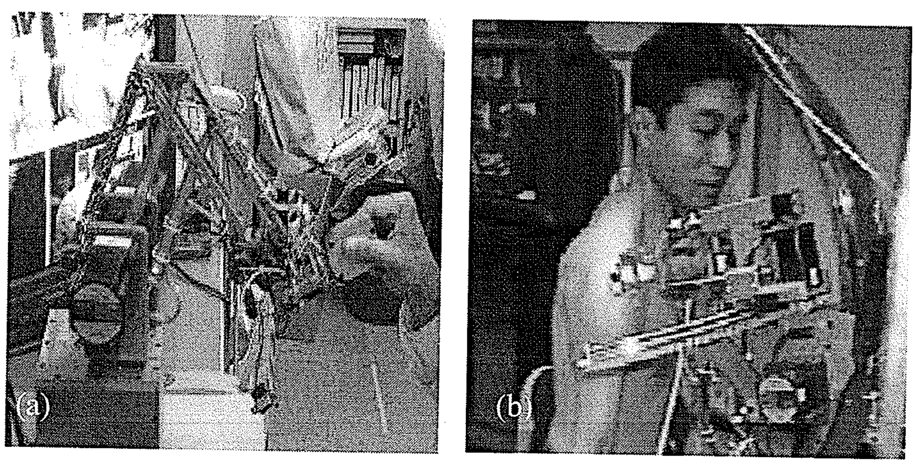

Figure 1-6. Remote ultrasound examination system: (a) physician manipulating stylus of a special-purpose haptic device for remote ultrasound imaging; (b) robotic arm performing ultrasound imaging on a patient (Koizumi et al. 2008).

Vilchis et al. (2003) reported the development of a parallel mechanism for positioning the ultrasound probe, and a wrist based on serial configuration with remote actuations for orienting the probe (Figure 1-7b). The system appears to be bulky and entirely embraces the patient in a way that there is no reasonable access to the patient by attending nurse. There is continuous contact between moving elements of the arm and the patient's body.

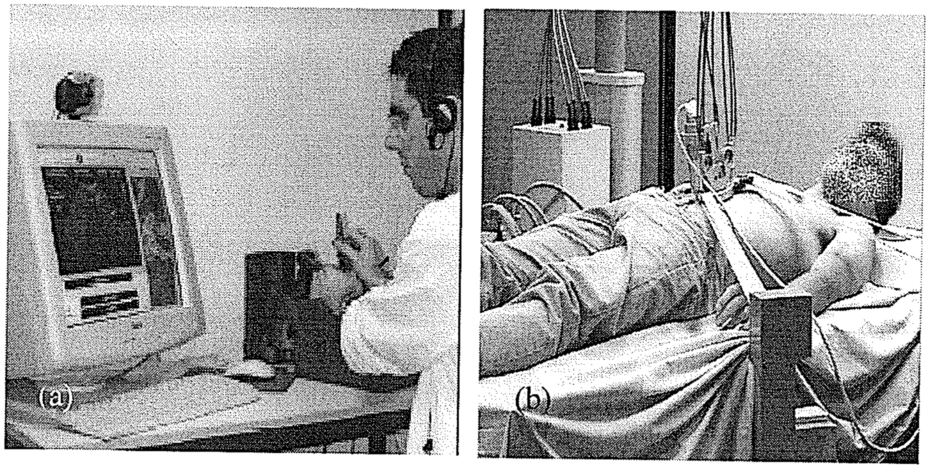

Figure 1-7. Robotic system for tele-echography: (a) physician manipulating stylus of a PHANToM device (SensAble) for remote ultrasound imaging; (b) robotic device performing ultrasound imaging (Vilchis et al. 2003).

Najafi (2004) designed a basic robotic system for remote palpation and ultrasound imaging. The design of a basic robotic wrist and a hand-controller was presented. The prototypes of both devices only had three DoFs with no force feedback capability for the hand-controller. The 3-DoF wrist and Hand-controller were interfaced to a PC. Forward kinematics and Jacobian matrix of the hand-controller were derived based on Danavit-Hartenberg method and did not consider the constraints involved in hand-controller parallel structure.

The European OTELO project described in Delgore et al. (2005) developed a 4-DoF robotic arm (Figure 1-8b). The system is able to orient an ultrasound probe about a fixed point on the patient's body. The actuators in this wrist are floating and coupled. Thus, they must move together in a coordinated manner to create standard ultrasound motions.

The wrist also has a singular configuration at the middle of its workspace, which can deteriorate ultrasound images. The ultrasound wrist developed by Gourdon et al. (1999) uses a differential mechanism with bevel gears and kinematically coupled DoFs. Bevel gears introduce backlash in the wrist power-train which produce non-smooth motions at the end-effector.

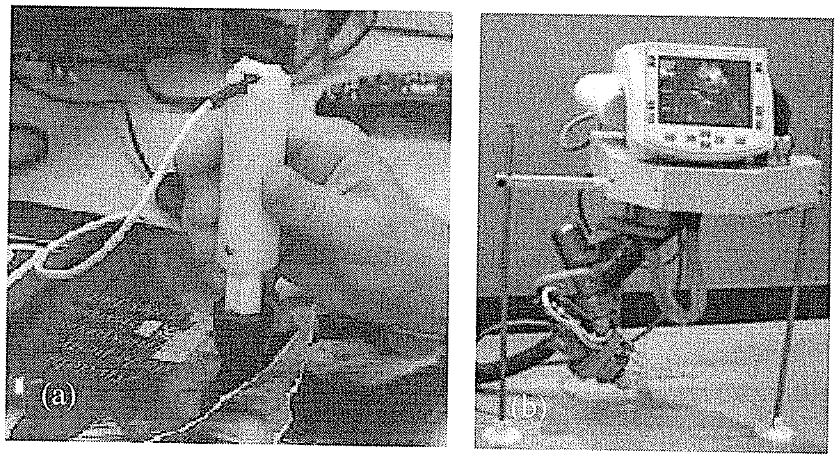

Figure 1-8. Tele-operated mobile ultrasound scanner: (a) physician manipulating a special-purpose controller for remote ultrasound imaging; (b) mobile robotic arm for performing ultrasound imaging (Delgore et al. 2005).

Vilchis et al. (2007) designed and constructed a 4-DoF robotic arm for ultrasound examinations (Figure 1-9). The device uses circular sliders powered by pinion gears in a serial configuration which is similar to the ultrasound robot developed by Koizumi et al. (2008).

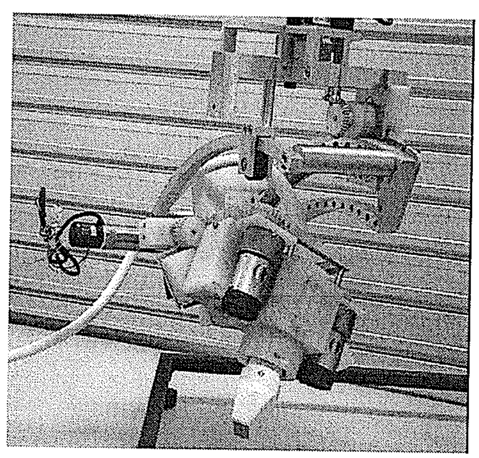

Figure 1-9. Robotic arm for ultrasound examination (Gonzalez et al. 2007).

Bassan et al. (2007) developed a 5-DoF manipulator with remote center-of-motion and cable actuation for 3-D ultrasound guided needle insertion (Figure 1-10). The electric motors are not mounted on a fixed base. This feature increases the inertia of the moving elements.

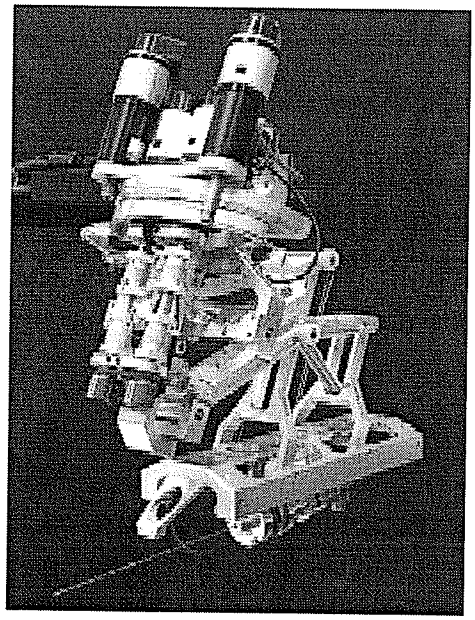

Figure 1-10. Manipulator for 3-D ultrasound guided needle insertion (Bassan et al. 2007).

Surgical instruments also have mechanisms with RCM and thus could potentially be used for ultrasound imaging. The remote center-of-motion robot for surgery by Taylor et al. (1995) has 4 DoFs and all the actuators are mounted on the proximal part of the device. The surgical instrument developed by Madhani et al. (1998) uses a novel cabling system for remote actuation of a miniature surgical wrist. Taylor and Madhani's mechanisms are similar to each other. Using Taylor and Madhani's mechanisms while achieving the compactness required for an ultrasound wrist, leads to closeness of the electrical actuators to the patient's body. Faraz and Payandeh (1998) designed a RCM mechanism for laparoscopic surgery with serial configuration and floating actuators. Similar work has been reported by Cavusoglu et al. (1999) which uses three linear actuators with base-mounted motors for the first three DoFs, and one floating actuator for the fourth DoF. The RCM device for endoscopic surgery by Funda et al. (2001) provides a RCM point using two circular guides. Commercially available precision-circular-guides are normally bulky and heavy.

1.4.2 Haptic Device

There exist many hand-controllers and haptic devices developed for various tasks including medical training and diagnosis. Bauman et al. (1997) designed a haptic device that uses a 4-DoF parallel manipulator with a remote center-of-motion for surgical simulations. The mechanism uses two perpendicular pantographs to provide spherical motion.

PHANToM by SensAble Technologies (Massie and Salisbury 1996) was built based on a four-bar mechanism that produces three or six DoFs with force feedback. For ultrasound examination, the first three motors should be simultaneously torque-servoed to provide force feedback along the desired axis of the stylus as in the case of holding the ultrasound probe. Although, the device has been used for proof-of-concept in ultrasound robotic systems (see Figure 1-7a), the results were not satisfactory due to lack of PHANToM's adaptability with ultrasound applications (Vilchis et al. 2003; Tahmasebi et al. 2008).

The needle-insertion-simulator by Bevrit et al. (2000) has three DoFs and provides a fixed center-of-motion (FCM[6]). The first two DoFs create the orientation of the end-effector. The third DoF provides the linear motion of the end-effector along the radius of the created hemisphere by the first two DoFs. The actuator of the third DoF is floating.

The 3-DoF device by Birglen et al. (2002) uses a spherical parallel mechanism. The mechanism has a FCM, but does not allow a linear motion along the axis passing through the FCM. The 6-DoF haptic device developed by Lee et al. (2001) uses parallel structure and non-floating actuators. In order to move the moving platform about a fixed point, all DoFs should be controlled in a coordinated manner. Furthermore, the mechanism has undesirable singular configurations in its workspace. At singular configurations, haptic devices cannot properly reflect force.

---

[6] FCM is defined, in this thesis, as a point which is inside the mechanism and the end-effector of the mechanism spherically rotates about that point.

Yoon and Ryu (2001) described the design of a 6-DoF haptic device based on parallel mechanisms. The device does not have a FCM and all the power chains are kinematically coupled. The seven-axis haptic device by Hayward (1995) uses a hybrid mechanism consisting of a serial configuration for positioning and a parallel configuration for orientation. The orientation mechanism comprises of two five-bar linkages driven by pulleys.

The haptic pen developed by Stocco et al. (2001) uses two 3-DoF five-bar mechanisms that provide three translations and two rotations of the end-effector. The sixth DoF (roll) is provided by an actuator mounted on the five-bar mechanism. The mechanism has a singular configuration within its workspace which is eliminated by the addition of a redundant actuator.

Vlachos et al. (2003) developed a 5-DoF haptic device which is used as part of a training simulator for urological operations. The mechanism consists of a 2-DoF, five-bar mechanism and a 3-DoF spherical joint. All five actuators are base-mounted and the orientation DoFs are decoupled. For applications such as ultrasound imaging, however, it is highly desirable to have a linear force feedback along the roll axis of the spherical joint. In this device, the desired force feedback along the roll axis demands undesirable simultaneous movements of all DoFs.

Duriez et al. (2001) developed a 3-DoF parallel mechanism creating a spherical surface with a variable radius. It was used to simulate abdominal movements during ultrasound examination. The mechanism does not have a FCM and all DoFs are kinematically coupled. Koizumi et al. (2007) developed a complete tele-echography system including a hand-controller. The hand-controller has 6 DoFs to achieve arbitrary positions and orientations of an ultrasound probe (see Figure 1-6a). A parallel link mechanism was used for positioning. The degrees of freedom in the orientation and positioning mechanisms seem to be coupled and the actuators are floating.

Marchal and Troccaz (2004) reported development of a 1-DoF haptic probe, whose position and orientation is tracked using a magnetic localizer (see Figure 1-8a). The tracker is attached to an element integrating a floating motor and a ball screw for transmitting linear force. The entire device must sit on a surface to establish a FCM.

Remarks

Within the context of ultrasound imaging, the existing robotic arms and haptic devices described above, have one or more of the following undesirable characteristics:

1- lack of suitable DoFs for producing standard clinical motions of ultrasound examinations,

2- absence of RCM in robotic arms and FCM in haptic mechanisms to facilitate 3-D ultrasound examinations,

3- existence of singular configurations in the workspace of robotic wrists and haptic mechanisms,

4- kinematically coupled DoFs in haptic devices and robotic wrists,

5- floating electric motors in the haptic and robotic arms as the main source of excess inertia and difficulties for sterilization of robotic arms,

6- lack of efficient static balancing of the haptic mechanisms,

7- lack of one-to-one control-action correspondence between haptic devices and robotic arms,

8- large size of the robotic arms, and

9- no reasonable access to patients by attending nurse.

1.5 Objectives of this Thesis

In view of the above discussion, it is obvious that one needs to design a new robotic wrist and a corresponding hand-controller which overcome the drawbacks of the available devices prior to this work while keeping the advantages. The usability of the outcome devices should be evaluated by ultrasound experts to facilitate its future clinical trials.

The first objective of this thesis is to develop a robotic wrist having the following specifications:

1- The wrist mechanism should be able to move the ultrasound probe about a RCM point that is located outside the mechanism. During 3-D ultrasound examination, this point is placed on the patient's body.

2- The wrist should provide a singularity-free workspace. Singularities can deteriorate ultrasound images taken by wrist during ultrasound imaging (Delgore et al. 2005). At singular configurations, actuator saturation, breakdown and undesirable motion happen.

3- The wrist should have structural rigidity. Parallel manipulators provide higher structural rigidity than serial ones.

4- The wrist should have decoupled DoFs. Kinematic decoupling allows one motion of the ultrasound probe by only actuating one kinematic chain. This will significantly simplify design and implementation of control algorithms. Most parallel manipulators have coupled DoFs (Carricato and Castelli 2004). Achieving kinematically decoupled DoFs in parallel mechanisms is challenging.

5- It is desirable to have a compact and light wrist. This will increase the portability of the device which is important in mobile tele-ultrasound systems (Delgore et al. 2005).

6- To maintain the contact between ultrasound probe and the patient's body and to capture continuous ultrasound images, the wrist should be able to apply palpation forces up to 20 N (Guerin et al. 2003).

7- Ultrasound probe velocities vary during free-hand ultrasound examinations. The robotic wrist should be able to move the probe with the average velocity of 3°/s (Salcudean et al. 2000).

8- The ultrasound probe should move in a conical workspace with a vertex angle up to 60°. The palpating motion should be about 30 mm (Guerin et al. 2003).

9- The wrist should operate in a safe manner. Ikta and Nokata (1999), Morita and Sugano (1995) and Khodabandehloo et al. (2003) have developed and quantified safety aspects of the medical robots. Safety goals which are to be considered in the design of the proposed wrist are:

a- There should be reasonable access to the patient by the attending nurse.

b- The electrical actuators should be as far as possible from the patient. They must be isolated to prevent electrical shocks and facilitate cleaning.

c- In case of power failure, the manipulator should fail in a safe and predictable manner.

d- The inertia of the moving elements should be kept low. This will reduce the impact force between the patient and the manipulator (Ikta and Nokata 1999). Parallel manipulators give the ability to place all actuators on the ground and consequently reduce the inertia of the wrist and the size of the actuators.

The second objective of this research is to develop a force reflecting hand-controller which is suitable for remote ultrasound examination. The following factors should be considered in the design of the device:

1- The device should be able to generate standard ultrasound movements about a fixed center-of-motion (FCM), resembling the pivot point of the ultrasound probe on the patient's body. At the same time, the hand-grip must also slide as much as 30 mm along the axis of the probe passing through the pivot point for maintaining continuous pressure between the remote probe and the patient's body (Guerin et al. 2003). Further, the output force of the device applied to user's hand should be uniform over the entire workspace.

2- The device should be statically balanced. Static balancing implies that no operating effort for the actuators or the operators, apart from acceleration and deceleration, is needed to move the device from one configuration to another. Static balancing reduces operator fatigue and actuator's inertia size. It also improves inherent safety in case the operator lets go of the hand-controller.

3- The operator's hand gestures when she/he holds the hand-grip should resemble holding an ultrasound probe. This will increase the quality of force feedback because different joints and muscles have different input force bandwidth (Brooks 1990). It also makes the use of the hand-controller more intuitive since the operator can move her/his hand and consequently the slave wrist in its most natural way (Kulishov and Lakota 1988).

4- The workspace created by hand-controller should be singularity-free. Hand-controllers cannot simply avoid singular points, because they are operated by user's random commands. At singular points, mechanisms lose or gain degrees of freedom; thus, force cannot be reflected properly.

5- Structural rigidity is an important factor which enables the hand-controller to tolerate higher forces (Orlov 1979). Parallel mechanisms provide higher structural rigidity than serial ones.

6- The DoFs should be kinematically decoupled to provide force feedback to the operator's hand along each ultrasound motion direction with only one actuator. Decoupled kinematic also reduces the amount of power train inertia.

7- Inertia of the moving elements should be kept low to reduce fatigue, which in turn affects the quality of tele-operation. Since actuators are the main sources of inertia in haptic mechanisms, they should be placed on the base.

8- The power train should be backdriveable[7], especially when the position error loop is used for force control (Daniel and Siva 1990). Although considered in this thesis, backdriveability is not always an asset especially when the operator lets go of the haptic (Kulishov and Lakota 1988; Madhani 1998).

9- The DoFs in haptic and wrist should have one-to-one position correspondence (control-action correspondence), i.e. any control action by the physician and its resulting-change in the remote robotic wrist moves equally and in the same direction (Sheridan, 1992). It has been argued that, it is very easy for the operator to lose track of relative position and orientation between remote arm and operator's hand. This is particularly aggravated by one's having to observe the results of remote manipulation through video or other displays such as ultrasound, or by not having one-to-one position correspondence (Sheridan, 1992). Therefore, the probe orientation in the wrist mechanism should always be aligned with the orientation of the operator's hand. This simplifies control algorithms and removes operator's mental load from thinking of the relative position between her/his hand and the probe.

[7] According to Ishida and Takanishi (2006), qualitative definition of backdriveability is that when the output axis of a mechanism is moved by a force, this motion is conveyed through the power transmission to the input axis. The level of easiness of force and motion transmission from output axis to input axis is defined as backdriveability.

1.6 Scope of this Thesis

This thesis focuses on the mechanical design, kinematics analysis, prototyping and performance evaluation of a novel 4-DoF robotic wrist and haptic device suitable for remote ultrasound examination of patients (see Figure 1-11). In particular, this thesis elaborates on features that have not been previously explored, all together, for ultrasound application. This thesis also presents the complete mechanical design of both systems which fulfill the objectives outlined earlier. Control and communication systems are implemented not as the focus of this work but to make the entire robotic system work.

Specifically in this thesis, the detailed and embodiment design of the 4-DoF robotic wrist is described. The modifications to the previous wrist by Najafi (2004) include: changing the design of the universal telescoping joints from single-stage to double stage to reduce the height of the wrist, changing the detail design of all joints, cable routings, and combinatory module to make them practical in terms of increasing rigidity and decreasing friction and inertia of the new device. The complete prototype of the 4-DoF ultrasound wrist is constructed. The prototype enables physician to remotely maintain the contact between ultrasound probe and patient's body which is vital for proper ultrasound imaging. The 4-DoF haptic device in this thesis is statically balanced using only a tension spring which required a new design for mechanism's linkages and their arrangements. The inertia of the device is significantly reduced by changing the arrangement and miniaturization of the elements of the third DoF which provides force reflection to the operator hand. Complete prototype of the device is made and its technical characteristics such as static balancing performance, static-friction break away force, and maximum achievable impedances are evaluated. The effect of fixed center-of-motion created by hardware is investigated and its results are compared with the ones of an OMNI PHANToM device in which the FCM was created by virtual fixtures. Analytical static output force and output force error analysis have been presented for the haptic device. Complete forward kinematic analysis is presented for both wrist and haptic devices based on successive rotations. The relationship between the actuators and the ultrasound probe rotations are determined for both devices. The Jacobian matrix of both devices are derived based on loop-closure equations which considers all the constraints involved in the parallel structure of both devices. New computer interfacing hardware is developed for both haptic and wrist in which the devices are connected together through Internet using campus network. Bilateral control is implemented to enable physicians to remotely control the motion of the wrist device while feeling the contact force between remote probe and patient. Ultrasound imaging tests of kidney, spleen, livers, and heart of a few volunteers are done during the development of the new wrist and haptic devices.

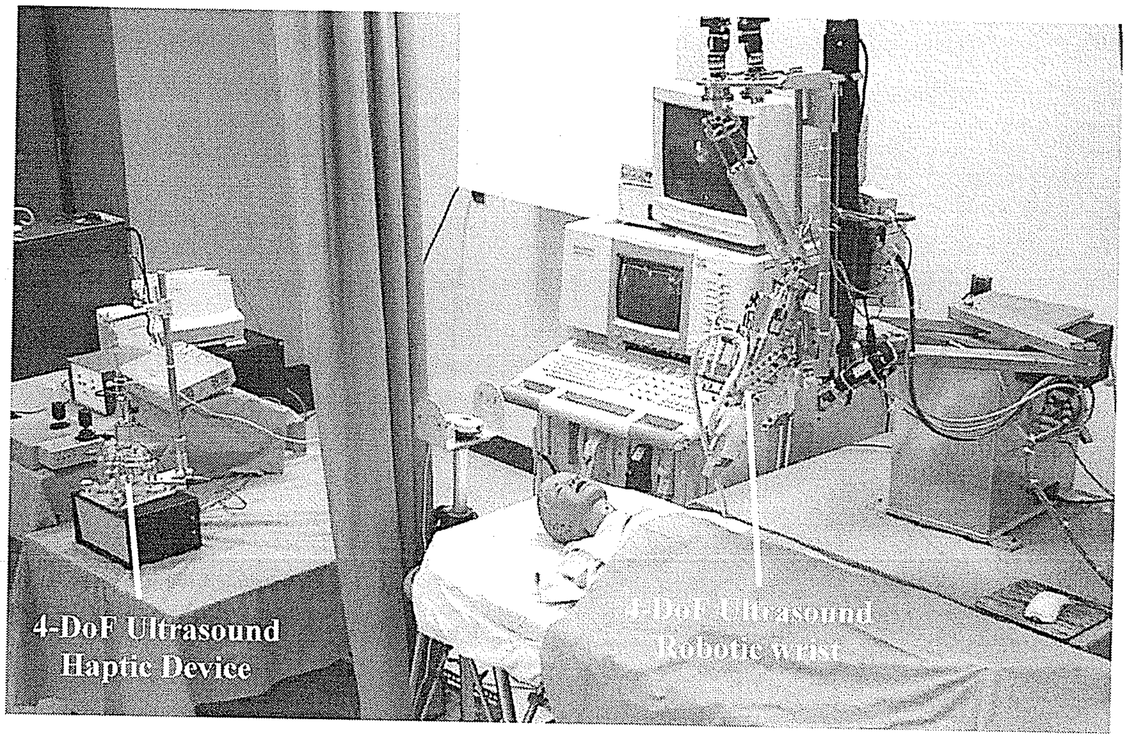

Figure 1-11. General view of robotic system for remote ultrasound imaging.

The outline of this thesis is as follows: Chapter 2 describes the conceptual and embodiment design, kinematics analysis, and prototyping of the 4-DoF robotic wrist suitable for remote ultrasound imaging. Technical specifications of the robotic wrist including workspace, overall dimensions, and inertial properties are determined and presented in this Chapter.

Chapter 3 addresses the conceptual and embodiment design, kinematics and output force analysis, and performance evaluation of the 4-DoF force reflecting hand-controller for remote ultrasound examination. Performance evaluation aims to examine the technical characteristics of the device including inertial properties, static balancing, static-friction break-away force, maximum and uniformity of the output force, and maximum/minimum achievable impedances. Additionally, the performance evaluation identifies the effect of fixed center-of-motion on remote ultrasound examination task.

Chapter 4 describes computer interfacing and performance evaluation of the entire experimental setup. Force and position tracking responses between the haptic device and robotic wrist are described. Ultrasound imaging tests of the kidney, spleen, liver and heart of the volunteers is presented in this Chapter.

Chapter 5 summarizes the contributions of the thesis and presents ideas for future work.

Chapter 2

Design of Ultrasound Robotic Wrist[1]

This Chapter describes the development of a 4-DoF robotic wrist to enable physicians to perform ultrasound diagnosis on patients located in remote areas. This Chapter also describes how the basis structure of the wrist is conceptualized to satisfy the objectives outlined in Section 1.5. Detailed design, kinematics analysis, and preliminary evaluation of the prototype wrist are presented.

2.1 Basic Structure

There are various planar or spatial mechanisms in the literature which provides circular or spherical motion of the end-point (Artobolevsky 1979). Spherical five-bar linkage mechanisms can provide pitch and yaw motions of the ultrasound probe. They can be designed very light. However, singular configurations may happen in the middle of the workspace (Ouerfelli and Kumar 1994). Circular-slider mechanisms are planar and provide the circular motion of the end-point. Two circular sliders can be derived by crank mechanisms or pinion gears (Artobolevsky 1979; Sclater and Chironios 2001). They can also be combined together in serial and parallel configurations to provide pitch and yaw motions. Circular sliders, however, are heavy and need precision machining. Another idea is to combine two spherical linkages in serial to provide a 2-DoF spherical mechanism. However, actuators will be floating in this mechanism.

The basic structure of the proposed wrist was inspired by the mechanism introduced by Stanisic and Duta (1990). They presented a symmetrically actuated double pointing system, which was a basis for a singularity-free workspace. It consists of two circular links carrying circular sliders. Circular sliders are pined together to generate a 2-DoF

[1] Some material of this Chapter has been published in:
Najafi, F. and Sepehri N. (2007). Hand controller and wrist device. US patent No. 7,204,168.

mechanism. Circular slides are heavy and costly and need precise machining. Additionally, the center of rotation is located on the plane in which the actuators are located. A simple mechanism that achieves the same motions consists of two six-bar pantographs shown in Figure 2-1a. Each link in this mechanism is easy to manufacture and can be built light. The end-links of the pantographs (E_1F_1 and E_2F_2) are connected together by a revolute joint. By rotating the links A_1B_1 and A_2B_2 via two actuators, point R of the revolute joint moves on the hemispherical workspace. This mechanism has two decoupled DoFs in which the singular configurations are located on the great circle of the hemisphere. By holding the links E_1F_1 and E_2F_2 in vertical position, and rotating links A_1B_1 and A_2B_2 about O as much as α with respect to the horizontal plane will move the remote center-of-motion (RCM), O, outside the wrist mechanism (see Figure 2-1b). Although, this slightly reduces the workspace of the pantograph, the actuators and moving links A_1B_1 and A_2B_2 are moved away from the RCM. The mechanism shown in Figure 2-1b is a parallel mechanism to provide the pitch and yaw scanning motions of the ultrasound probe.

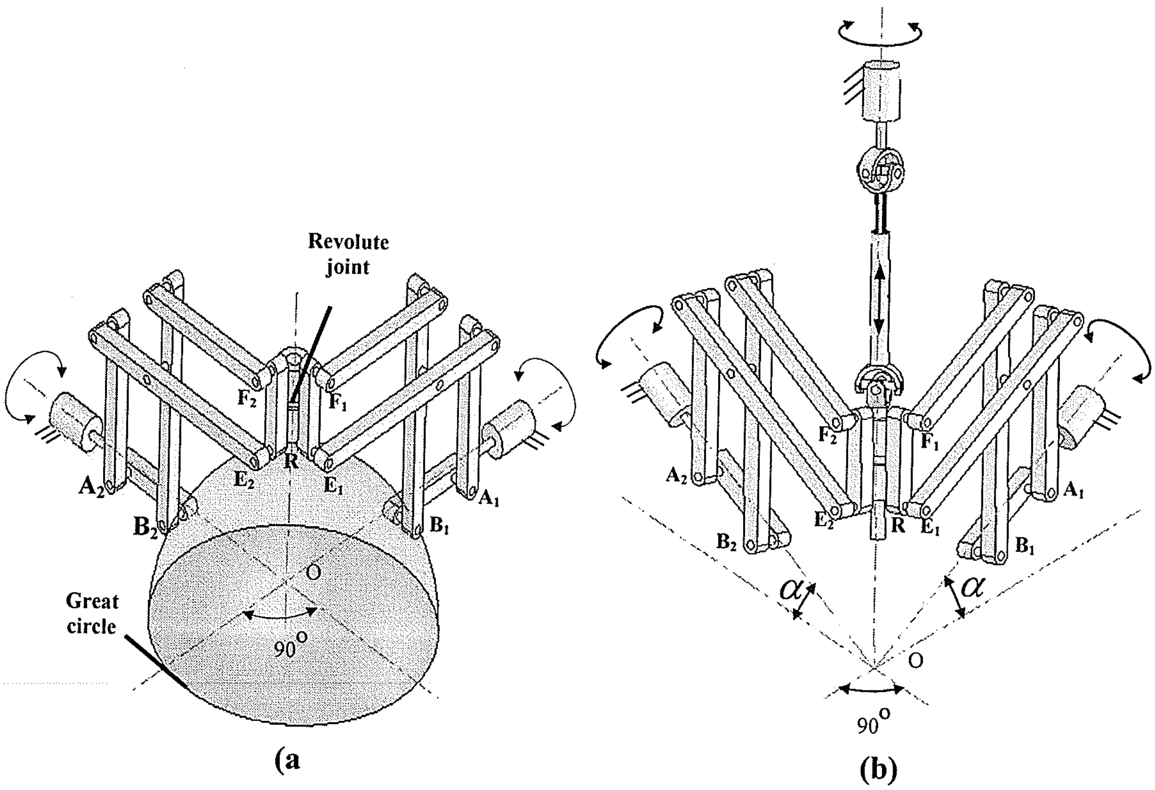

Figure. 2-1. Wrist mechanism: (a) 2-DoF parallel wrist with a singularity-free workspace in which DoFs are decoupled; (b) 3-DoF parallel wrist with a singularity-free workspace and decoupled DoFs with RCM, O.

The rotational motion of the ultrasound probe along its axis is achieved by combining two universal joints connected by a shaft and actuated by an electric motor (see Figure 2-1b). Since point R moves on a sphere, the distance between the centers of the universal joints changes. Therefore an axial sliding motion is required for the shaft connecting the two universal joints. The redundancies of the axial slider and universal joints allow the universal telescoping joint to idly follow the motion of the two pantographs while independently transmitting the actuator's torque to the revolute joint of the pantographs. This produces a decoupled rotational motion about the radius OR of the created hemisphere (Figure 2-1b). The rotational motion serves two purposes: (1) it can be used for rotational motion of the ultrasound probe; (2) it can also be converted to a sliding motion along the axis of the probe for palpating purposes, which will be discussed in detail in Section 2.2.4.

2.2 Embodiment Design

This section presents the detailed descriptions and assemblies of the wrist. Figure 2-2 shows the front and back view of the wrist. This design uses the basic kinematics architecture discussed in the previous Section. A pair of six-bar pantographs is mounted on the circular frame to define the first two DoFs of the ultrasound probe. The circular frame is connected to the columns and the upper housing which accommodates electric actuators.

2.2.1 Design of First and Second DoFs

The end-links of the pantographs are connected together with ball bearings. Both end-links are hollow to provide enough space to accommodate the combinatory module for the third and fourth DoFs which will be discussed in Section 2.2.4. Since the interferences between linkages and the connecting shafts make the workspace small, special crank-shafts have been designed to allow the linkages to move freely without interference with other connecting shafts (see Figure 2-3). Care has been taken to ensure rigidity both in the plane of the pantographs and in their normal planes. The electric actuators can be connected to the input shafts for applications where the closeness of the actuators to the RCM is not of concern. However, regarding the ultrasound application, it is preferred to connect each actuator to its pantograph via cable drives. An open-loop cable drive system has been designed to prevent slippage of the cable (see Figure 2-3). The driver and driven pulleys are fixed to the actuator and input shafts respectively. Cables pass through guiding pulleys. A cable tensioner designed to adjust the cable tension. A second encoder can be added on the input shaft to check the breakage of the cable for safety issues.

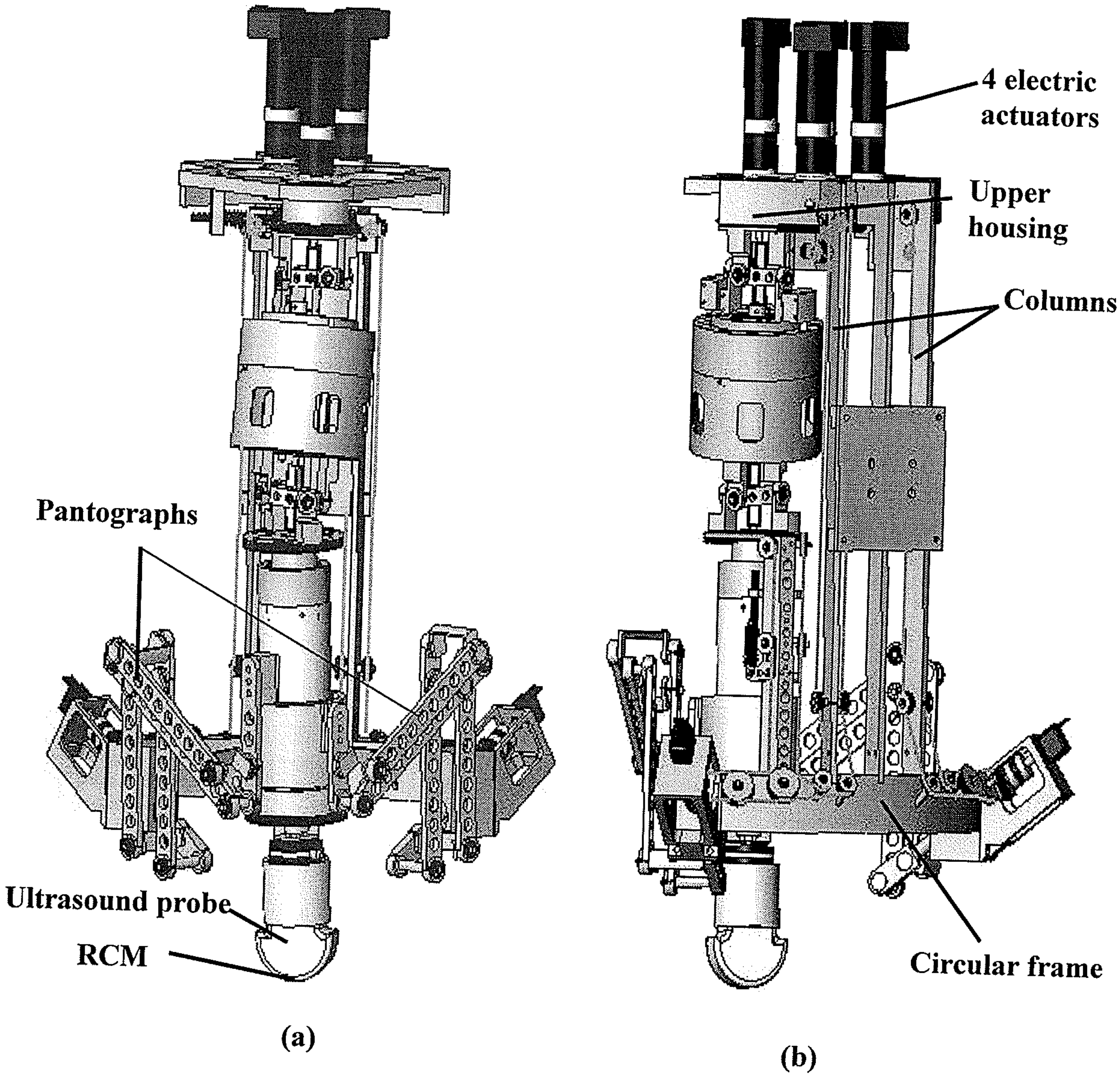

Figure 2-2. General view of 4-DoF robotic wrist: (a) front view of the wrist; (b) back view of the wrist.

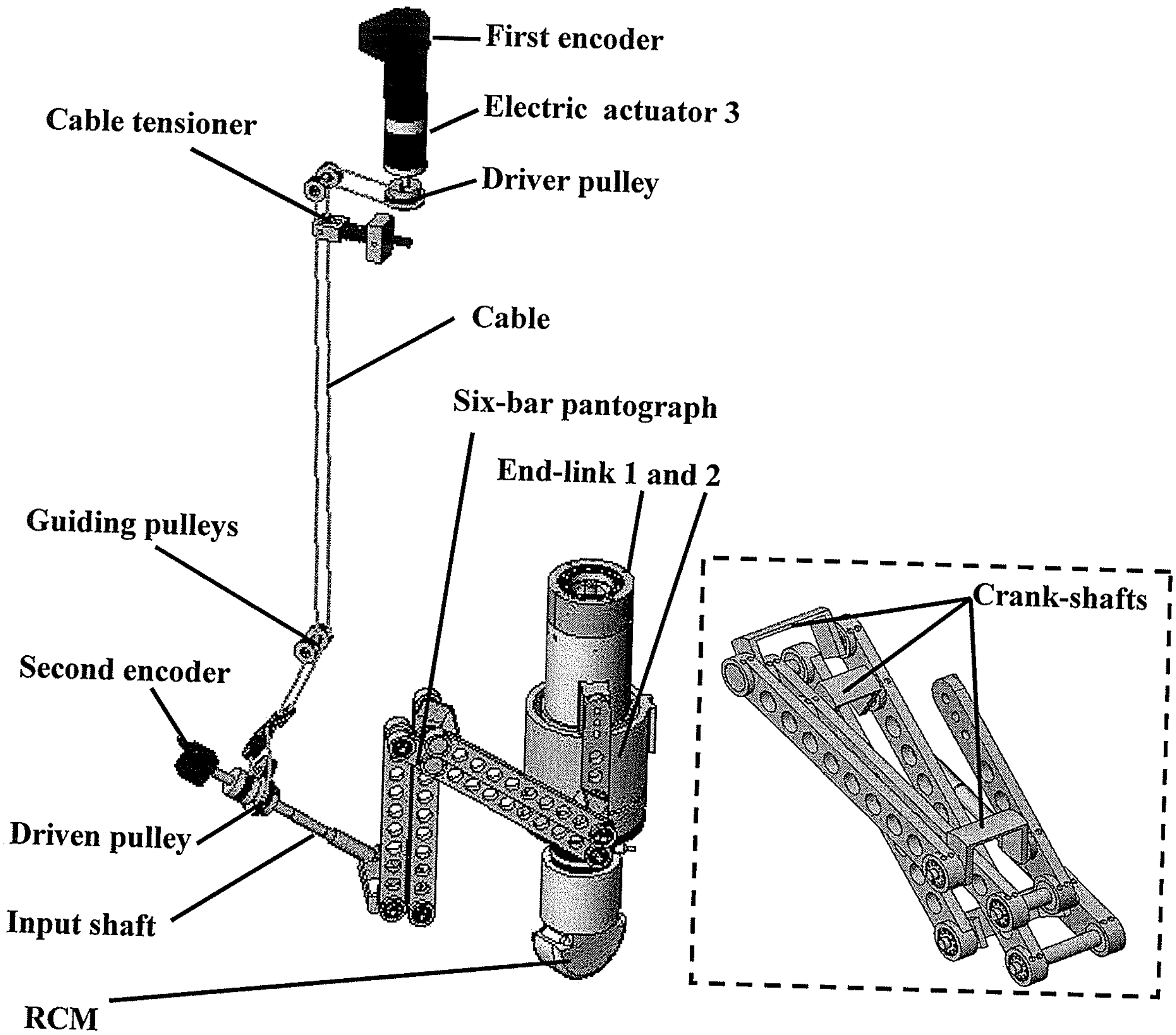

Figure 2-3. Power train of each of the first two DoFs of the wrist.

2.2.2 Design of Third DoF

The third DoF has been designed to produce a sliding motion of the ultrasound probe along the axis of the probe which is herewith called palpating motion (see Figure 2-4). The third DoF maintains the contact between probe and patient. Its power train consists of an electric actuator, an upper universal joint, inner telescoping joint, lower universal joint and finally the combinatory module. Upper universal joint is connected to the electric actuator. The lower universal joint is connected to the pantograph's end-link by decoupling ball bearings (not shown). The inner telescoping joint permits torque transmission from upper to lower universal joint, while its length between the two universal joints increases when it idly follows the motion of the pantograph's end-link. In order to shorten the overall height of the wrist, inner telescoping joint has two stages. The first and second stages use a combination of ball spline and linear shafts, respectively. The rotary motion is delivered to the combinatory module to generate the palpating motion of the ultrasound probe. The combinatory module is inside the pantograph's end-link and will be described in Section 2.2.4. The close-up view of Figure 2-4 shows the power train of the third DoF where it follows the movement of the first two DoFs created by six-bar pantographs.

2.2.3 Design of Fourth DoF

The fourth DoF creates rotational motion of the ultrasound probe about its axis. Its power train consists of an electric actuator, first cable drive, an outer telescoping joint, second cable drive and combinatory module (Figure 2-5). The combinatory module is placed inside the pantograph's end-link. The upper universal joint is actuated by the first cable drive. The lower universal joint is connected to the pantograph's end-link by decoupling ball bearings (not shown). Outer telescoping joint has two stages accomplished using linear shafts. The outside diameter of the lower universal joint is the driver pulley for the second cable drive in which a cable passes through guiding and driven pulleys. The driven pulley is connected to the end-link of the pantographs through a decoupling ball bearing. Therefore, the rotary motion of the fourth electric actuator is transmitted to the driven pulley of the second cable drive. This rotary motion is delivered to the combinatory module to generate the rotational motion of the ultrasound probe.

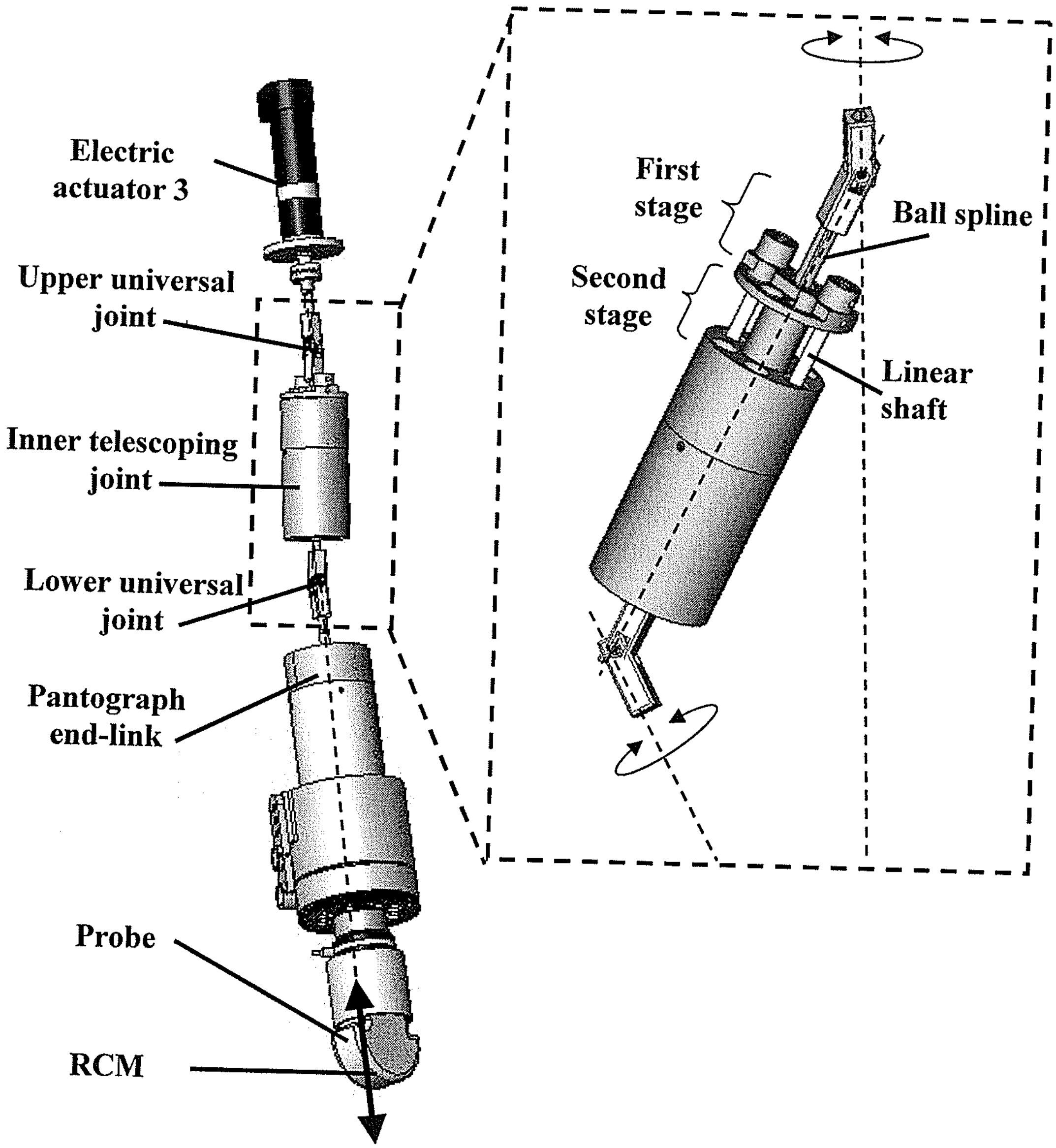

Figure 2-4. Power train of third DoF and close-up view in a tilted position.

2.2.4 Design of Combinatory Module for Third and Fourth DoFs

This module has two inputs and two outputs (Figure 2-6). The module converts rotary motion of the third DoF (first input) into the palpating motion of the ultrasound probe to maintain the contact between ultrasound probe and patient's skin. It also transmits the rotary motion of the fourth DoF (second input) to the rotational motion of the ultrasound probe. Since these two DoFs are kinematically decoupled, the module can produce independent palpating or rotational motions of the probe by each of the two actuators. Spiral motion can also be achieved if both actuators work simultaneously.

The lower universal joint from the third DoF is connected to the ball screw via a multi-jaw coupling which allows easy insertion of the module inside the wrist. Upon driving the ball screw, the slider slides on the linear shafts with respect to the base-plate. The slider is connected to the spline shaft by a decoupling ball bearing to decouple the rotary motion imparted by driven pulley from the sliding motion of the slider. The outer housing is fixed to the driven pulley which receives its rotary motion from the power train of the fourth DoF (see Figure 2-6). The ball spline nut allows free relative axial motion of the probe while transmitting the rotary motion. The ball spline shaft is connected to a force sensor and connector. The pantographs orient the module about the RCM, and the module provides palpating and rotational motions of the ultrasound probe.

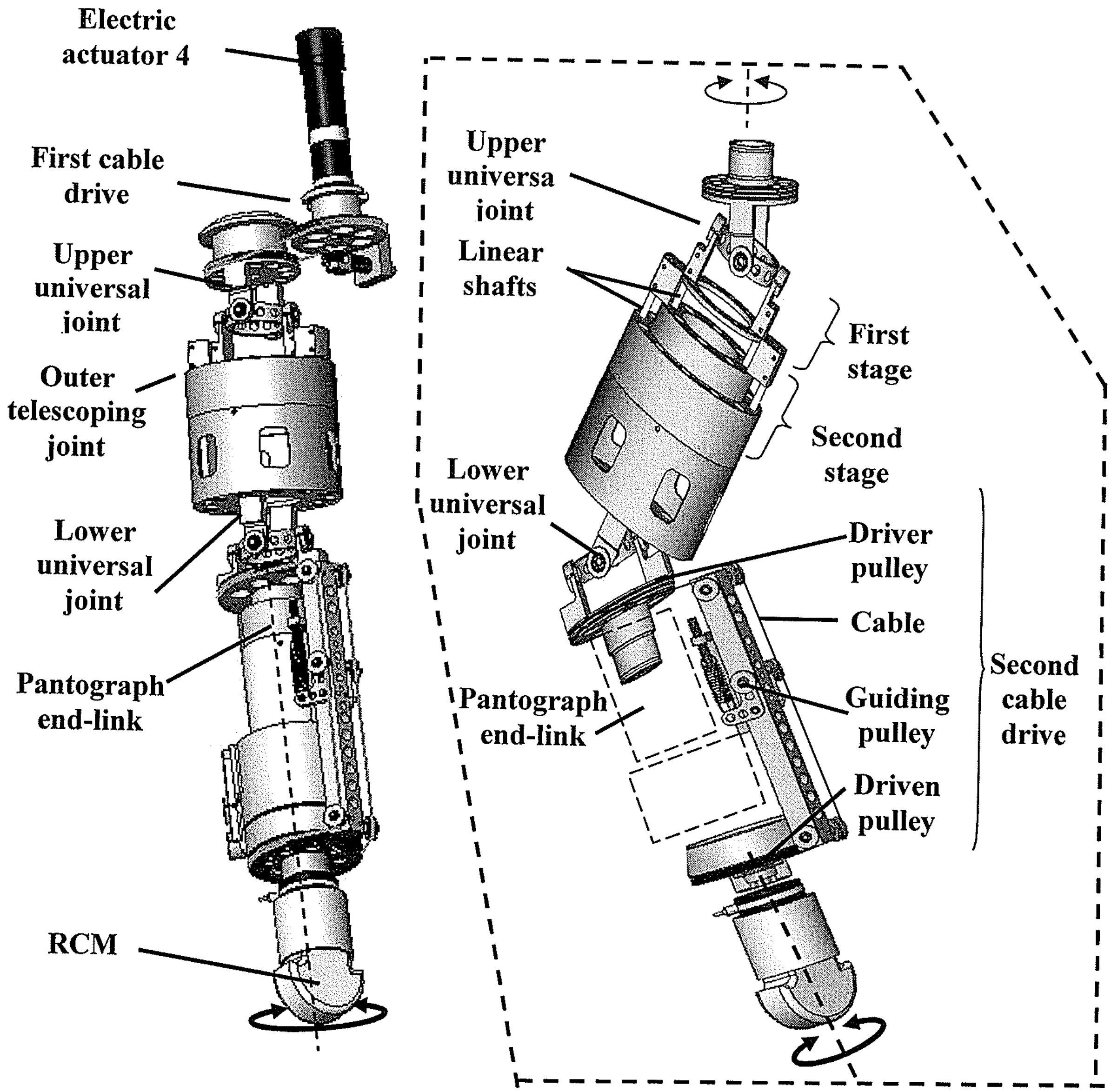

Figure 2-5. Power train of fourth DoF and close-up view in a tilted position.

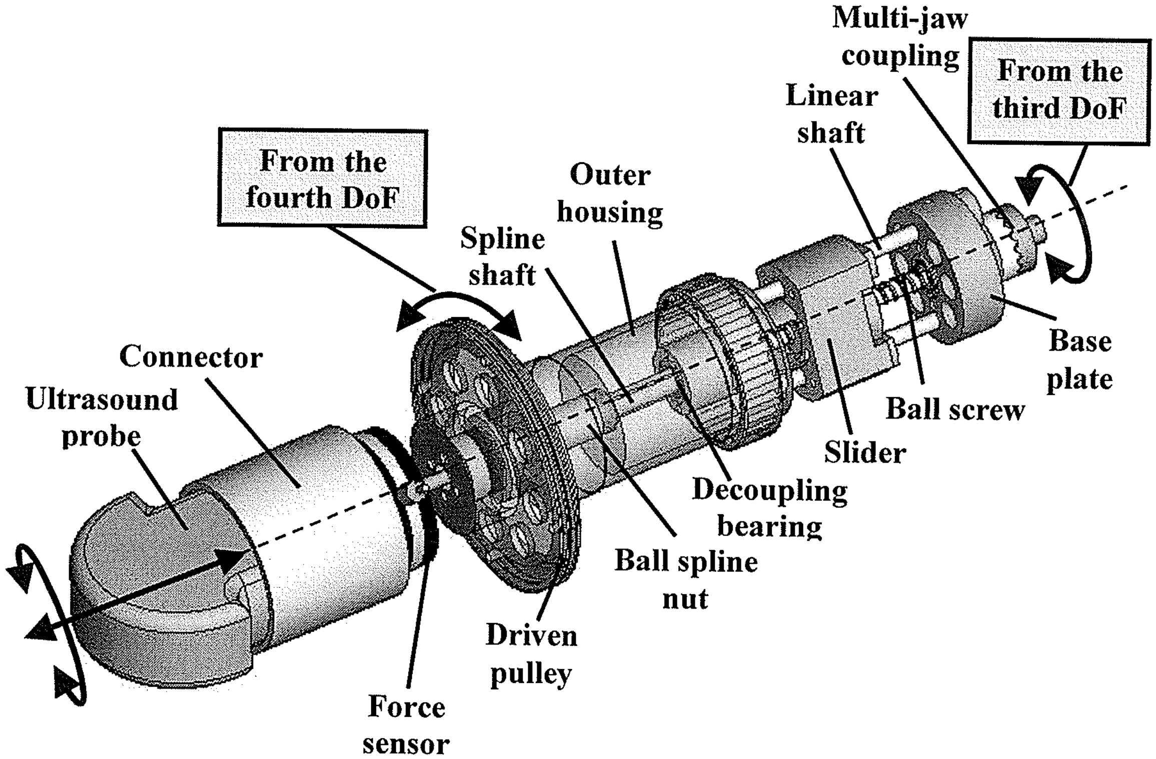

Figure 2-6. Power train of combinatory module.

2.2.5 Discussion

All DoFs in the present wrist are kinematically decoupled, i.e., each required motion of the ultrasound probe is accomplished by only one kinematic chain activated by an electric actuator. The ultrasound robot by Poignet at al. (2003) is a serial manipulator and uses coordinated joint control to move the ultrasound probe. Robots with coordinated joint control have pivot flexibility and increased maneuverability. However, according to Taylor and Stoinovici (2003), for medical applications, RCM mechanisms with decoupled motions, as in the proposed wrist, are safer due to their decoupled motions and simplicity in control implementation.

All RCM mechanisms introduced in the literature, prior to this work, use either serial or hybrid configurations to achieve decoupled DoFs and a singularity-free workspace (Taylor et al. 1995; Faraz and Payandeh 1998; Salcudean et al. 2000; Vischer and Clavel 2000). The present design introduces, for the first time, a parallel version of a RCM mechanism with decoupled DoFs and, as will be shown later, with singularity-free workspace.

Compact wrists allow portability towards mobile tele-echography applications (Delgorge, et al. 2005). Using two six-bar mechanisms in parallel brings the footprint of the new wrist to the order of 192 × 192 mm. Additionally, the weight of the moving elements in the prototype wrist is 2.5 kg. According to Ikta and Nokata (1999), reducing the weight of the moving elements decreases the potential of high impact between robotic arm and patient.

Ultrasound transducers, connectors and cables must be frequently sterilized (Muradali et al. 1995). Using parallel mechanisms with remote cable actuation in the present wrist separate electrical actuators from the linkages and moving components near the probe and thus simplify disinfection procedure. This characteristic has not been observed in other devices including those reported by Mitsuishi et al. (2001), Masuda et al. (2001), Gonzales et al. (2001), and Vilchis et al. (2007). The current practice is to either use presterilized bags around most of the robot and sterilize only the tool holder (Taylor and Stoinovici 2003) or, seal all floating actuators to allow cleaning.

Ultrasound robots designed by Masuda et al. (2001) and Gonzales et al. (2001) both embrace the patient's body and there is no reasonable access to the patient. Proper arrangement of power trains in the present design moved all the wrist elements above the ultrasound probe. Therefore, there is enough access to the patient by the attending nurse. The ultrasound robots developed by Salcudean et al. (2000) and Delgorge et al. (2005) also allow reasonable access to the patient.

2.3 Kinematics Analysis

Forward kinematics consists of finding the position and orientation of the implement (ultrasound probe) given motor joint variables. With reference to Figure 2-7, the fixed frame $\{X_0Y_0Z_0\}$ is attached to point O as the RCM of the wrist. The moving frame $\{X_mY_mZ_m\}$ is attached to the tip of the ultrasound probe. Initially, the moving frame coincides with the fixed frame. The first two rotations θ_1 and θ_2 occur about the axes X_t and Y_t. Axes X_t and Y_t are located in the planes X_0Z_0 and Y_0Z_0, respectively. The third rotation θ_3 occurs about the axis Z_2 of frame $\{X_2Y_2Z_2\}$, the frame resulting from the first two rotations β_1 and β_2. The 4th motion is the radial displacement r of the tip of ultrasound probe along the axis Z_2.

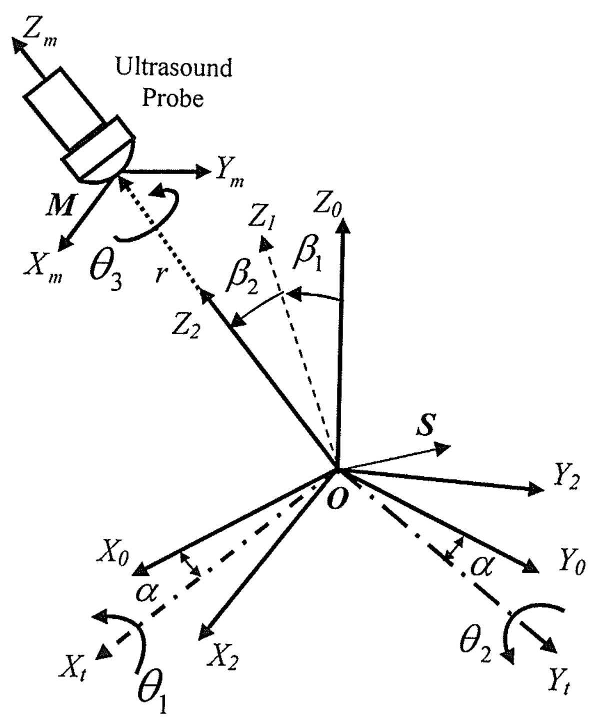

Figure 2-7. Coordinate transformation between the fixed frame $\{X_0Y_0Z_0\}$ and moving frame $\{X_mY_mZ_m\}$ frames.

The axis X_t is rotated as much as α with respect to axis X_0. Moreover, due to geometrical constraints between two pantographs, the rotation θ_1 about axis X_t causes the axis Z_0 to rotate as much as β_1 about axis X_0. Its rotation matrix can be written as (Tsai 1999):

$$Rot(X_0, \beta_1) = \begin{pmatrix} 1 & 0 & 0 \\ 0 & c\beta_1 & -s\beta_1 \\ 0 & s\beta_1 & c\beta_1 \end{pmatrix} \tag{2.1}$$

where

$$\tan\theta_1 = \frac{\tan\beta_1}{\cos\alpha} \tag{2.2}$$

and c and s denote "cosine" and "sine" functions, respectively. Detailed derivation of Eq. (2.2) is presented in Appendix A. The second rotation θ_2 occurs about axis Y_t. Due to geometrical constraints between the two pantographs, the rotation θ_2 causes the axis Z_1 to rotate as much as β_2 about the unit vector S in a plane which contains Z_1 and X_t. Therefore, the unit vector $S(s_x, s_y, s_z)$ is normal to unit vectors $X_t(c\alpha, 0, -s\alpha)$ and $Z_1(0, -s\beta_1, c\beta_1)$ described in the fixed frame $\{X_0 Y_0 Z_0\}$. The orthogonality condition leads to the following Equations:

$$S.X_t = 0 \tag{2.3a}$$

$$S.Z_1 = 0 \tag{2.3b}$$

Solving Eqs. (2.3) simultaneously, we have:

$$s_x = \frac{s\alpha\, s\beta_1}{\sqrt{1 - s^2\alpha\, c^2\beta_1}}; \quad s_y = \frac{c\alpha\, c\beta_1}{\sqrt{1 - s^2\alpha\, c^2\beta_1}}; \quad s_z = \frac{c\alpha\, s\beta_1}{\sqrt{1 - s^2\alpha\, c^2\beta_1}} \tag{2.4}$$

The rotation matrix about axis $S(s_x, s_y, s_z)$ can then be written as (Tsai 1999):

$$Rot(S, \beta_2) = \begin{pmatrix} a_{11} & a_{12} & a_{13} \\ a_{21} & a_{22} & a_{23} \\ a_{31} & a_{32} & a_{33} \end{pmatrix} \tag{2.5}$$

where

$$a_{11} = (s_x^{\,2} - 1)(1 - c\beta_2) + 1; \; a_{12} = s_x s_y (1 - c\beta_2) - s_z s\beta_2; \; a_{13} = s_x s_z (1 - c\beta_2) + s_y s\beta_2$$

$a_{21} = s_x s_y(1-c\beta_2) + s_z s\beta_2$; $a_{22} = (s_y^{\ 2} - 1)(1-c\beta_2) + 1$; $a_{23} = s_y s_z(1-c\beta_2) - s_x s\beta_2$

$a_{31} = s_x s_z(1-c\beta_2) - s_y s\beta_2$; $a_{32} = s_y s_z(1-c\beta_2) + s_x s\beta_2$; $a_{33} = (s_z^{\ 2} - 1)(1-c\beta_2) + 1$

The relationship between angles β_2 and θ_2 is given below:

$$\tan(\beta_2 - \eta) = \frac{c\alpha\, s\theta_2 - s\alpha\, c\alpha\, c\theta_2}{s_y s\alpha\, s\theta_2 - s\alpha\, c\theta_2(s_z c\alpha + s_x s\alpha) + s_y c\theta_2\, c^2\alpha} \tag{2.6a}$$

$$c\eta = s\beta_1\,(s_x s\alpha + s_z c\alpha) + s_y c\beta_1\, c\alpha \tag{2.6b}$$

Detailed derivation of Eq. (2.6) is given in Appendix B. The first two rotations β_1 and β_2 occur about axes X_0 and S described in the fixed frame $\{X_0Y_0Z_0\}$, respectively. Therefore, the resulting rotation matrix is obtained by pre-multiplying the two rotation matrixes described in Eqs. (2.1) and (2.5). The third rotation θ_3 occurs about the axis Z_2 of the frame $\{X_2Y_2Z_2\}$, therefore the third rotation matrix should be post-multiplied.

$$Rot(\beta_1, \beta_2, \theta_3) = Rot(\beta_2, S)Rot(\beta_1, X_0)Rot(\theta_3, Z_2) \tag{2.7}$$

The elements of the homogenous transformation matrix that describes transformation from frame $\{X_0Y_0Z_0\}$ to $\{X_mY_mZ_m\}$ is now obtained as:

$$T = \begin{pmatrix} Rot(\beta_1, \beta_2, \theta_3)_{(3\times3)} & Rot(\beta_1, \beta_2, \theta_3)_{(3\times3)}\begin{pmatrix}0 & 0 & r\end{pmatrix}^T{}_{(3\times1)} \\ 0_{(1\times3)} & 1_{1\times1} \end{pmatrix} = \begin{pmatrix} b_{11} & b_{12} & b_{13} & b_{14} \\ b_{21} & b_{22} & b_{23} & b_{24} \\ b_{31} & b_{32} & b_{33} & b_{34} \\ 0 & 0 & 0 & 1 \end{pmatrix} \tag{2.8}$$

where

$b_{11} = a_{11}c\theta_3 + a_{12}c\beta_1\, s\theta_3 + a_{13}s\beta_1\, s\theta_3$; $b_{12} = -a_{11}s\theta_3 + a_{12}c\beta_1\, c\theta_3 + a_{13}s\beta_1\, c\theta_3$

$b_{13} = -a_{12}s\beta_1 + a_{13}c\beta_1$; $b_{14} = -a_{12}rs\beta_1 + a_{13}rc\beta_1$

$b_{21} = a_{21}c\theta_3 + a_{22}c\beta_1\, s\theta_3 + a_{23}s\beta_1\, s\theta_3$; $b_{22} = -a_{21}s\theta_3 + a_{22}c\beta_1\, c\theta_3 + a_{23}s\beta_1\, c\theta_3$;

$b_{23} = -a_{22}s\beta_1 + a_{23}c\beta_1$; $b_{24} = -a_{22}rs\beta_1 + a_{23}rc\beta_1$

$b_{31} = a_{31}c\theta_3 + a_{32}c\beta_1\, s\theta_3 + a_{33}s\beta_1\, s\theta_3$; $b_{32} = -a_{31}s\theta_3 + a_{32}c\beta_1\, c\theta_3 + a_{33}s\beta_1\, c\theta_3$

$b_{33} = -a_{32}s\beta_1 + a_{33}c\beta_1$; $b_{34} = -a_{32}rs\beta_1 + a_{33}rc\beta_1$

In which a_{ij} are the elements of the Eq. (2.5). r is the radial displacement (palpating motion) of the moving platform $\{X_m Y_m Z_m\}$ with respect to point O as shown in Figure 2-7.

Eqs. (2.2) and (2.6) describe the relationship between angles β_1 and β_2 and their corresponding angles θ_1 and θ_2. Input shafts of the pantographs are connected to their corresponding actuators by cable drives with transmission ratio one (see Figure 2-3). Therefore, we have: $\theta_1^m = \theta_1$ and $\theta_2^m = \theta_2$

Due to use of universal telescoping joint, rotational position θ_3 is different from its corresponding motor's position θ_3^m (see Figure 2-8a). However, they are not constant-velocity joints (Sclater and Chironios 2001; Johnson and Willems 1993) meaning that input and output velocities of the joint are different. Consequently, this effect shows itself in the universal telescoping joints used for the third and fourth DoFs.

With reference to Figure 2-8a, the velocity difference in a universal telescoping joint can be removed if two yokes on the telescoping joint lie in one plane and $\phi_1 = \phi_2$. Thus, the transmission ratio between the actuator's angle θ_3^m and the ultrasound probe θ_3 is one. In the present wrist design, the yokes on the telescoping joint are located in one plane. However, the deflection angles ϕ_1 and ϕ_2 are not equal. The relationship between θ_3^m and θ_3 is (Johnson and Willems 1993):

$$\tan\theta_3 = \tan\theta_3^m \frac{\cos\phi_1}{\cos\phi_2} \tag{2.9}$$

Angles ϕ_1 and ϕ_2 are the deflection angles of the upper and lower universal joints, respectively (see Figure 2-8), and can be calculated in triangle ORQ as:

$$\phi_1 = \sin^{-1}(\sin\psi.\frac{OR}{QR}) \tag{2.10}$$

$$\phi_2 = \pi - \sin^{-1}(\sin\psi.\frac{OQ}{QR}) \tag{2.11}$$

where lengths OR and OQ are selected in the current design as 420, 688 mm, respectively (see Figure 2-8a). With reference to Figure 2-8, $OPRS$ is a cone covered by a portion of a sphere created by two pantographs in which O is the RCM and the angle 2ψ is the vertex angle of the cone. QP and QT are the lengths of the universal telescoping joint in fully extended and retracted configurations, respectively. Angle ψ in Figure 2-8a, is the angle between axes Z_0 and Z_2 (see Figure 2-7) and can be obtained by:

$$\cos\psi = \frac{u_{Z_0} . u_{Z_2}}{|u_{Z_0}||u_{Z_2}|} = -a_{32}s\beta_1 + a_{33}c\beta_1 \tag{2.12}$$

In Eq. (2.12), u_{Z_0} and u_{Z_2} are unit vectors along axes Z_0 and Z_2 described in the fixed frame $\{X_0 Y_0 Z_0\}$.

Equations (2.9), (2.10), (2.11) and (2.12) are now used to show the difference between the actuator rotation and the rotational position of the ultrasound probe at different orientation, ψ, (see Figures 2-8a and 2-8b).

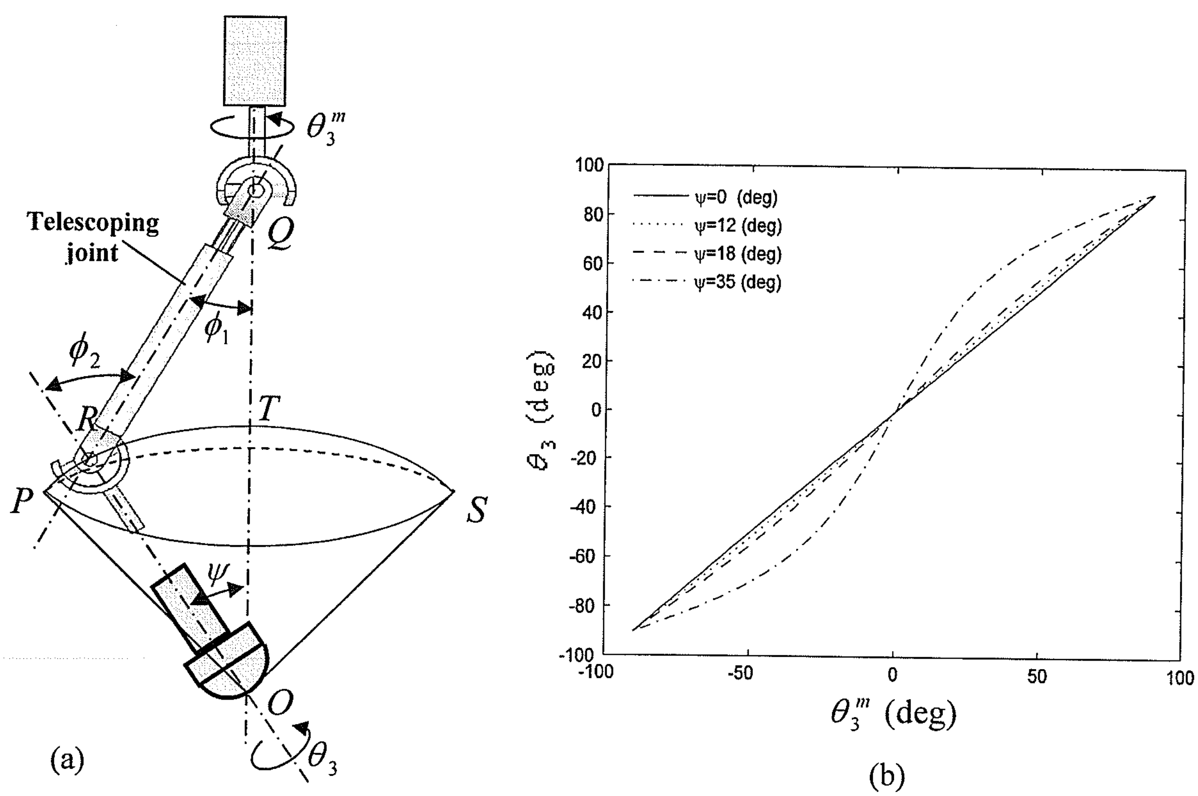

Figure 2-8. (a) Orientation of probe and universal telescoping joint; (b) variation of probe rotation, θ_3, versus motor rotation, θ_3^m, at different orientation, ψ, of probe.

The radial displacement, r, is due to converting the rotational motion of the inner universal telescoping joint connected to multi-jaw coupling into palpating motion of the probe (see Figure 2-6), which can be obtained from the following relationship (Berezovsky et al.1988):

$$r = \frac{nP\theta_4}{2\pi} \tag{2.13}$$

where $n=1$ and $P=4$mm are the number of starts and pitch of the ball screw, respectively. θ_4 is the input rotational motion of the ball screw. Due to use of universal telescoping joint for the third DoF, input rotational position θ_4 is also slightly different from its corresponding motor's position, θ_4^m. Therefore, we have:

$$\tan\theta_4 = \tan\theta_4^m \frac{\cos\phi_1}{\cos\phi_2} \tag{2.14}$$

The relationship between the actuator and the ultrasound probe velocities can be found by applying a loop-closure method described by Tsai (1999) and kinematic relations outlined above:

$$\begin{bmatrix}\vec{\omega} & \vec{V}\end{bmatrix}^T_{(6\times1)} = \begin{bmatrix}J\end{bmatrix}_{(6\times4)} \cdot \begin{bmatrix}\dot{\theta}_1^m & \dot{\theta}_2^m & \dot{\theta}_3^m & \dot{\theta}_4^m\end{bmatrix}^T \tag{2.15}$$

$[\dot{\theta}_1^m, \dot{\theta}_2^m, \dot{\theta}_3^m, \dot{\theta}_4^m]$ and $[\vec{\omega}\ \vec{V}]^T$ are actuators angular velocities and ultrasound probe velocities, respectively. Detailed derivation of the Jacobian matrix, J, is given in Appendix B. The velocity state of the tip of the ultrasound probe based on actuator's velocities is simulated for the full range of motions of all motors, i.e., from $[-35°, -35°, -90°, -90°]$ to $[35°, 35°, 90°, 90°]$with constant speed (see Figures 2-9). The speed of each joint is selected so that the complete range of each joint is traveled in 10 seconds.

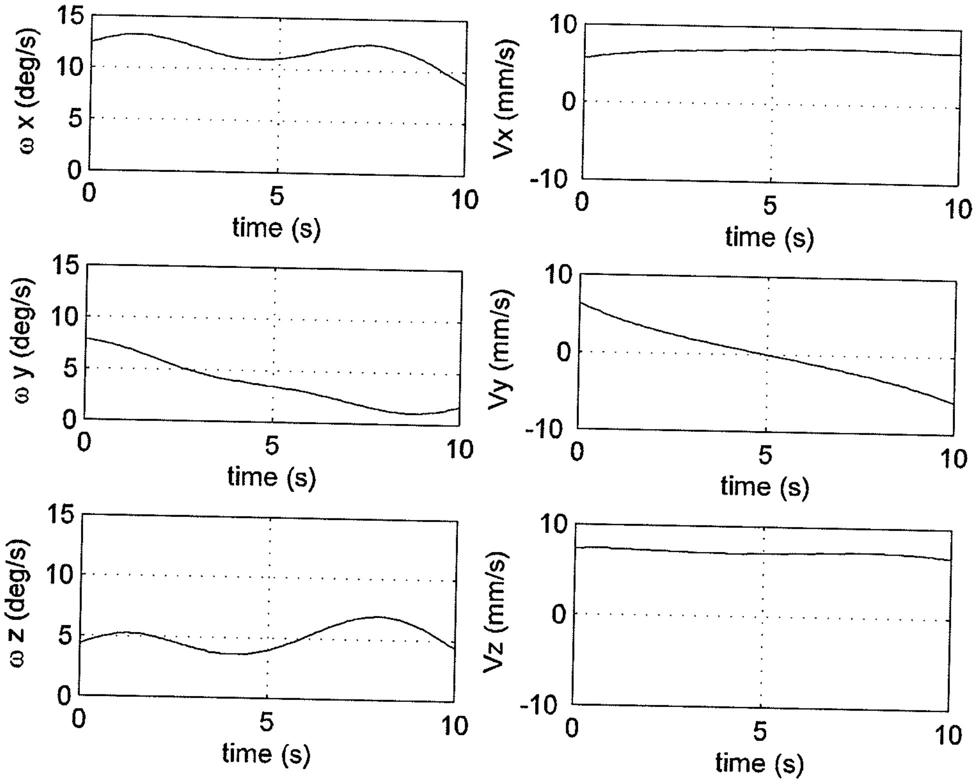

Figure 2-9. Variation of velocity vector of probe.

Singularity Analysis

An important limitation of parallel manipulators is that singular configurations may exist within its workspace where the manipulators gain or lose one or more DoFs. In this Section singular configurations of the proposed wrist are investigated and it is shown that the proposed wrist provides a singularity-free workspace. For pantograph mechanisms, singular configurations happen only when points O, E, and B_1 (see Figure 2-10a) lie on a straight line, which makes each pantograph in a fully-stretched or folded-back position. In this configuration, the wrist loses one DoF. At the same time, if both pantographs rotate until EF lie in a plane consisting axes A_1B_1 and A_2B_2, it creates four possible configurations for the wrist mechanism. In these configurations, the mechanism gains one more DoF, i.e., the ultrasound probe gains small motions even though the pantograph's actuators are locked. It is seen that, all singular configurations occur at the boundary of the great circle of the hemisphere which is physically unreachable by the ultrasound probe. Therefore, this type of mechanism creates a singularity-free workspace for the ultrasound probe.

Universal telescoping joints of the third and fourth DoFs follow the spherical motion generated by the first two DoFs idly. Singularity configurations simply occur when the deflection angles of each universal joint becomes 90°. Figures 2-10b and 2-10c show singular configurations of the universal telescoping joint. In Figure 2-10, configuration (b) can not happen because OR is designed to be less than OQ. In order to avoid singular configuration (c) in the middle of the workspace of the pantographs, the following design condition must be met once dimensions OR and OQ are chosen.

$$\psi + \phi_1 > 90° \tag{2.16}$$

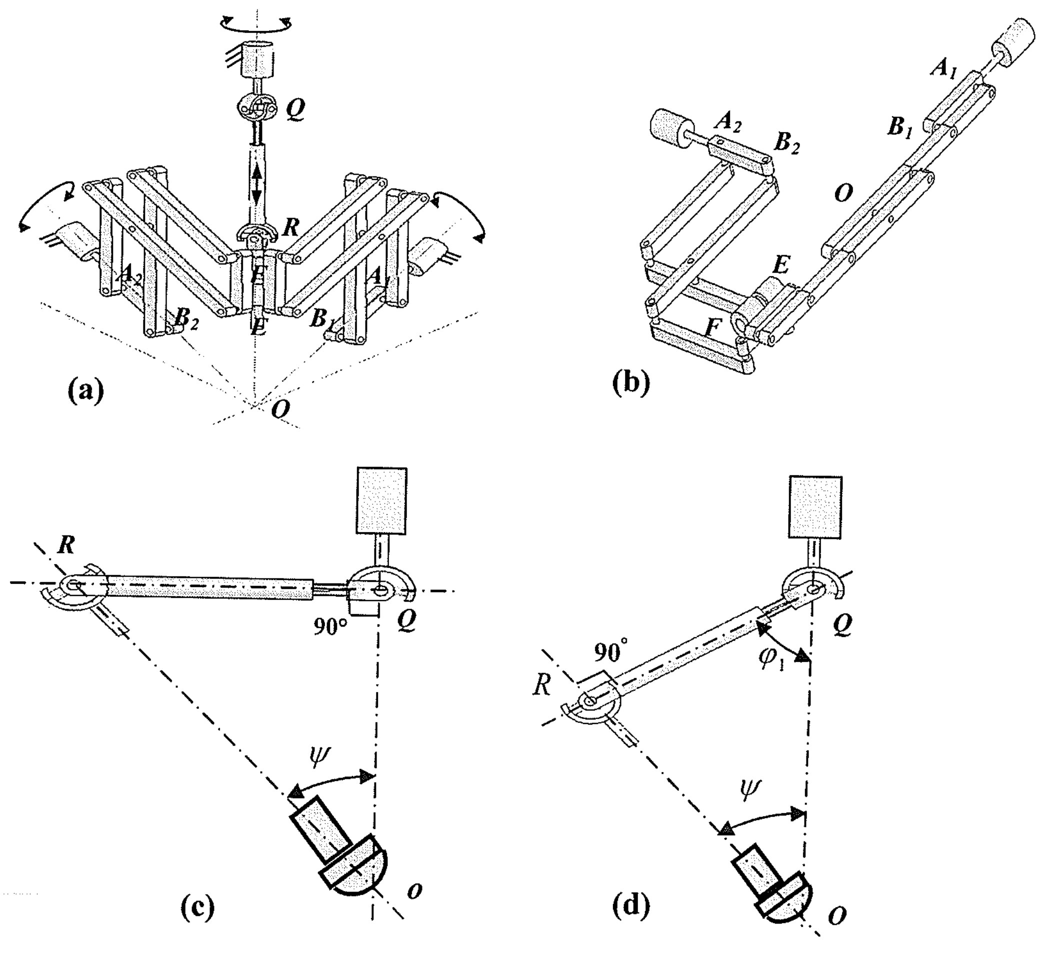

Figure 2-10. (a) Simplified structure of wrist (b) singular configuration of pantograph; (c) geometrically impossible singular configuration of telescoping joint; (d) possible singular configuration of telescoping joint.

2.4 Prototype Device

Figure 2-11 shows the prototype of the wrist. The pantographs create the first two DoFs of the wrist. These two DoFs generate yaw and pitch motions of the ultrasound probe about RCM. The third DoF is a palpating motion in order to maintain the contact between the probe and the patient. The fourth DoF generates a rotational motion of the probe about its axis. .

The wrist structure is made of ordinary aluminum except for the shafts which are made of steel. The weight of the moving elements of the 4-DoF wrist is approximately 2.5 kg. The inertia matrix of the prototyped 4-DoF wrist has been calculated at the center of mass using "SolidWorks" software package.

$$\begin{pmatrix} I_{xx} & -I_{xy} & -I_{xz} \\ -I_{yx} & I_{yy} & -I_{yz} \\ -I_{zx} & -I_{zy} & I_{zz} \end{pmatrix} = \begin{pmatrix} 63.0 & -33.8 & 7.2 \\ -33.0 & 39.1 & -15.0 \\ 7.2 & -15.0 & 80.0 \end{pmatrix} \times 10^{-3} \text{ kg.m}^2$$

The footprint and height of the wrist is (192 mm$\times$192 mm), and 750 mm, respectively. The nominal workspace of the ultrasound probe is a cone with 50° as vertex angle. This workspace is achieved by replacing ordinary shafts with the crank-shafts allowing the linkages to pass through the centerline of the shafts. Other specifications of the 4-DoF robotic wrist are given in Table 2-1. Each DoF is driven by a permanent magnet brushed DC motor equipped with planetary gearbox and a digital encoder (2000 counts/Rev). In this prototype, two of the actuators are directly connected to input shaft of each pantograph.

Table 2-1. General specifications of prototype 4-DoF ultrasound robotic wrist.

Axis	Range of motion	Motor	Gear ratio	Motor torque/force
Yaw	± 25°	Maxon RE 36	111:1	88.5 mNm
Pitch	± 25°	Maxon RE 36	111:1	88.5 mNm
rotation	± 90°	Maxon RE 25	84:1	29.3 mNm
palpation	32 mm	Maxon RE 25	84:1	24 N (measured)

Proportional and derivative control scheme is used to drive each electric motor. Typical step responses for DC motors are shown in Figures 2-12 to 2-15. First, proportional gains were tuned to achieve a satisfactory performance based on steady-state error and transient response. In the next stage, derivative gains were tuned to modify the transient responses. One axis force sensor[2] (LCMKD 50 N, by Omega) is mounted between the ultrasound probe and the end-effector of the wrist. The force sensor directly measures the contact force between ultrasound probe and patient's body. The measurement information can either be used in wrist local force control or be transmitted to the remote force-reflecting hand-controller to provide force feedback to the physician.

[2] The maximum amplitude of the force-sensor noise was measured and is equal to 0.1 N. The measured forces by the force sensor goes through a first order low pass filter with cut-off frequency of 1 Hz. The average applied force to patient's body by the ultrasound probe during a typical kidney examination is 0.5 N.

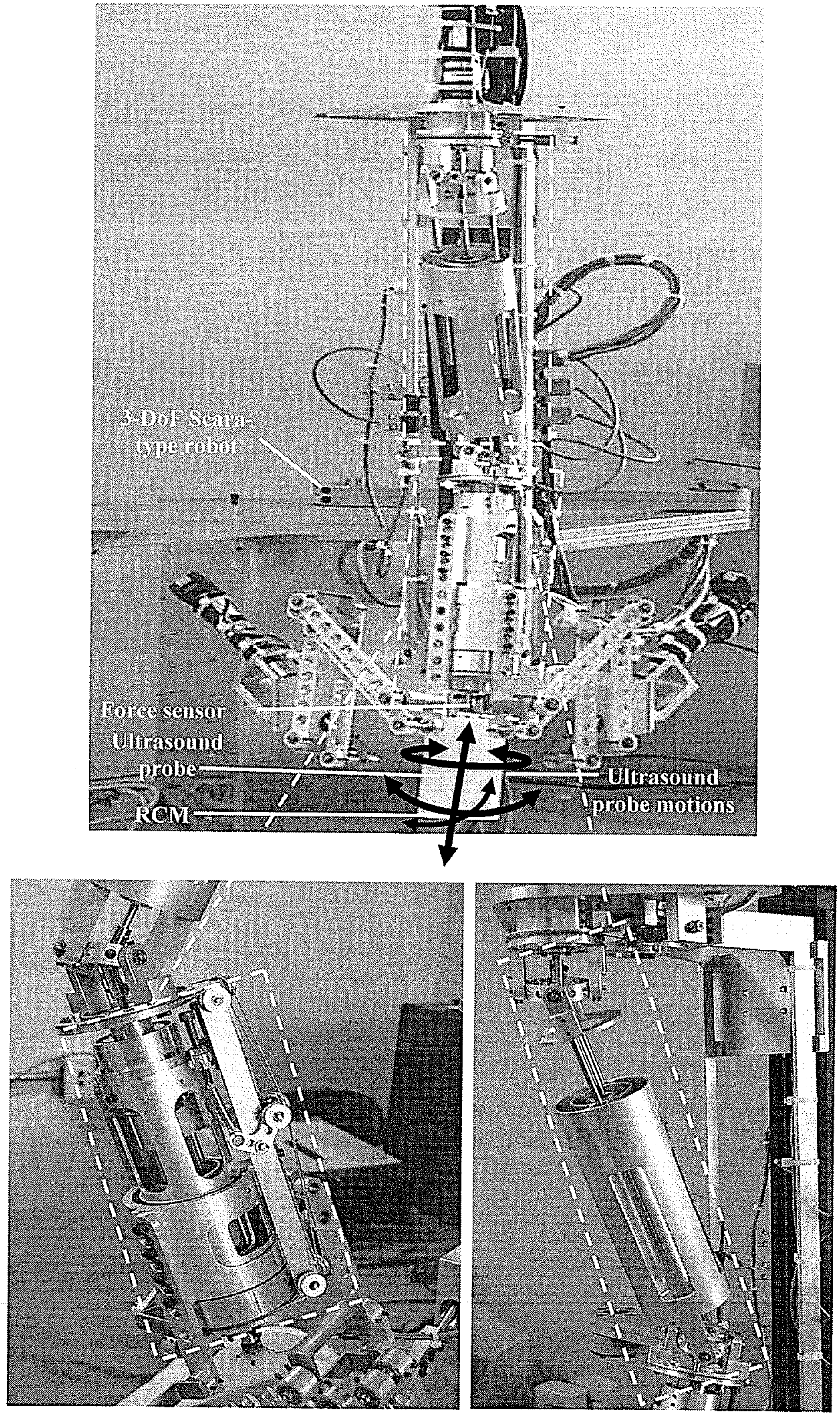

Figure 2-11. 4-DoF robotic wrist for remote ultrasound diagnosis.

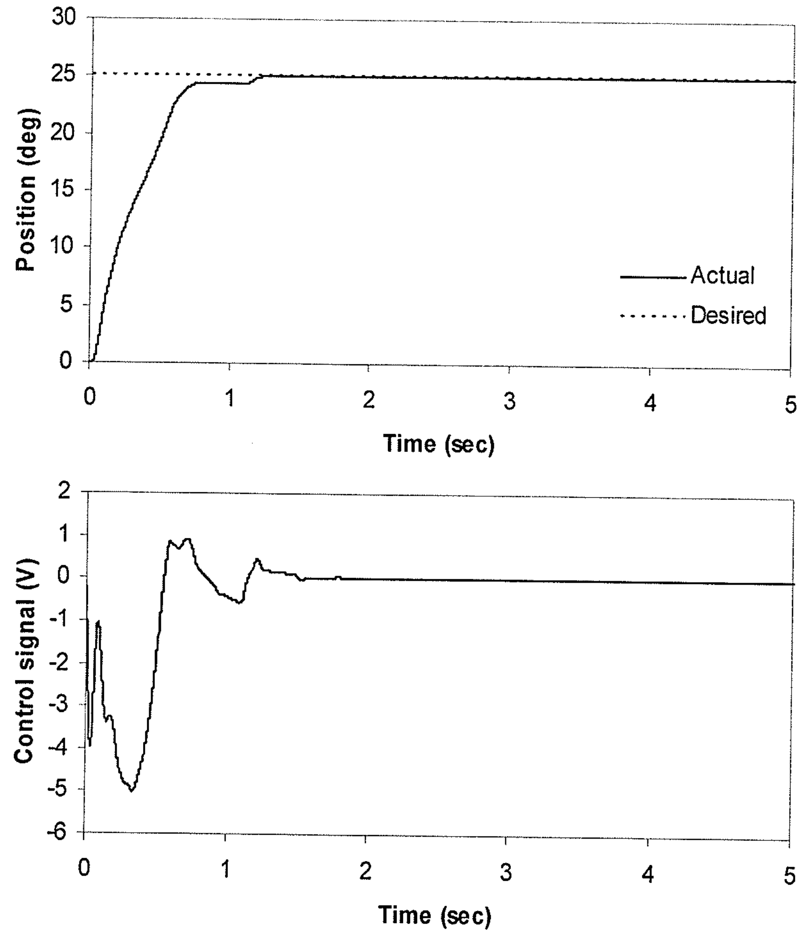

Figure 2-12. Step input response of power train producing yaw scanning motion using PD control scheme (K_p= 1.4 V/deg and K_v = 0.06 Vs/deg).

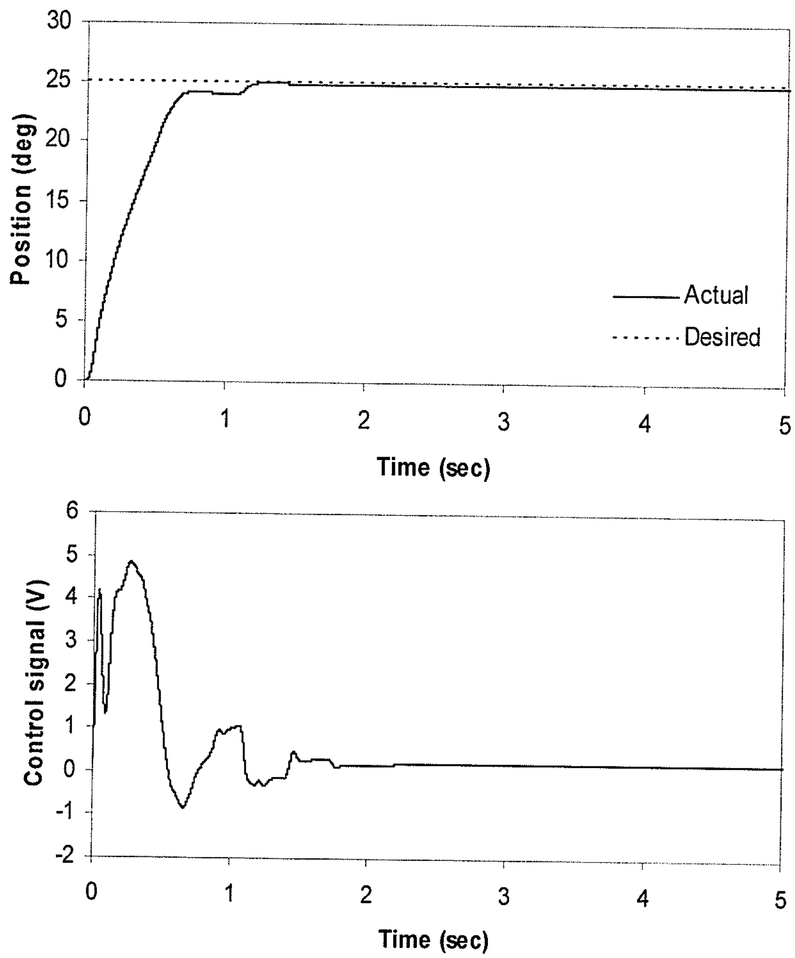

Figure 2-13. Step input response of power train producing pitch scanning motion using PD control scheme (K_p= 1.4 V/deg and K_v = 0.06 Vs/deg).

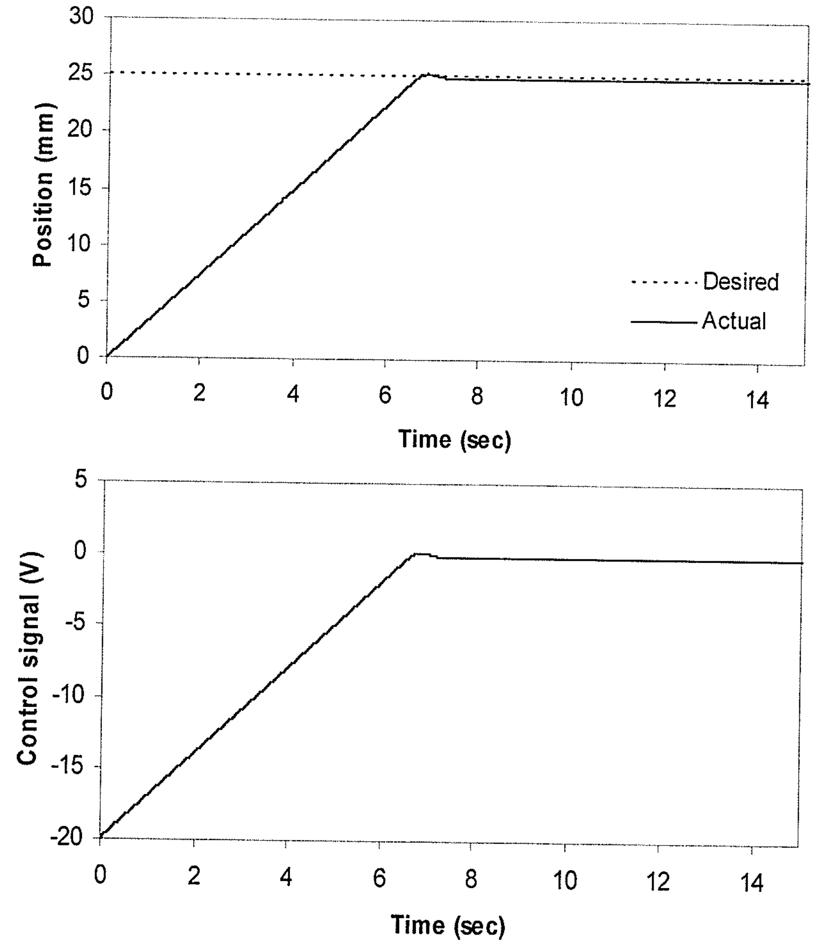

Figure 2-14. Step input response of power train producing palpating motion using PD control scheme (K_p=0.8 V/mm and K_v=0.03 Vs/mm).

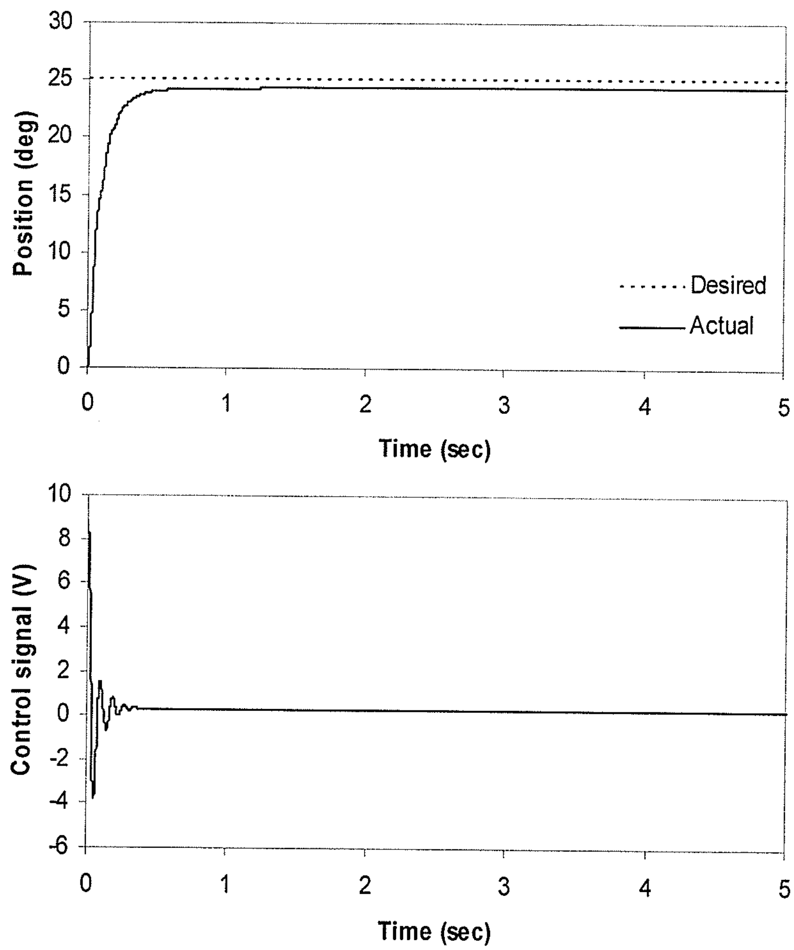

Figure 2-15. Step input response of power train producing rotational scanning motion along the axis of probe using PD control scheme (K_p = 0.3 V/deg and K_v = 0.03 Vs/deg).

2.5 Summary

A novel 4-DoF robotic wrist for remote ultrasound imaging has been designed and constructed. The proposed wrist has a set of specifications which make it suitable for ultrasound diagnosis. It has 4 degrees of freedom (DoFs) built upon parallel mechanisms to provide main clinical motions of the probe required for ultrasound imaging and has a remote center-of-motion (RCM) which is located outside the mechanism. The existence of a RCM in the kinematic chain of the mechanism enables the wrist to perform the 3-D ultrasound imaging with 4 DoFs. All DoFs are kinematically decoupled from each other. Kinematic decoupling improves the safety of the manipulation by generating each motion of the ultrasound probe by actuating a single kinematic chain. The workspace produced by the proposed wrist is singularity-free and all actuators are placed on the ground to reduce inertia of moving elements and to simplify disinfection-procedure. The wrist allows a reasonable access to the patient by attending nurse. There is no contact between moving elements of the wrist and patient's body except at the tip of the ultrasound probe. These features (remote center-of-motion parallel mechanism, decoupled DoFs, and singularity-free workspace) have not been simultaneously considered in the robotic systems developed prior to this work and described in Section 1.4.1.

Chapter 3

Design of Ultrasound Haptic Device[1]

This Chapter describes the development of a 4-DoF force reflecting hand-controller to enable physicians to remotely manipulate the ultrasound wrist described in the previous Chapter. The basis structure of the haptic device is described that satisfies the objectives outlined in Section 1.5. Detailed design, Kinematics analysis, force analysis, prototyping, and technical performance evaluation of the haptic device are also presented.

3.1 Embodiment Design

The 4-DoF haptic device is shown in Figure 3-1. It has been designed to meet the requirements outlined in Section 1.5. For the first two DoFs, two eight-bar parallel mechanisms are mounted on the fixed plate to produce the hemispherical motion of the hand-grip about the FCM. The eight-bar mechanisms are connected together by a revolute joint.

The third DoF provides a sliding motion along the axis of the hand-grip. With reference to Figure 3-1b, the power train for the third DoF consists of an actuator, a universal joint and a cable drive. The input of the universal joint is connected to the output of the cable reducer. The center of the universal joint coincides with the FCM. The rotational motion of the actuator and the universal joint is converted into the sliding motion of the hand-grip by a cable drive. The cable drive consists of driver and driven pulleys, frame, cable and hand-grip. The drive pulley is fixed to the connecting shaft of the universal joint and its rotational motion is decoupled from the frame by decoupling ball bearings inside the frame (not shown). Therefore, the driver pulley rotates freely on

[1] Some material of this Chapter has been published in :
Najafi, F. and Sepehri N. (2008). A novel hand-controller for remote ultrasound imaging. *Mechatronics*, 18(10): 578-590.

the frame while driving the cable. One side of the cable is fixed to the hand-grip which slides on a ball spline shaft. The universal joint allows the cable drive to follow the spherical motion generated by parallelograms, while transmitting actuator's rotary motion into the sliding motion of the hand-grip. The eight-bar parallelogram mechanisms carry the weight of the third DoF's power train. Additionally, the interaction forces between user's hand and the hand-grip is distributed among the eight-bar parallelogram mechanisms.

Rotational motion of the hand-grip (fourth DoF) is measured by an encoder (Figure 3-1b). The center of gravity of the mechanism is located on the axis of the hand-grip regardless of the orientations of the device. The total mass of the eight-bar mechanisms and cable drive is statically balanced by a zero-free-length tension spring which will be described next. Each power train in the parallel mechanism can be equipped with base-mounted actuator to provide force feedback along each motion of the ultrasound probe.

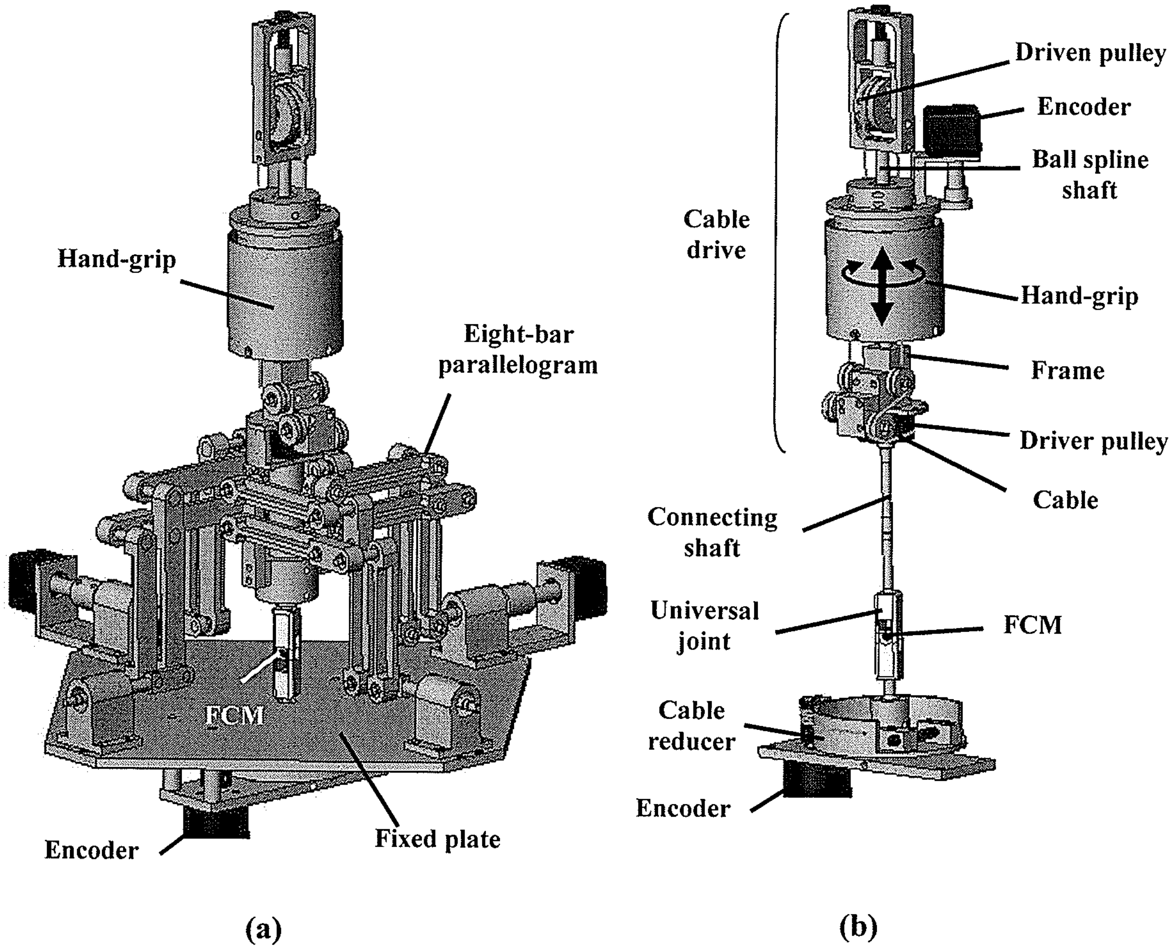

Figure 3-1. 4-DoF force-reflecting hand-controller: (a) general view of device; (b) power train of the third and fourth DoFs producing sliding and rotational motions of hand-grip.

3.2 Design for Static Balancing

Static balancing techniques for mechanisms can be categorized as active or passive. Active balancing utilizes electric, pneumatic, or hydraulic actuators (Rivin 1988). For example, Agrawal et al. (2001) described the design of an active gravity balanced planner mechanism, where auxiliary parallelograms were used to physically locate the center of the mass of the mechanism.

Passive balancing uses springs or counterweights. Counterweight balancing ensures that the center of mass of the mechanism remains fixed for every configuration of the mechanism. Counterweight balancing has been used in the 3-DoF parallel haptic device by Steger et al. (2004). In some haptic devices, the weights of the electric actuators were used as counterweights (Hayward et al. 1998). However, using counterweights, the overall inertia of the device will increase.

Static balancing using tension springs ensures that the total potential energy of the mechanism is constant at every configuration of the mechanism. Tension springs have the advantage of low inertia and high output force over using counterweights (Herder 2002). This will result in increased bandwidth and acceleration and decreased actuator size.

A combination of spring, cam, and cables can also be used to statically balance the weight of mechanisms when the center of gravity changes on a predefined path in space (Tidwell et al. 1994; Kobayashi 2001). Static balancing of parallel manipulators using counterweights or springs has been thoroughly studied by Wang and Gosselin (1999, 2000) in which 3, 4 and 6 DoF parallel manipulators were statically balanced using 2, 5 and 12 tension springs, respectively.

In this thesis, a tension spring is used to statically balance the weight of the hand-controller. Thus, to provide insight into static balancing using springs, the conditions associated with a single body pivoting on a spherical joint are described based on the method presented by Gosselin (1999). With reference to Figure 3-2, the body with mass, m, is mounted on a 3-DoF spherical joint, O. The center of mass is located at the tip of line OC. A fixed coordinate frame $\{X_0Y_0Z_0\}$ is attached to the base with its origin in O and its Z_0 axis pointing in the direction opposite to the gravitational acceleration vector.

It is possible to choose attachment points and stiffness, K, for the spring to obtain a statically balanced system for any orientation of the body with mass m. The conditions for balancing are obtained by imposing that the total potential energy including gravitational and elastic be constant with respect to orientation of the moving body. According to Gosselin (1999), for mechanism shown in Figure 3-2, we have

$$\left|\overrightarrow{OC}\right| = \frac{K\left|\overrightarrow{OA}\right|\left|\overrightarrow{OB}\right|}{mg} \tag{3.1}$$

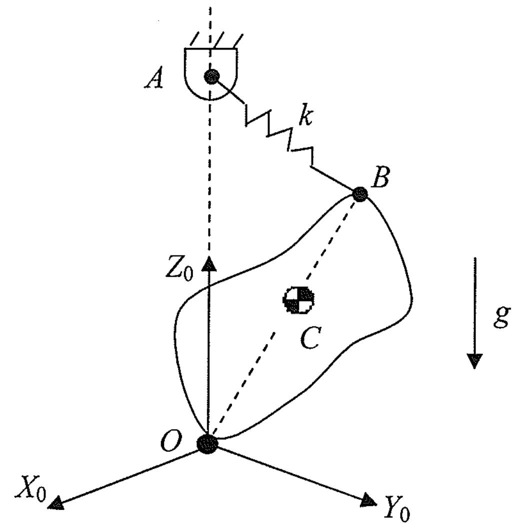

Figure 3-2. Spherical 3-DoF single-body mechanism balanced with one spring (Gosselin 2000).

Equation (3.1) shows that a 3-DoF body that can undergo arbitrary pure rotations about a fixed spherical joint can be balanced for all configurations using a single spring (Gosselin 1999). The total potential energy in the system remains constant for any orientation of the body, and hence the system can be brought to a static equilibrium without any external force or torque. Note that, the complete static balancing of the mechanisms using tension springs is only possible when the un-stretched length of the spring is equal to zero. There is no tension spring that has such a capability. However, such an elastic element can be realized by a combination of tension spring, cable and pulleys as shown in Figure 3-3.

To fully take advantage of the above balancing method in the design of the hand-controller presented here, the overall center of gravity must move on a sphere. Combining two eight-bar parallelogram mechanisms on two perpendicular planes allows the overall center of gravity to move on a sphere over the entire workspace (Figure 3-4a). This unique characteristic is achieved by knowing that the diagonals of a four-bar parallelogram mechanism bisect each other, and the center of gravity always remains on the intersection of the diagonals, and moves on a circle. Furthermore, in order to increase the rigidity, four-bar parallelograms are combined together as shown in Figure 3-4b. In the resulting eight-bar mechanism, the distance between the center of gravity and the center of base link remains constant at different orientations of the mechanism. Therefore, the resulting multi-linkage mechanism behaves similar to a rigid body connected to ground by a spherical joint, and can be statically balanced by a zero-free-length tension spring as in Figure 3-3. Figure 3-5 shows how the hand-controller mechanism is statically balanced using a zero-free-length tension spring.

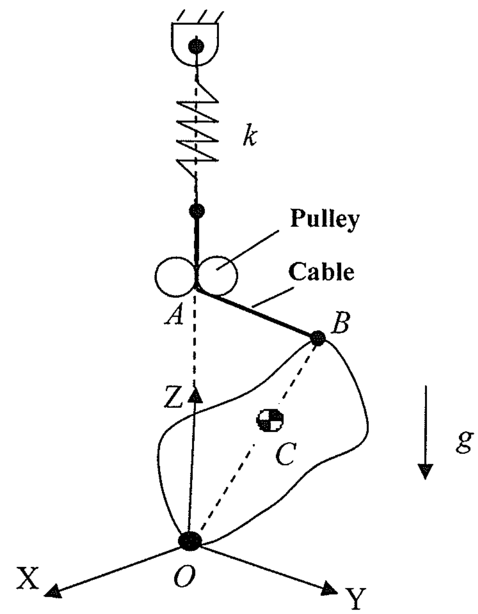

Figure 3-3. Implementation of a zero-free-length tension spring.

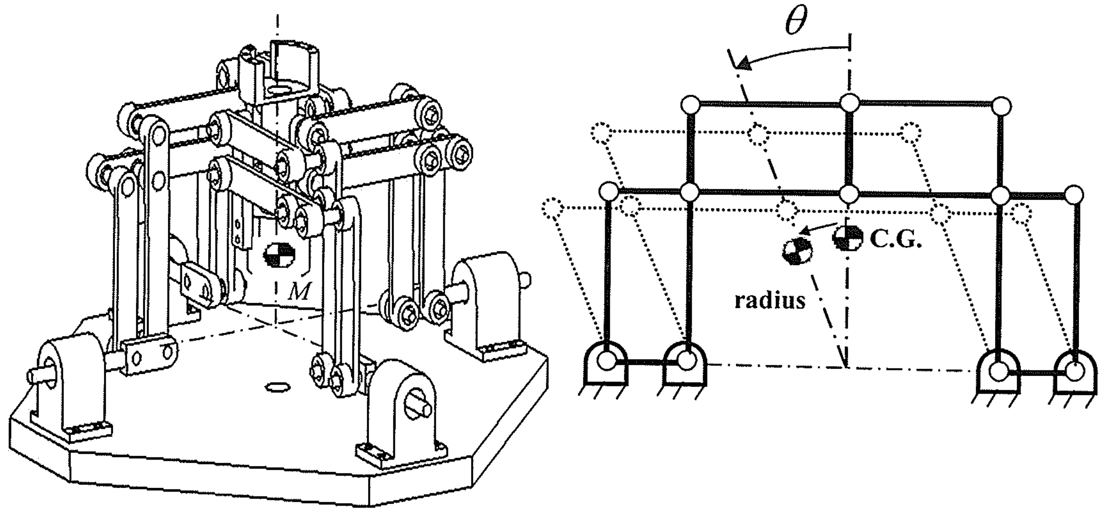

(a) (b)

Figure 3-4. Static balancing of two symmetric eight-bar mechanisms: (a) two symmetric mechanisms on two perpendicular planes with center of gravity moving on a sphere for all configurations; (b) center of gravity moves on a circle at different orientation of each eight-bar mechanism.

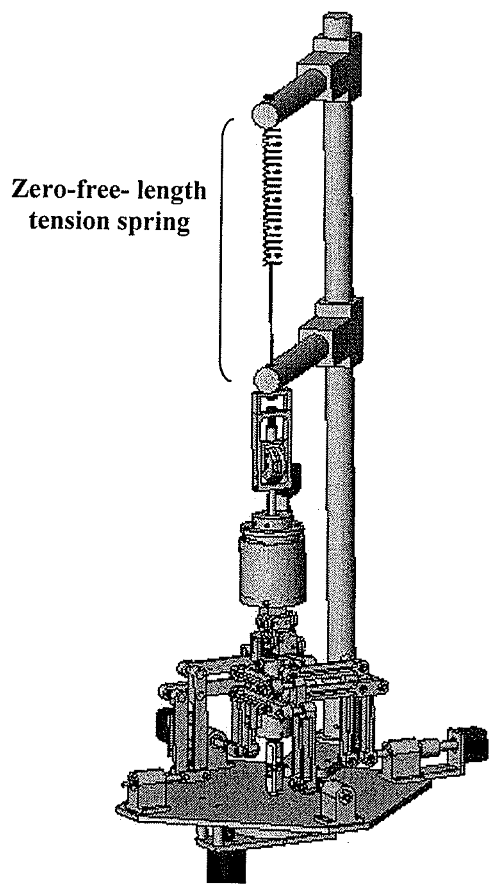

Figure 3-5. Static balancing of hand-controller with zero-free-length tension spring.

3.3 Remarks

Remark 1- The structure of the proposed mechanism can be altered by changing or reducing the number of linkages. Figure 3-6b shows asymmetric version of the device. This mechanism uses two six-bar pantograph mechanisms which is simpler than the mechanism in Figure 3-6a. Figure 3-6c shows a version which uses two double-parallelogram mechanisms located in two perpendicular planes. A much simpler configuration uses two two-link mechanisms (Figure 3-6d). All links can also be removed which leads to the mechanism shown in Figure 3-6e. The footprint of the mechanisms reduces from configurations 3a to e. Mechanisms shown in Figures 3-6a, 3-6c and 3-6e can be statically balanced by a single tension spring. Mechanisms in Figures 3-6b and 3-6d have simpler structures, but cannot be balanced with a spring. The mechanism shown in Figure 3-6e can only provide force feedback along the axis of the hand-grip. Measurement of joint axis in other DoFs can be challenging in this mechanism. The mechanism in Figure 3-6a has higher structural rigidity than the one shown in Figure 3-6c and was chosen in this work. Comparisons between all configurations are summarized in Table 3-1.

Table 3-1. Comparison between design configurations.

	Design a				Design b				Design c				Design d				Design e			
Static balancing with spring	√				-				√				-				√			
Structural simplicity	√				√√				√√				√√√				√√√√ (simplest)			
Possibility of providing of force feedback (pitch (1), yaw (2), palpation (3) and rotation (4) axes)	1	2	3	4	1	2	3	4	1	2	3	4	1	2	3	4	1	2	3	4
	√	√	√	-	√	√	√	-	√	√	√	-	√	√	√	-	-	-	√	-
Footprint	√				√√√				√√				√√√				√√√√ (Smallest)			

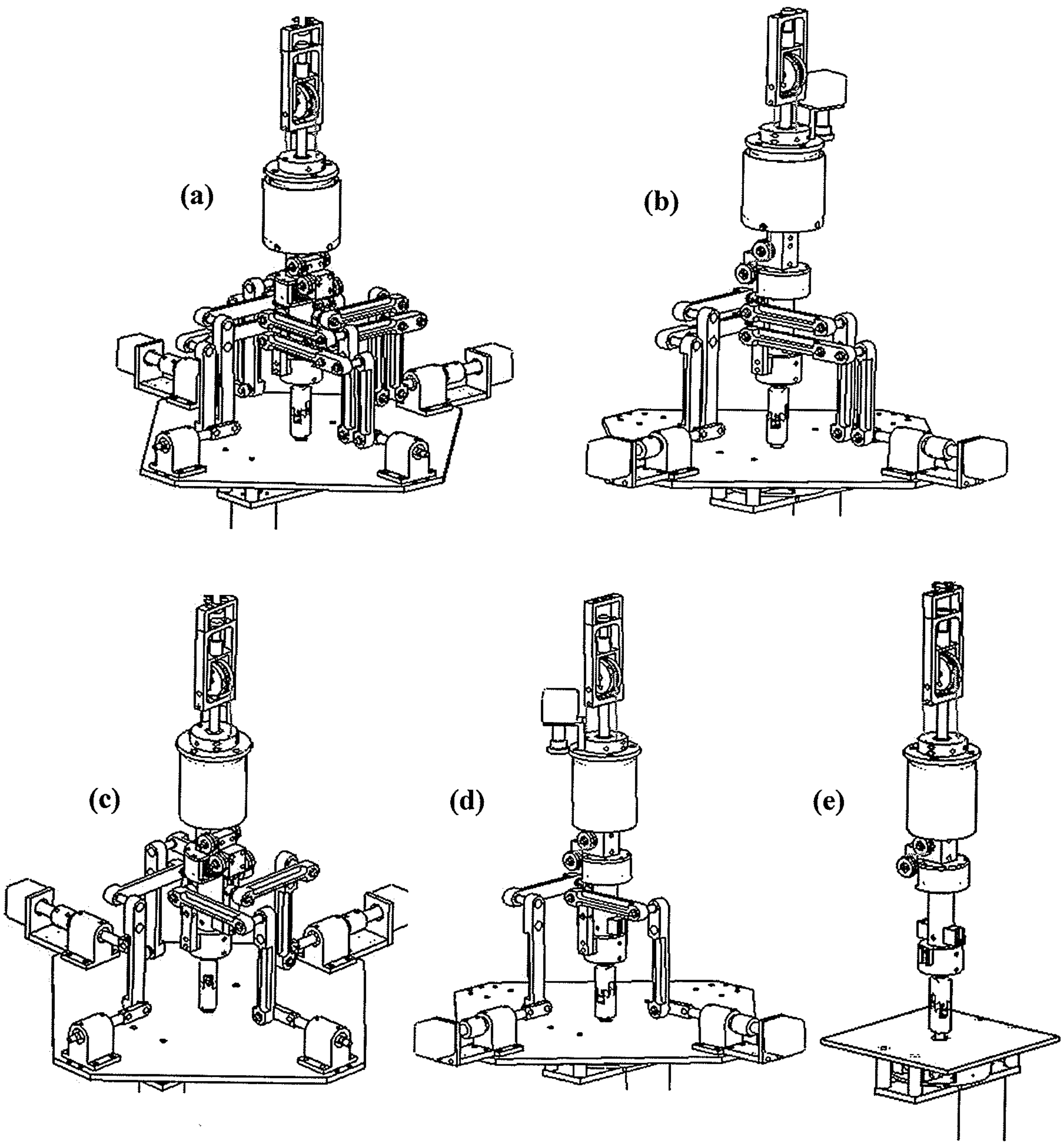

Figure 3-6. Possible configurations: (a) symmetric eight-bar mechanisms; (b) asymmetric six-bar pantograph mechanisms; (c) symmetric double-parallelograms; (d) asymmetric parallelograms; (e) one DoF sliding motion.

Remark 2- One may argue that using symmetric mechanisms as in Figures 3-6a and 3-6c, adds more weight and inertia to the haptic mechanism as compared to the asymmetric mechanisms shown in Figures 3-6b and 3-6d. Here we show that given the same structural stiffness, the symmetric mechanism becomes lighter than asymmetric one. A simple model of six-bar and two-link mechanisms shown in Figures 3-6b and 3-6d is a cantilever beam shown in Figure 3-7a. A simple model of eight-bar and double parallelogram mechanisms shown in Figures 3-6a and 3-6c is a cantilever beam fixed at both ends shown in Figure 3-7b. The maximum deflections of models at points $A1$ and $A2$ under static force, F, are given by (Popov 1976):

$$Y_{A1} = \frac{Fl_1^3}{3EI_1} \tag{3.2a}$$

$$Y_{A2} = \frac{Fl_2^3}{192EI_2} \tag{3.2b}$$

where E, and $I_i = b_i h_i^3/12$ $(i=1,2)$ are modulus of elasticity and area moments of inertia, respectively. If the models have the same structural deflection, i.e., $Y_{A1} = Y_{A2}$, the relation between widths of the beams should be $b_1 = 8b_2$, assuming $h_1 = h_2$. In this case, the model shown in Figure 3-7a is four times heavier than the second model in Figure 3-7b, i.e. $m_1 = 4m_2$. In terms of mass moments of inertia, $I_{ixx} = \frac{1}{12} m_i (b_i^2 + h_i^2)$, $(i=1,2)$ comparison between I_{1xx} and I_{2xx} assuming $m_1 = 4m_2$ and $b_1 = 8b_2$ reveals that $I_{1xx} > 4I_{2xx}$. Therefore, the symmetric mechanism shown in Figure 3-7b can be designed four times lighter than the asymmetric mechanism in Figure 3-7a, but with the same structural stiffness. Furthermore, the open-loop or mechanical bandwidth, $\omega_n = \sqrt{k/m}$, of the symmetric mechanism, $\omega_{2n} = \sqrt{k/m_2}$, is two times greater than the one belonging to the asymmetric mechanism, $\omega_{1n} = \sqrt{k/m_1}$, since they have the same structural stiffness k.

Remark 3- Designs presented in Figures 3-6a and 3-6c have uniform structures leading to uniform distribution of reaction forces at the joints. This results in uniform friction forces inside revolute joints. Uniform frictional behaviour is a desirable feature in haptic devices since it increases the fidelity of the force reflections (Vlachos et al. 2003).

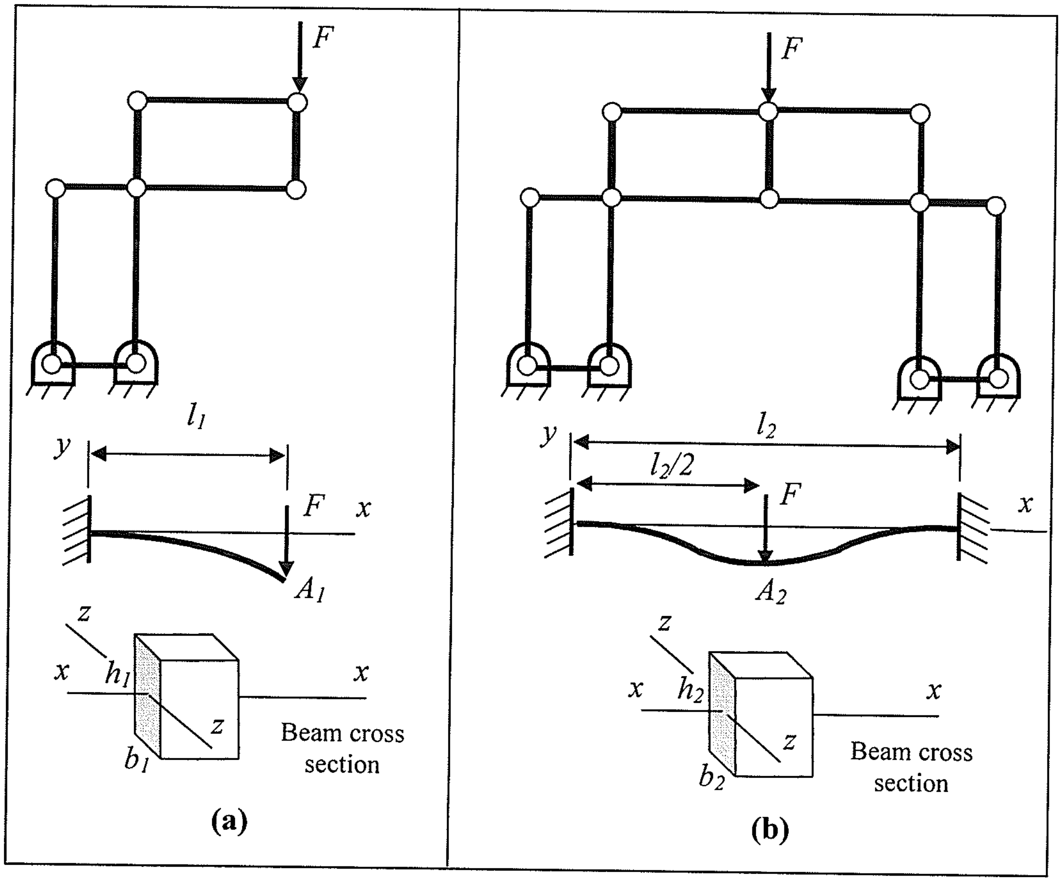

Figure 3-7. (a) Simple model of six-bar pantograph mechanism under load F; (b) simple model of an eight-bar mechanism under load F.

3.4 Kinematics Analysis

In this section, forward kinematics of the mechanism is derived using Euler angles about moving frames. Detailed derivation of Jacobian matrix is presented in Appendix E.

Forward kinematics

With reference to Figure 3-8, frame $\{X_0Y_0Z_0\}$ is attached to point O representing the FCM of the hand-controller. Frame $\{X_mY_mZ_m\}$ is attached to the hand-grip. Initially, the moving frame $\{X_mY_mZ_m\}$ coincides with the fixed frame $\{X_0Y_0Z_0\}$. The first two actuator (motor) rotations θ_1^m and θ_2^m occur about axes X_0 and Y_0 where the pantograph's actuators are located. The rotation θ_4^m occurs about the new axis Z_2 of frame $\{X_2Y_2Z_2\}$, resulted from the first two rotations θ_1^m and θ_2^m. The radial displacement, r, of the hand-grip occurs along axis Z_2.

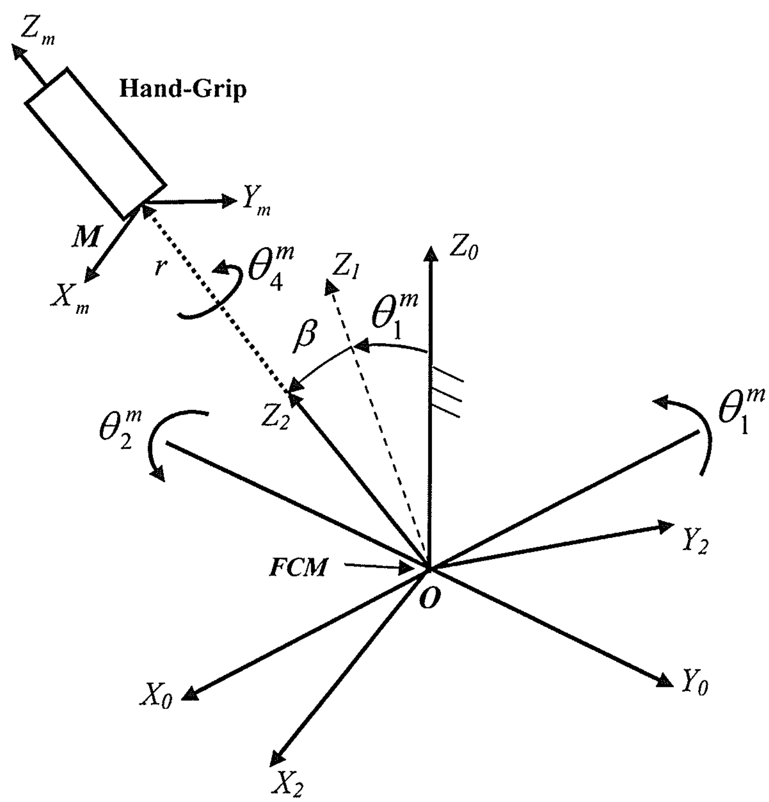

Figure 3-8. Coordinate transformation between fixed frame $\{X_0Y_0Z_0\}$ and moving frame$\{X_mY_mZ_m\}$.

With reference to Figure 3-8, rotation θ_1^m about axis X_0 causes axis Z_0 to reach to axis Z_1. Its rotation matrix can be written as (Tsai 1999):

$$Rot(X_0,\theta_1^m) = \begin{pmatrix} 1 & 0 & 0 \\ 0 & c\theta_1^m & -s\theta_1^m \\ 0 & s\theta_1^m & c\theta_1^m \end{pmatrix} \tag{3.3}$$

where c and s denote 'cosine' and 'sine' functions, respectively.

Rotation θ_2^m about axis Y_0, causes axis Z_1 to rotate about the moving axis Y_1 of moving frame $\{X_1Y_1Z_1\}$ as much as β:

$$Rot(Y_1,\beta)=\begin{pmatrix} c\beta & 0 & s\beta \\ 0 & 1 & 0 \\ -s\beta & 0 & c\beta \end{pmatrix} \tag{3.4}$$

Angle β is obtained from the following relation

$$t\theta_2^m=\frac{t\beta}{c\theta_1^m} \tag{3.5}$$

t in Eq. (3.5) denotes 'tan' function. Detailed derivation of Eq. (3.5) is given in Appendix D. The rotation θ_4^m is about axis Z_2 of moving frame $\{X_2Y_2Z_2\}$. Its rotation matrix can be written as:

$$Rot(Z_2,\theta_4^m)=\begin{pmatrix} c\theta_4^m & -s\theta_4^m & 0 \\ s\theta_4^m & c\theta_4^m & 0 \\ 0 & 0 & 1 \end{pmatrix} \tag{3.6}$$

Therefore, the elements of the homogenous transformation matrix that describes the transformation from frame $\{X_0Y_0Z_0\}$ to $\{X_mY_mZ_m\}$ is:

$$T=\begin{pmatrix} Rot(\theta_1^m,\beta,\theta_4^m)_{(3\times3)} & Rot(\theta_1^m,\beta,\theta_4^m)_{(3\times3)}\begin{pmatrix}0 & 0 & r\end{pmatrix}^T{}_{(3\times1)} \\ 0_{(1\times3)} & 1_{(1\times1)} \end{pmatrix}=\begin{pmatrix} t_{11} & t_{12} & t_{13} & t_{14} \\ t_{21} & t_{22} & t_{23} & t_{24} \\ t_{31} & t_{32} & t_{33} & t_{34} \\ 0 & 0 & 0 & 1 \end{pmatrix}$$

(3.7)

where

$$Rot(\theta_1^m,\beta,\theta_4^m)=Rot(X_0,\theta_1^m)\,Rot(Y_1,\beta)\,Rot(Z_2,\theta_4^m)$$

and

$$t_{11}=c\beta\,c\theta_4^m$$

$$t_{12}=-c\beta\,s\theta_4^m$$

$$t_{13}=s\beta$$

$$t_{14}=r\,s\beta$$

$t_{21} = c\theta_1^m \, s\theta_4^m + s\theta_1^m \, s\beta \, c\theta_4^m$

$t_{22} = c\theta_1^m \, c\theta_4^m - s\theta_1^m \, s\beta \;\, s\theta_4^m$

$t_{23} = -s\theta_1^m \, c\beta$

$t_{24} = -r \, s\theta_1^m \, c\beta$

$t_{31} = s\theta_1^m \, s\theta_4^m - c\theta_1^m \, s\beta \, c\theta_4^m$

$t_{32} = s\theta_1^m \, c\theta_4^m + c\theta_1^m \, s\beta \, s\theta_4^m$

$t_{33} = c\theta_1^m \, c\beta$

$t_{34} = r \, c\theta_1^m \, c\beta$

In Eq. (3.7), r is the radial distance of the hand-grip from point *O*. It is related to the third rotation θ_3^u (see Figure 3-10) as follows:

$$r = \frac{\theta_3^u d_3}{2} \tag{3.8}$$

where d_3 is the diameter of the driver pulley.

Note that due to the universal joint (see Figure 3-10), rotational angle θ_3^u is different from its corresponding actuator angular position θ_3^m. They are however related by the following relationship (Hinkle 1960; Johnson and Willems 1993):

$$t(\frac{\theta_3^m}{n}) = \frac{t\theta_3^u}{c\psi} \tag{3.9}$$

n is cable reduction ratio (see Figure 3-10). ψ is the angle between axes Z_0 and Z_2 shown in Figure 3-8, and can be obtained in terms of actuator rotations from by the following equation:

$$c\psi = c\beta \, c\theta_1^m = c[t^{-1}(c\theta_1^m \, t\theta_2^m)]c\theta_1^m \tag{3.10}$$

Singularity Analysis

Investigating Eq. (e.8) in Appendix E, indicates that it is physically impossible for the haptic mechanism to have both vectors $(\overrightarrow{OE} \times \overrightarrow{C_1E})$ and $(\overrightarrow{OE} \times \overrightarrow{C_2E})$ become zero simultaneously. Therefore, singular configurations happen only when one of the vectors is zero. In these configurations, each pantograph is in a fully-stretched or folded-back position as shown in Figures 3-9a and 3-9b. The hand-controller, in these configurations, loses one DoF. Additionally, the determinant of the right-hand side of Eq. (e.7) in Appendix E, is zero when both pantographs rotate as much as 90°. Four more singular configurations as shown in Figures 3-9c to 3-9f can happen. In these configurations, the mechanism gains one additional DoF, i.e., the hand-grip can move even though all actuators are locked.

Finally, with respect to the third and fourth DoFs, since they follow the spherical motion generated by the first two DoFs idly, singular configurations only occur when the deflection angles of the universal joints becomes 90° (see Figures 3-9a to 3-9f)

The above analysis shows that all singular configurations occur at the boundary of the great circle of the hemisphere which is physically unreachable by the hand-grip. Therefore, the proposed design creates a singularity-free workspace.

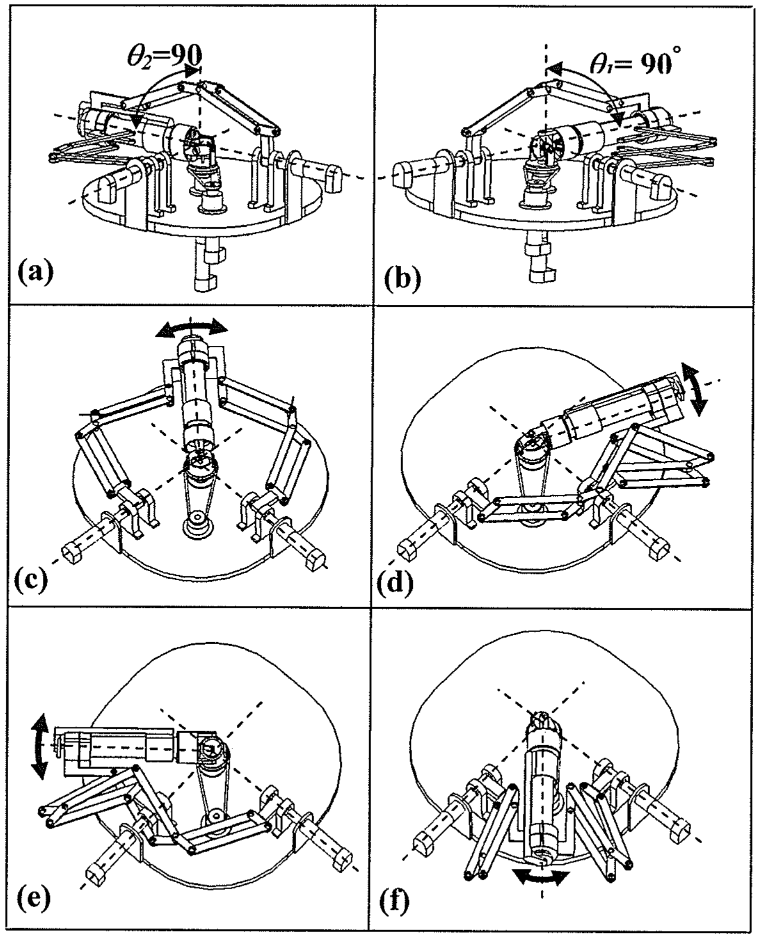

Figure 3-9. Singular configurations of hand-controller with simplified structure. In configurations (a) and (b) hand-controller loses one DoF. In configurations (c), (d), (e) and (f) hand-controller gains an extra DoF.

3.5 Output Force Analysis

3.5.1 Maximum and Uniformity of Output Force

Providing force reflection along the axis of hand-grip assists physicians to properly maintain the pressure between the remote probe and the patient's body in ultrasound examinations. This Section describes the maximum magnitude and uniformity of static forces that the hand-controller is able to apply against the user's hand along the axis of its grip. With reference to Figure 3-10, motor torque and position, T_3^m and θ_3^m, are converted to torque and position, T_3^r and θ_3^r, by the cable reducer. Torque and position, T_3^r and θ_3^r, at the output of cable reducer are converted next to, T_3^u and θ_3^u, by the universal joint. Finally, T_3^u and θ_3^u are converted to output force and displacement, F_3 and r, of the hand-grip via the cable drive. The following relationship exists between the input and output rotational angles of the universal joint (Johnson and Willems 1993; Sclater and Chironis 2001):

$$\tan\theta_3^u = \cos\psi \tan\theta_3^r \tag{3.11}$$

where ψ (hand-grip orientation) is the angle between hand-grip and vertical axis.

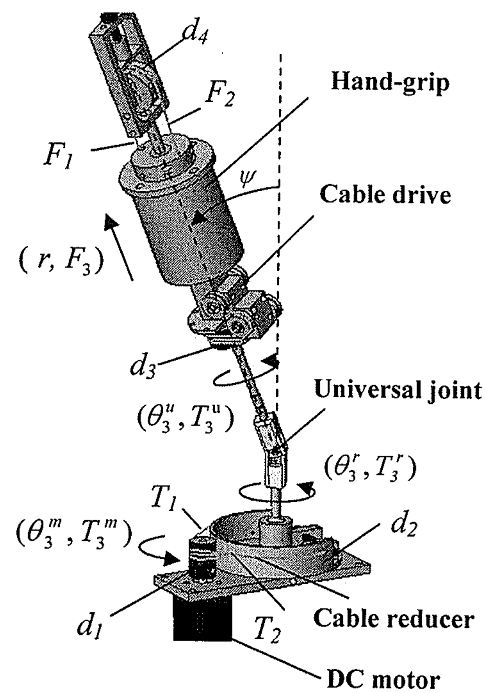

Figure 3-10. Power train of third DoF showing torques and angular positions.

In static equilibrium, the relation between input and output torques of the universal joint, T_3^r and T_3^u is:

$$T_3^u = \frac{\cos^2\theta_3^r}{\cos\psi\cos^2\theta_3^u} T_3^r \tag{3.12}$$

Combining Eqs. (3.11) and (3.12),

$$T_3^u = \frac{\cos\psi}{\sin^2\theta_3^u + \cos^2\psi\cos^2\theta_3^u} T_3^r \tag{3.13}$$

With reference to Figure 3-10, we have $T_3^r = nT_3^m$, $T_3^u = F_3 d_3 / 2$, and $r = d_3\theta_3^u / 2$ where n, d_3 and r are cable reduction ratio, diameter of driver pulley at the cable drive, and radial displacement of the haptic-grip, respectively. Therefore, the applied force, F_3, on the user's hand along the axis of the hand-grip is:

$$\frac{F_3}{T_3^m} = \frac{2n\cos\psi}{d_3[\sin^2(\frac{2r}{d_3}) + \cos^2\psi\cos^2(\frac{2r}{d_3})]} \tag{3.14}$$

Equation (3.14) describes the analytical relation between motor torque, T_3^m, and the output force, F_3, as a function of hand-grip displacement, r, and orientation, ψ. Using Eq. (3.14), variation of the output force F_3 is simulated and shown in Figure 3-11 for $T_3^m = 1$ Nmm, $d_3 = 22$ mm, $-60^\circ \le \psi \le 60^\circ$, $-15 \le r \le 15$ mm, and $n = 5$. The dashed-rectangle shows the workspace of the device presented in this thesis. From Figure 3-11, the lower bound of the output force is 0.45 N/Nmm. The maximum continuous and stall torque of the selected actuator (RE25 Maxon motor) are 29.3 Nmm and 129 Nmm, respectively. Thus, the lower bounds of the output force, F_3, using maximum continuous and stall torque of the actuator, are 13.2 N and 58.1 N, respectively which are enough for ultrasound imaging applications (Guerin et al. 2003). Moreover, the variation of the maximum output force in the workspace of the device is less than 10% which is desirable.

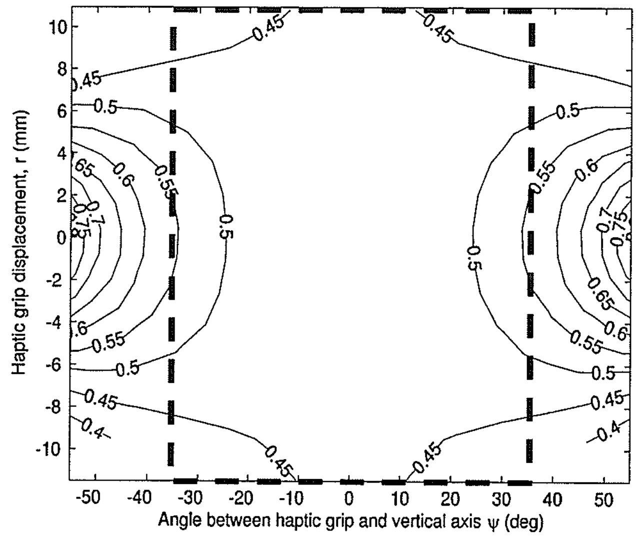

Figure 3-11. Iso-value output force per unit motor torque (N/Nmm) on user's hand for $T_3^m = 1\,\text{Nmm}$, $d_3 = 11\,\text{mm}$, $-60^\circ \le \psi \le 60^\circ$, $-15 \le r \le 15$ mm, and $n = 5$.

3.5.2 Output-Force Error

Once a force is exerted to user's hand, elastic members of the hand-controller deflect. In the present hand-controller, the power train of the sliding motion of the hand-grip consists of a DC motor, cable reducer, universal joint, and cable drive (see Figure 3-10). The deflection of the cable reducer and cable drive, combined with the motion of the universal joint affect the accuracy of the output force on the haptic-grip. The deviation between the intended force and the actual output force applied to the user's hand, $|\Delta F|$, is called force error. The relative output force error is then defined as the ratio of force error, $|\Delta F|$, over the acting force, $|F|$, that can be exerted (Mason and Salisbury 1985). In this Section, we derive the analytical expression of the relative output force error for the present hand-controller.

With reference to Figure 3-10, deformation of the cable at the cable reducer leads to a position error, $\Delta\theta_3^r$ (Townsend and Salisbury 1988):

$$\Delta\theta_3^r = \int_{\theta_3^m} \frac{T_1 - T_2}{EA} \frac{d_1}{d_2} d\theta_3^m \qquad 0 \le \theta_3^m \le \frac{5\pi}{2} \tag{3.15}$$

where T_1 and T_2 are the high and low tension sides, respectively. E and A are module of elasticity and cross sectional area of the cable, respectively. In the cable reducer, the driver pulley is threaded which engages the cable in a way to form a friction drive. Two or three warps is sufficient to prevent the cable from slipping on the pulley since the ratio of the high to low tension sides of the cable increases exponentially with wrap angle. Thus, with reference to Figure 3-10 for the cable reducer, we have

$$\frac{T_1}{T_2} = e^{\mu \gamma_r} \tag{3.16}$$

μ and γ_r are the coefficient of friction in cable-pulley assembly and wrap angle for cable reducer, respectively.

Position error of the cable reducer, $\Delta\theta_3^r$, results in a position error, $\Delta\theta_3^u$, at the output of the universal joint which can be found using Taylor series and Eqs. (3.11) and (3.15):

$$\Delta\theta_3^u = \Delta\theta_3^r \frac{d}{d\theta_3^r}[\tan^{-1}(\cos\psi \tan\theta_3^r)] = \Delta\theta_3^r \frac{\cos\psi(1+\tan^2\theta_3^r)}{(1+\cos^2\psi\tan^2\theta_3^r)} \tag{3.17}$$

Similarly, position error due to the deflection at the cable drive, $\Delta\theta_3^f$, can be obtained as:

$$\Delta\theta_3^f = \int_{\theta_3^u} \frac{F_1 - F_2}{EA}\frac{d_3}{d_4} d\theta_3^u \qquad (0 \le \theta_3^u \le \frac{\pi}{2}) \tag{3.18}$$

where

$$\frac{F_1}{F_2} = e^{\mu \gamma_f} \tag{3.19}$$

The total position error can be obtained by adding Eqs. (3.17) and (3.18):

$$\Delta\theta_3^{total} = \Delta\theta_3^u + \Delta\theta_3^f$$

The output torque of the universal joint, T_3^u, has the following relation with the high and low tension sides of the cable drive (see Figure 3-10):

$$T_3^u = 0.5 d_3 (F_1 - F_2) \tag{3.20}$$

The relation between output torque of the universal joint, T_3^u, and the motor torque T_3^m can be found using Eq. (3.13):

$$T_3^u = \frac{n\cos\psi}{\sin^2\theta_3^u + \cos^2\psi\cos^2\theta_3^u} T_3^m \qquad (3.21)$$

Combining Eqs. (3.19), (3.20), and (3.21), we have:

$$F_1 = \frac{n\cos\psi}{0.5d_3(1-\frac{1}{e^{\mu\gamma_f}})(\sin^2\theta_3^u + \cos^2\psi\cos^2\theta_3^u)} T_3^m \qquad (3.22)$$

The total position error, $\Delta\theta_3^{total}$, creates an output force error, ΔF_1, which can be calculated using Taylor series and Eq. (3.22):

$$\Delta F_1 = \Delta\theta_3^{total}\frac{dF_1}{d\theta_3^u} = \Delta\theta_3^{total}\frac{4n\cos\psi\sin^2\psi\sin\theta_3^u\cos\theta_3^u}{d_3(1-\frac{1}{e^{\mu\gamma_f}})(\sin^2\theta_3^u + \cos^2\psi\cos^2\theta_3^u)^2} T_3^m \qquad (3.23)$$

Therefore, the relative force error, $\eta = \left|\frac{\Delta F_1}{F_1}\right|$, is determined using Eqs. (3.22) and (3.23) as follows:

$$\eta = \left|\frac{2\Delta\theta_3^{total}\sin^2\psi\tan(\frac{2r}{d_3})}{\tan^2(\frac{2r}{d_3}) + \cos^2\psi}\right| \qquad (3.24)$$

Equation (3.24) describes the relative force error, η, based on the total deformation of the cables, $\Delta\theta_3^{total}$, radial displacement of the hand-grip, r, orientation of the hand-grip, ψ, and diameter of drive pulley, d_3. Figure 3-12 shows the relative output force error of the hand-grip for $d_1 = 12$ mm, $d_2 = 60$ mm, $d_3 = d_4 = 22$ mm, $-60° \le \psi \le 60°$, $-15 \le r \le 15$ mm, $n = 5$, $E = 210$ GPa, $A = 1.6\times10^{-7}$ m^2, $\mu = 0.61$, $\gamma_f = \gamma_r = 6\pi$ rad, and $T_3^m = 129$ Nmm (Motor stall torque). This Figure shows that the relative force error of the haptic is % 0.8 which indicates a high-fidelity static force reflection considering the effect of cable deformation and universal joint of the power-train.

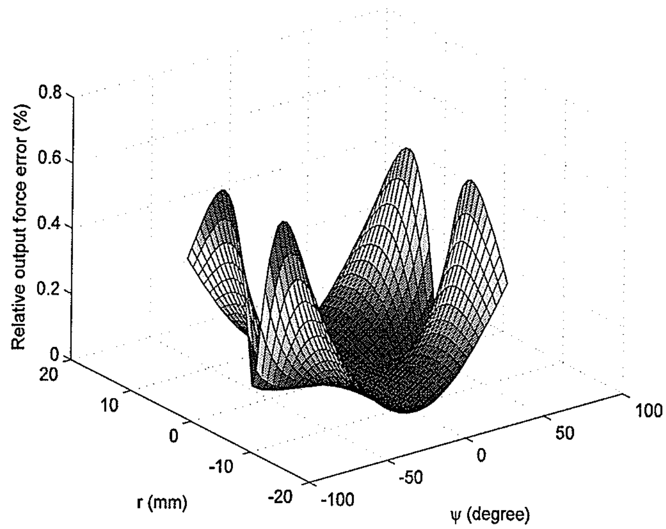

Figure 3-12. Relative output force error of hand-grip over entire workspace.

3.6 Prototype Device

System and Characteristics

Figure 3-13 shows the prototype hand-controller. The sliding motion of the hand-grip is driven by a Maxon permanent magnet DC motor (RE 26) and cable reducer (reduction ratio: 1/5) to provide force feedback to the operator's hand along the axis of the hand-grip. The continuous output torque of the DC actuator is 29.3 Nmm and the range of the sliding motion is 32 mm.

The workspace of the hand-controller is a cone with vertex angle as much as 70° which is adequate for performing ultrasound examination (Guerin et al. 2003). The workspace of the hand-controller is singularity-free. The footprint and height of the device are (232 mm × 232 mm), and 280 mm, respectively. The inertia matrix of the prototype device has been calculated at its center of mass, using SolidWorks, and for the device in its upright position.

$$\begin{pmatrix} I_{xx} & -I_{xy} & -I_{xz} \\ -I_{yx} & I_{yy} & -I_{yz} \\ -I_{zx} & -I_{zy} & I_{zz} \end{pmatrix} = \begin{pmatrix} 2.633 & -0.003 & -0.016 \\ -0.003 & 2.637 & -15.0 \\ -0.016 & -0.010 & 0.908 \end{pmatrix} \times 10^{-3} \ (\text{kg.m}^2)$$

The haptic structure is made of ordinary aluminium except for the shafts which are made of steel. The weight of all the moving elements is 452 gr. The weight of the device is effectively balanced with a zero-free-length tension spring of stiffness 0.4×10^{-3} kg/mm when the hand-grip is in the middle of its stroke. The spring stiffness is chosen based on Eq. (3.1).

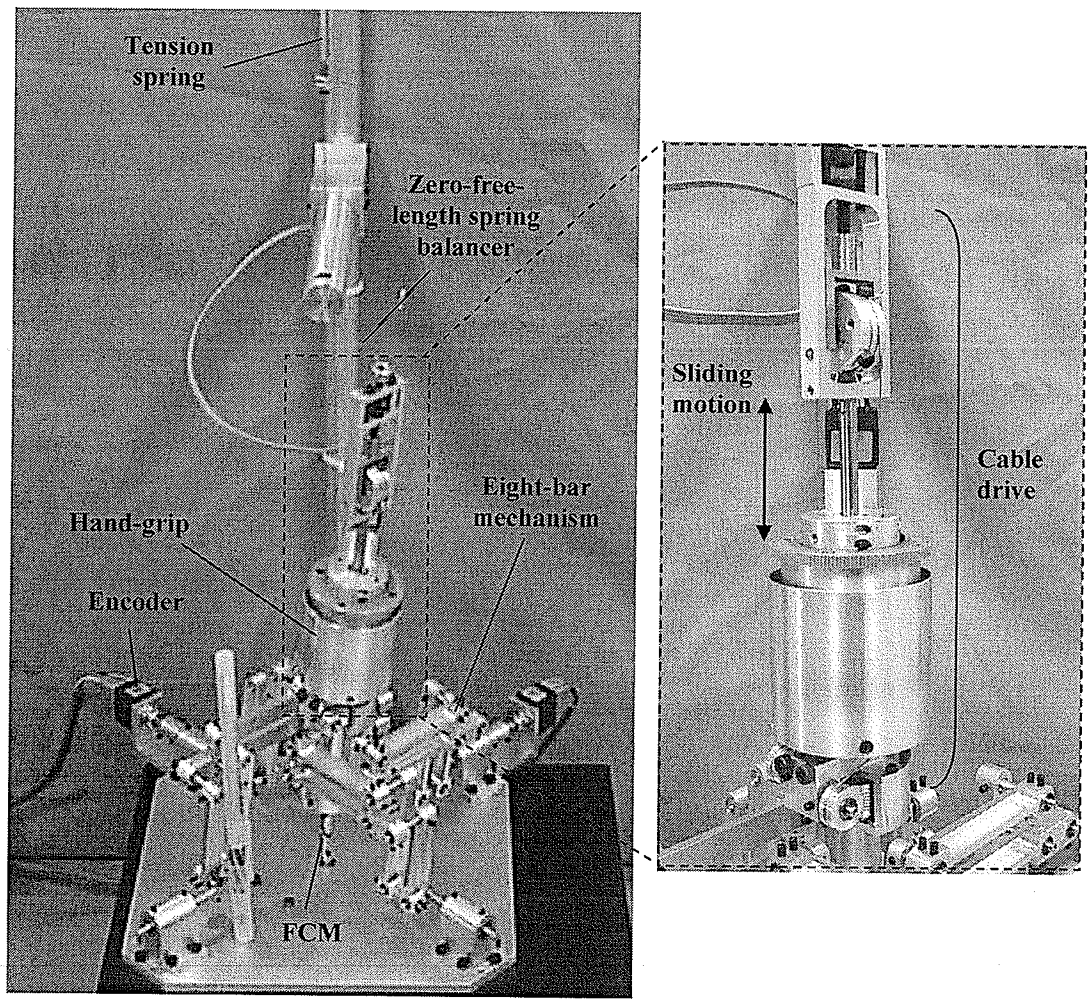

Figure 3-13. Prototype of hand-controller with force reflecting hand-grip and close-up view of cable drive.

Static Balancing Test

In order to test the performance for static balancing, the hand-grip was moved in various orientations by an operator for about 4.2 sec and before the operator lets go of the hand-grip (Figure 3-14). As is seen, the mechanism remained stationary which showed a satisfactory performance for static balancing. Similar results were repeatedly achieved throughout the entire workspace.

Relationship between Control Signal and Output Force

The relationship between the control signal and output force applied to the user's hand along the axis of the hand-grip was also obtained experimentally (Figure 3-15). A miniature force sensor (LCMKD 50 N, by Omega) was used within the hand-grip. Control signal was incrementally increased while output force was measured which showed a linear pattern. This result was used for output force calibration of the device during remote ultrasound imaging which involved force reflection to operator's hand.

Static-friction Break-away Force

The static-friction break-away force is defined as the minimum open-loop force increment when the change of the hand-grip position is the position resolution of the hand-grip (Yoon and Ryu 2001). This force was measured for the sliding motion of the hand-grip and is equal to 0.26 N (see Figure 3-16). This force was measured by incrementally increasing the weight-compensated hand-grip until it started to move. The measured static friction force for the present device is similar to the haptic device reported by Yoon and Ryu (2001).

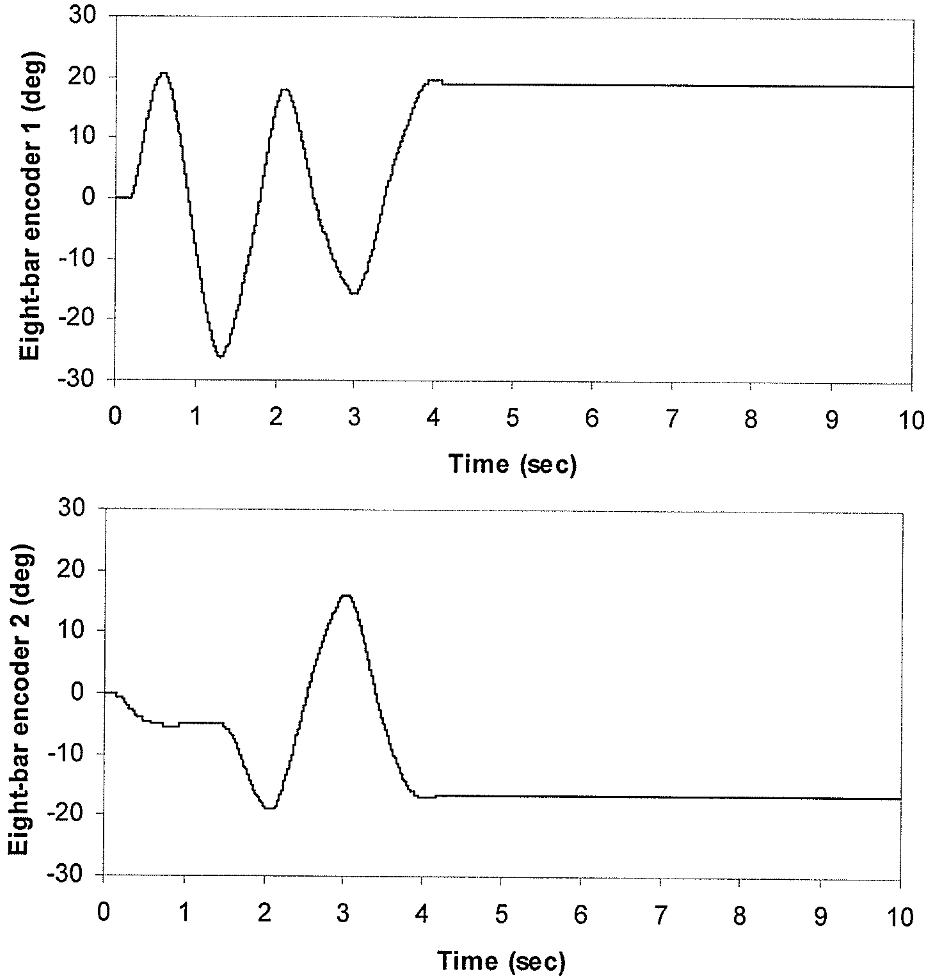

Figure 3-14. Demonstration of static balancing of prototype device. Device is moved arbitrarily and then released at about -18° and 20° orientation.

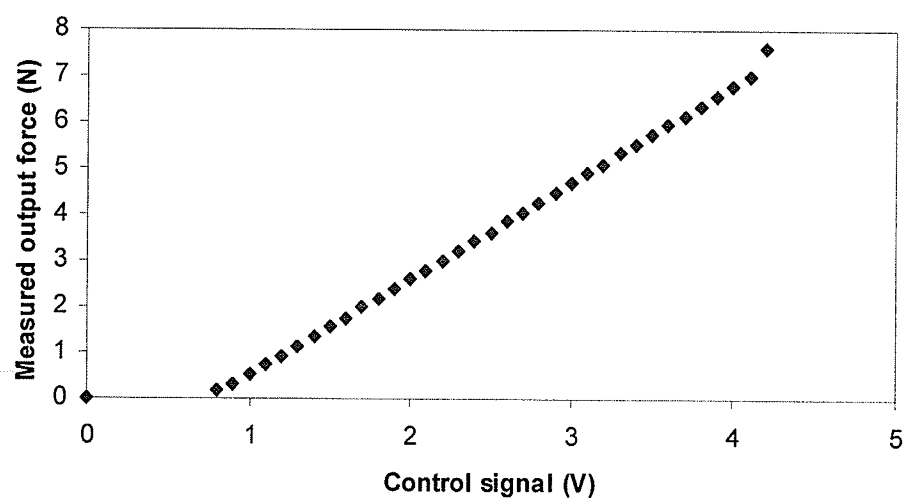

Figure 3-15. Experimental relation between control signal and measured output static force along the axis of hand-grip.

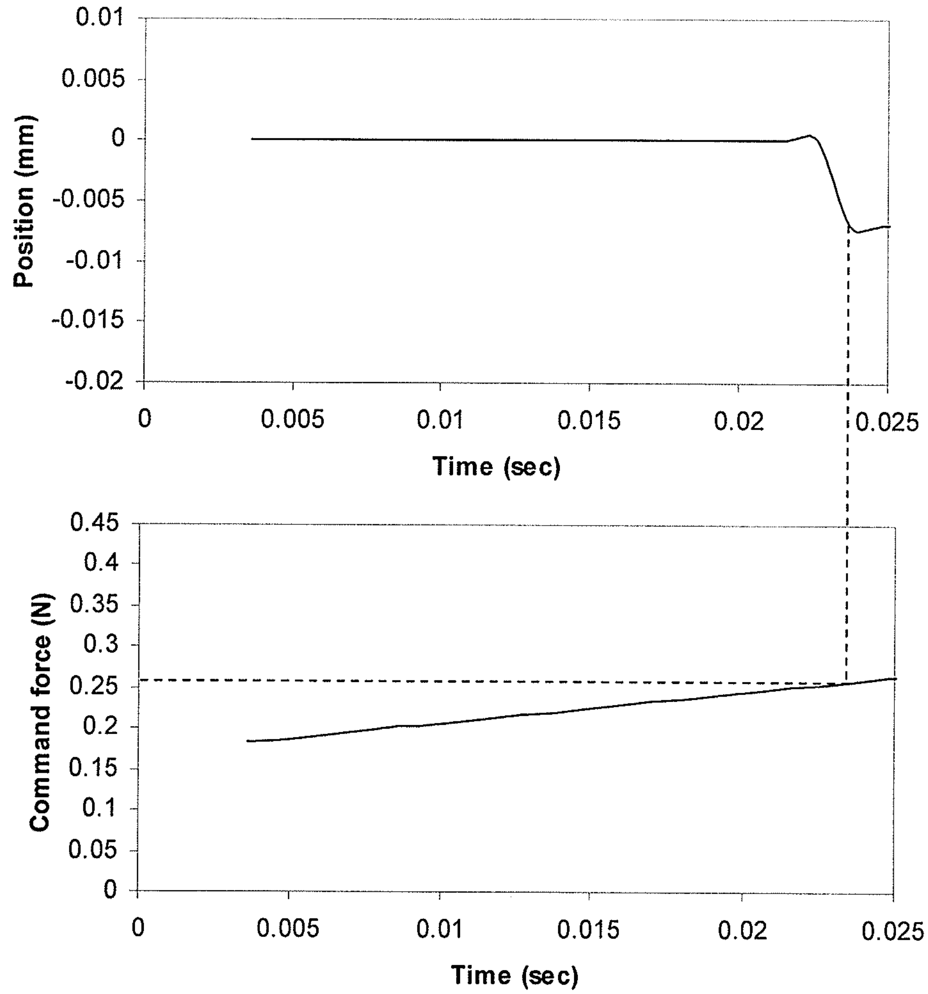

Figure 3-16. Static-friction break-away force along the axis of hand-grip.

3.7 Performance Evaluation

3.7.1 Evaluation of Entire Device

Virtual surface simulation was used to measure maximum achievable wall impedance while keeping the device stable. Stability is defined as a situation where sustained oscillations occur at the onset of contact. The virtual surface is modeled as a spring-damper system (Yoon and Ryu 2001):

$$F_{surface} = -\alpha[K(X_{hand} - X_{surface}) + \beta B\dot{X}_{hand}]$$

where α and β are constraints, K is the wall stiffness and B is the wall damping coefficient. The Constraints α and β are:

$$\alpha = \begin{cases} 1 & if \quad X_{hand} > X_{surface} \\ 0 & if \quad X_{hand} \leq X_{surface} \end{cases}$$

and

$$\beta = \begin{cases} 1 & if \quad \dot{X}_{hand} > 0 \\ 0 & if \quad \dot{X}_{hand} \leq 0 \end{cases}$$

The parameter α provides the force to the hand-grip only when the operator's hand penetrates inside the surface. The parameter β ensures that the damper does not provide any force on the hand-grip when it is moved away from the surface. In this experiment, the operator moved the hand-grip downward from zero position to contact and then to penetrate inside the surface. Stability was evaluated by recording the position (penetration depth) of the hand-grip. The maximum surface stiffness without inducing sustained oscillations was found to be 5 N/mm. The Figure 3-17a shows virtual surface simulation for the maximum surface stiffness. The maximum surface damping without stiffness was found to be 0.1 Ns/mm. Figure 3-17b shows virtual surface simulation for the maximum surface damping without stiffness. The maximum surface stiffness and damping without creating sustained oscillations at the boundary of the surface were found to be 5.6 N/mm and 0.06 Ns/mm, respectively (Figure 3-17c).

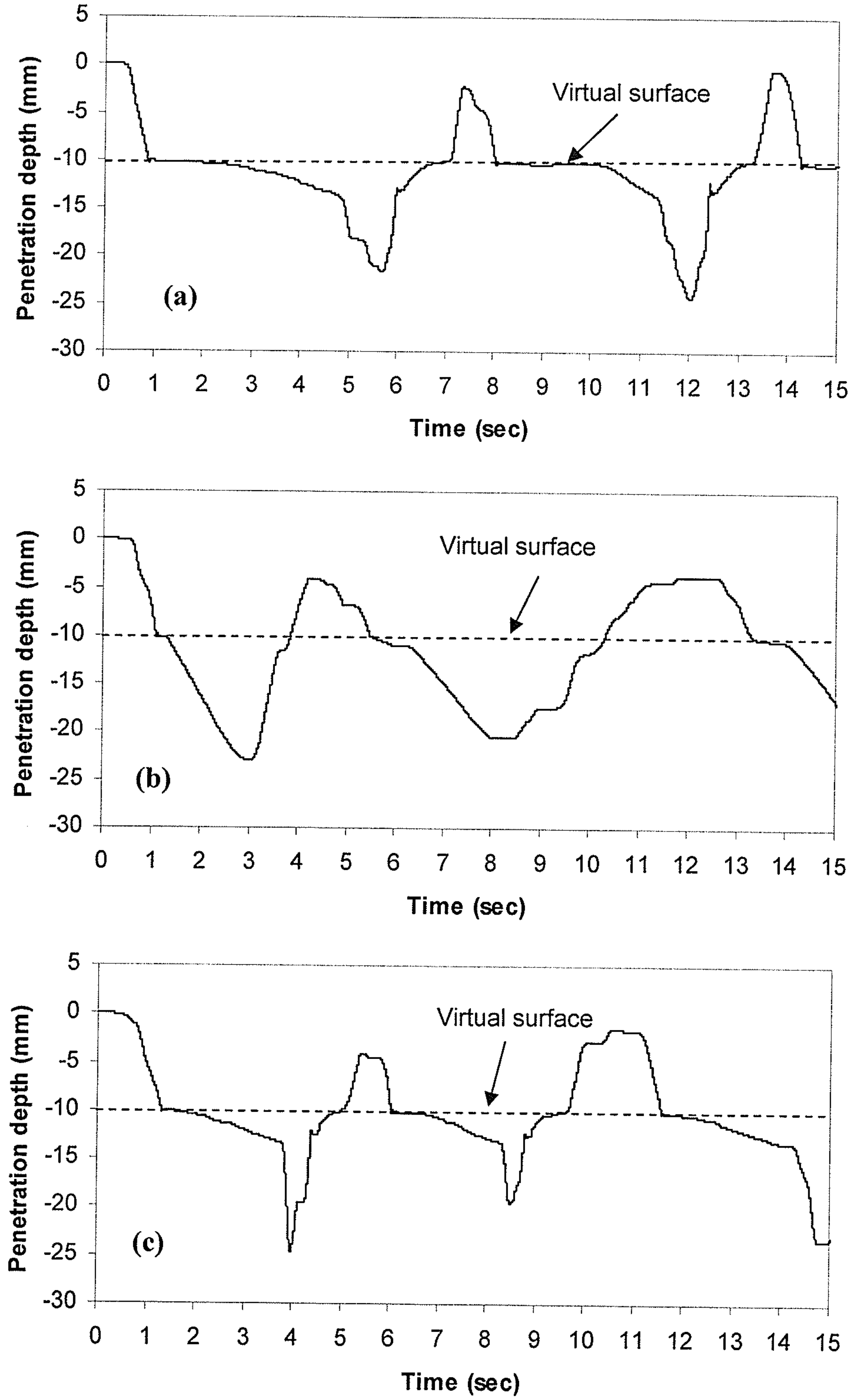

Figure 3-17. Virtual surface simulation without inducing sustained oscillations: (a) for maximum achievable surface stiffness of 5 N/mm and without damping; (b) for maximum achievable surface damping of 0.1 Ns/mm without stiffness; (c) for maximum achievable combined surface stiffness of 5.6 N/mm and damping of 0.06 Ns/mm.

3.7.2 Effect of Fixed Center-of-Motion

3.7.2.1 Introduction

In a conventional ultrasound examination, a physician moves an ultrasound probe in a circular motion about a fixed center-of-motion (FCM) on the patient's body. A considerable performance measure in this task is the operator's ability to minimize the error movements, i.e., unwanted movement of the probe in the plane other than the one containing desired scanning motion. Without minimizing the error movements during scanning, the operator would run the risk of not successfully capturing the intended ultrasound images. This problem can be amplified in any robotic-based ultrasound examination task.

The developed haptic device in this thesis has a physical fixed center-of-motion to facilitate 3-D imaging. As far as remote ultrasound imaging using a hand-controller is concerned, the benefit of having a fixed center-of-motion (FCM) on remote ultrasound task performance has not been investigated in the prior work (Vilchis et al. 2003; Koizumi et al. 2008; Delgorge et al. 2005; Marchal and Troccaz 2004).

In this Section, the effect of FCM on the user performance of the developed haptic device is studied. The results are compared with the performance of the general-purpose and widely-used OMNI PHANToM haptic device which does not have a physical FCM. A canonical task closely representing the main motion of the ultrasound task was chosen. The subjects were asked to perform the task with minimum hand-trajectory errors. Task completion time, root-mean-square of error of operator's hand-movements, and error band (peak-to-peak error), were chosen as performance indices.

3.7.2.2 Task Description

A canonical task which simulates the circular motion, ± 25°, of an ultrasound probe about a FCM on the patient's body, is shown in Figure 3-18. This experiment investigates if the haptic device developed in this thesis allows operators to execute this task without introducing unwanted gross orientation on the plane orthogonal to the plane of the desired motion.

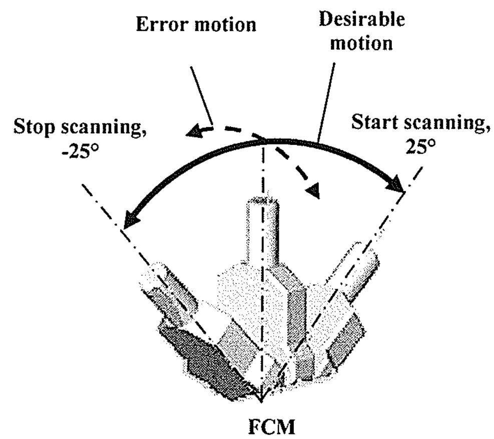

Figure 3-18. Pitch scanning motion of an ultrasound probe about a fixed center-of-motion.

User Interfaces

The first interface employed the developed haptic device. In this interface, the operators performed the pitch task about FCM in XZ plane and about Y axis (Figure 3-19a). The error angle was measured as unwanted angular motion about X axis. A constant 1 N force was applied to the user's hand along the axis of hand-grip in all orientations.

The second interface used a commercially available OMNI PHANToM[2] device (Figure 3-19b). In this interface, in order to assist the operator to perform pitch scanning task about Y axis, the gimbal center of the PHANToM device was confined in XY plane by creating a virtual fixture of cylinder type with wall stiffness of 0.3 N/mm and radius of 1 mm. A constant 1 N force, representing the contact force between probe and patient's body, was applied to the operator's hand only along the Z axis to allow the operator to hold the FCM in place. The error angle was measured as unwanted angular motion about X axis.

Two numbers were shown on computer monitor for both interfaces, the first number showed the pitch angle and the second number showed operator's hand-error.

[2] OMNI PHANToM is a six DoF haptic device with force reflection capability along XYZ axes. Technical specifications of the device are: (*i*) nominal position resolution of 0.055 mm; (*ii*) maximum output force 3.3 N at nominal position of the device.

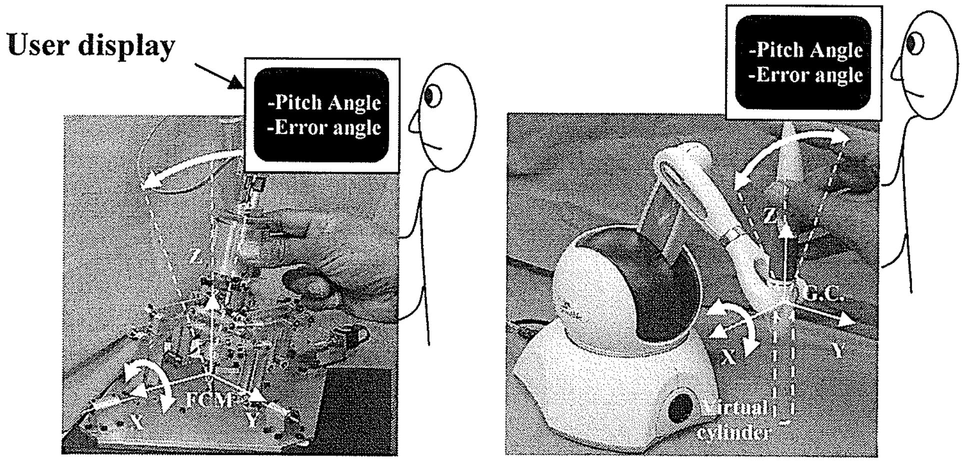

(a) (b)

Figure 3-19. Interfaces for pitch scanning task: (a) ultrasound haptic; (b) Phantom virtual cylinder.

Experimental Procedure

Ten subjects participated in this experiment. All of them had previous experience using standard joysticks. Each of the 10 subjects performed 10 trials for each interface. Prior to the trials, participants practiced until they felt comfortable with both interfaces. In order to initiate each experimental trial, the users had to locate the end-effector of the devices at the starting position of the circular path. The participants were then instructed to scan the path for ten times within 2 minutes and to maintain the error angle as small as possible. The task completion time was recorded for the movement of the end-effectors from the start position to the end position for each trial. During the task, time history of the measured error angle was recorded so that the root-mean-square[3] (RMS) of error as well as error band could be calculated for each trial. This set of experiments used a 2 (interface) $\times$ 1 (task) factorial design. The independent variables were interface types. For each experimental condition, the users performed 10 trials. This gave a total of 10

---

[3] The root-mean-square of collection of n values $\{x_1, x_2, ..., x_n\}$ is defined as $x_{RMS} = \sqrt{\frac{1}{n}\sum_{i=1}^{n} x_i^2}$. In mathematics the root mean square also known as quadratic mean, is a statistical measure of the magnitude of a varying quantity. It is especially useful when variables are positive and negative. The result is a measure of the magnitude of a set of numbers. In other methods such as average and mean, the positive and negative numbers cancel each other.

(subjects) $\times$ 2 (interfaces) $\times 10$ (trials) = 200 trials. The design was fully counterbalanced on interface type.

Results

Figure 3-20 shows typical hand and error trajectories for pitch scanning task using the above mentioned interfaces. Error trajectories decrease from PHANToM to ultrasound haptic device (Figures 3-20b and 3-20c). The results of the statistical analysis are presented below. Figure 3-21 shows the mean completion times for both interfaces. The results of the univariate analysis[4] show that there is no significant difference between interfaces (p=0.074). However, it took longer for the subjects to perform each trail for the ultrasound haptic device as compared with the PHANToM, probably, due to higher inertia of the ultrasound haptic.

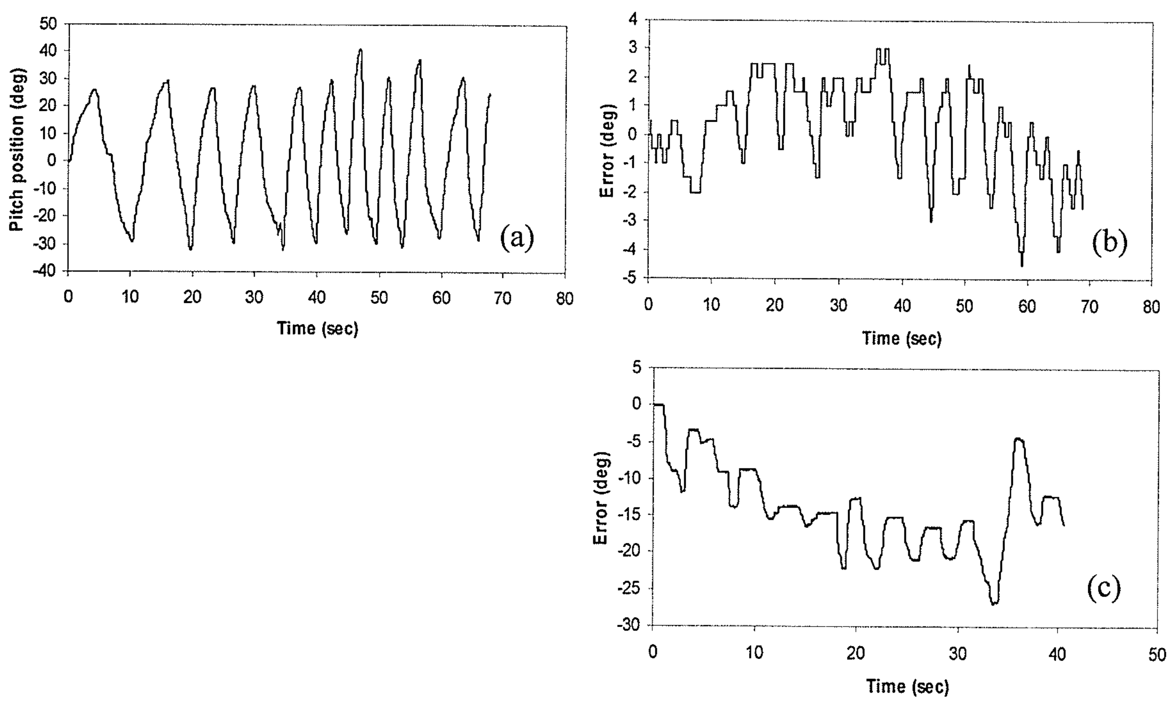

Figure 3-20. (a) typical hand-trajectory during pitch task for a randomly selected subject; (b) typical error trajectory for ultrasound haptic interface; (c) typical error trajectory for Phantom virtual cylinder interface.

[4] Univariate analysis explores each variable in a data set, separately. It looks at the range as well as the central tendency of the values. The value of P shows that if there is a significant difference between interfaces. In particular, $P < 0.05$ indicates that the smallest and largest means of interfaces are significantly different from each other.

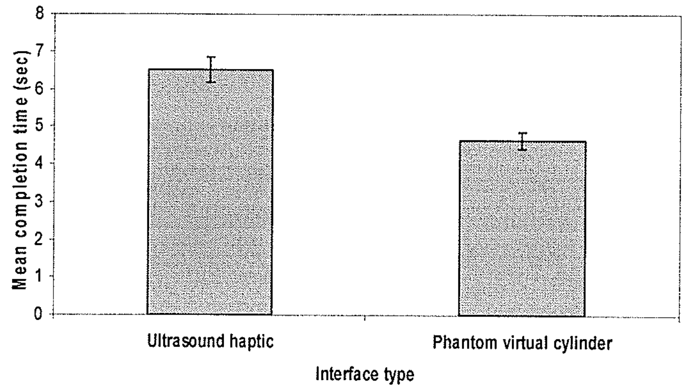

Figure 3-21. Mean task completion times.

Figure 3-22 shows RMS of errors for each interface. A univariate analysis was used for comparing the RMS of errors. The results show that there is no significant difference between interfaces ($p=0.183$). However, the performance of the PHANToM device is still lower than the ultrasound haptic. According to subjects, they were more comfortable with the stiff FCM created by hardware as compared with the FCM created by software.

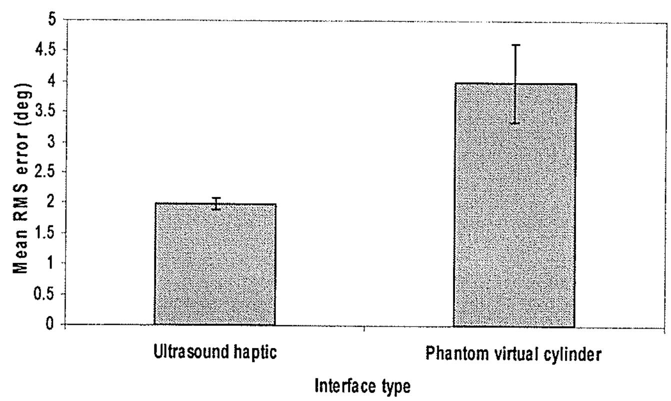

Figure 3-22. Mean RMS errors.

The error band for each interface is also shown in Figure 3-23. The results of a univariate analysis show that there is no significant difference between interfaces ($p=0.056$).

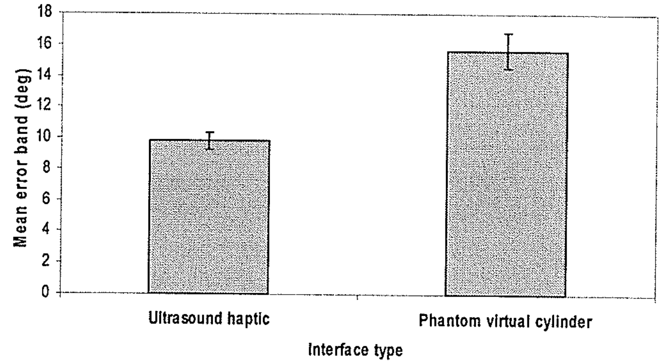

Figure 3-23. Mean error band (peak-to-peak error).

Discussion

From the above results, there was no significant difference in task completion time, RMS of errors, or error bands for interfaces in this experiment. The device proposed in this thesis has a FCM created by hardware. The PHANToM device was programmed to provide a FCM and to allow the user to move the stylus in a spherical coordinate system. The performance of the PHANToM device, in terms of RMS of errors and error band, was still lower than that of the ultrasound haptic interface. According to participant comments, the ultrasound haptic that uses physical FCM gave more support to hand motions during pitch scanning task. This result is inline with Vilchis et al. (2003) who physically fixed the center of PHANToM's gimbal mechanism when used for remote ultrasound examination. Moreover, the FCM created by mechanical hardware keeps the device in its workspace in case of power or software failure while in haptic mechanisms with FCM created by software, the mechanism collapse and move out of its intended workspace. In this case, the remote robotic arm will follow the haptic motions and generate unwanted motions on patient's body.

3.8 Summary

A novel 4-DoF force reflecting hand-controller for remote ultrasound imaging has been designed and constructed. The proposed force reflecting hand-controller is built upon parallel mechanisms with base-mounted actuators, has 4 degrees of freedom to provide standard clinical motions of ultrasound imaging, and has a fixed center-of-motion (FCM) located inside the mechanism. The existence of FCM in the kinematic chain enables operators to perform ultrasound examination with only 4 DoFs leading to reduction of the inertia of the moving parts. User performance evaluation shows that operators are more comfortable with the FCM created by hardware as compared with the FCM created by software. The proposed hand-controller in this thesis, exhibits a one-to-one-mapping between its movements and the movements of the ultrasound probe at the remote site. Moreover, all DoFs are kinematically decoupled from each other, i.e., independent drive system with base-mounted actuator for each degree of freedom. Finally, the workspace produced by the proposed hand-controller is singularity-free. The proposed device consists of miniaturized mechanisms with reduced inertia and intrusion with operator's hand. A novel balancing technique has also been used to statically balance the weight of the device by only a tension spring. The above mentioned features (parallel mechanism with base-mounted actuators, existence of physical FCM, decoupled kinematic, and static balancing) have not been simultaneously observed in the other haptic devices prior to this work.

Chapter 4

Experimental Setup of the Entire Robotic System

This Chapter describes the entire robotic system for remote ultrasound imaging. In particular, hardware setup, computer interfacing, and control implementation of the robotic system are presented. Experimental setup used for technical as well as ultrasound imaging evaluation of the system is presented.

4.1 Overview of the System

Figure 4-1 shows the entire robotic system developed in this thesis. The patient side consists of an ultrasound machine, a 4-DoF robotic wrist holding an ultrasound probe, a 3-DoF Scara robot (built by Quanser) for holding the robotic wrist, and video cameras. The physician side consists of a 4-DoF force reflecting hand-controller, a 2-axis spring-loaded joystick, and video displays. The two sides are connected together by Internet.

Using this setup, the physician is able to remotely relocate the ultrasound probe on the patient's body. This is done using the 2-axis joystick to control XY position of the Scara robot and consequently ultrasound probe. Joystick's push buttons enable the physician to lock the XY position of the entire wrist at the specific area of the patient's body. The physician then places the probe on the patient's body by moving the slider of the haptic device and consequently the robotic wrist along the axis of the ultrasound probe. The physician also feels the contact force between the probe and the patient's body. A force sensor is placed between the ultrasound probe and the wrist's end-effector to directly measure the interaction forces between the probe and the patient's body. Upon achieving contact between the probe and the patient's body, the physician is able to change the orientation of the probe by moving the remaining DoFs of the haptic device in order to capture the desired images of the affected organ.

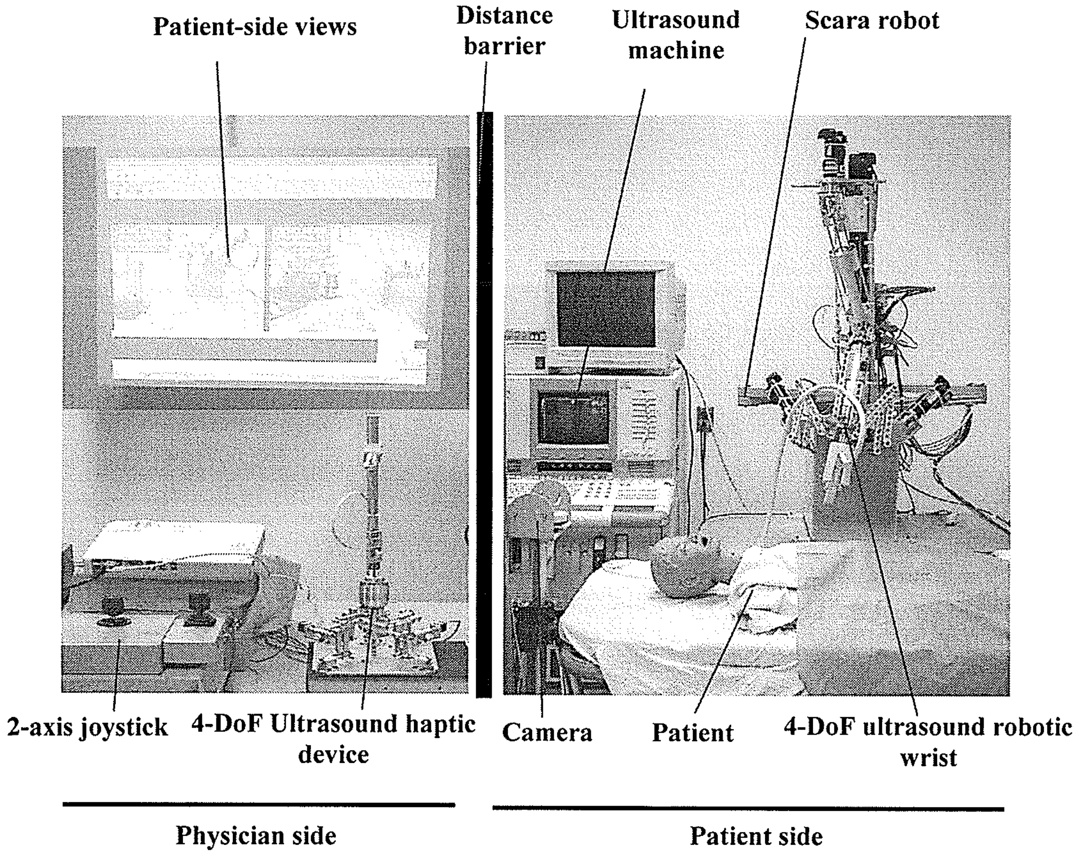

Figure 4-1. Proposed robotic system for remote ultrasound imaging.

There is a one-to-one position mapping (control-action correspondence) between corresponding DoFs in the hand-controller and robotic wrist and standard scanning schemes for ultrasound imaging (see Figure 4-2). This means, any control action by the physician and its resulting change in the remote wrist mechanism move equally and in the same direction. Therefore, the probe orientation in the wrist mechanism is always aligned with the orientation of the physician's hand. This makes the usage of the system intuitive and it is believed to reduce physician's mental load.

The physician uses camera views of the patient side when she/he is coordinating the Scara robot and wrist motions. 3-D cameras could be deployed which provides better 3-D perception for the physician. During ultrasound examination, the physician concentrates on the ultrasound images and haptic feedbacks coming from the patient's side.

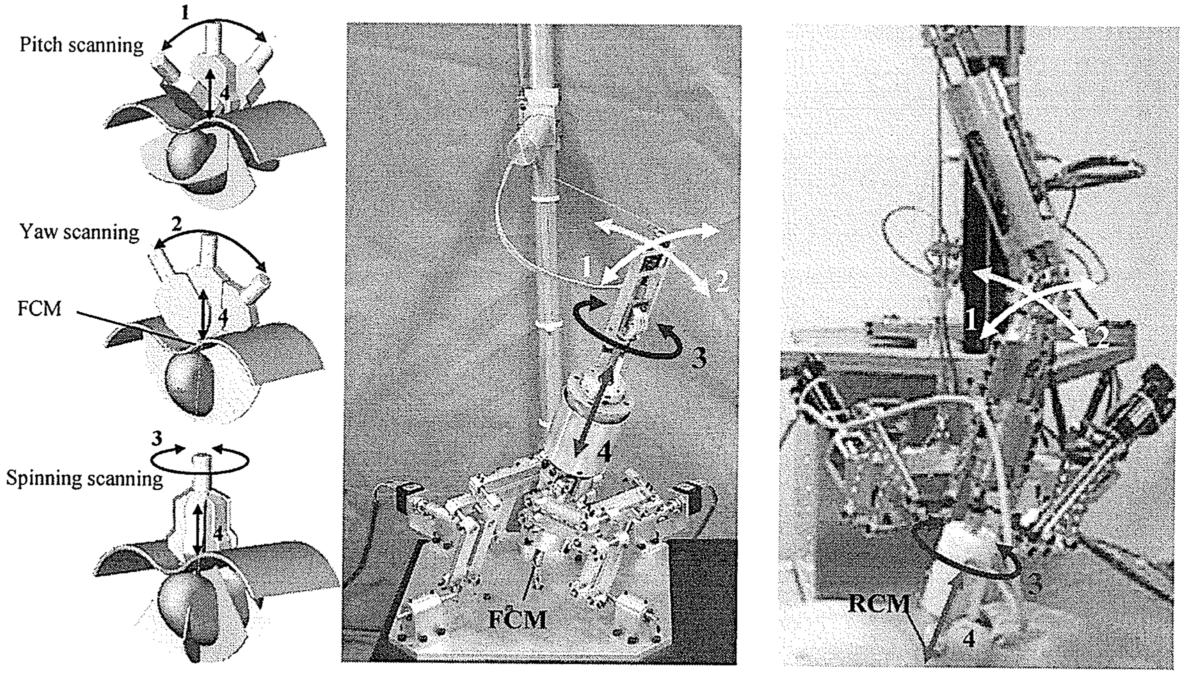

Figure 4-2. Motion correspondence between standard ultrasound motions, 4-DoF hand-controller, and robotic wrist.

4.2 Computer Interfacing

Figure 4-3 shows computer interfacing of the robotic system. Patient and physician sides are connected to each other through Internet. As network communication protocol, UDP (User Datagram Protocol) is implemented using C++ socket programming. Using campus network, the measured network round-trip delays between two sides is less than 1 ms.

Devices at both the physician and patient sides use similar control hardware as shown in Figure 4-3. They use Pentium 4 with 2.6 GHz CPU. Robotic wrist, 3-DoF Scara robot, hand-controller, and joysticks are connected to their computers via Q8 data acquisition boards[1], by Quanser, and LSC servo amplifiers by Maxon motor. The Q8 boards support

[1] The general specifications of the board are: (*i*) PCI interface; (*ii*) PCI bus width 32-bit; (*iii*) bus speed 33 MHz. The key features of the device are: (*i*) 8 × 14-bit (for 0-100% to the A/D converter the resolution is 0.006 %) programmable analog inputs (± 10 V) with 56 kHz sampling frequency; (*ii*) 8 × 12-bit (resolution 0.025%) D/A analog voltage outputs (± 10 V); (*iii*) 8 × 32-bit (resolution 0.001%) encoder counter. The board provides a high accuracy resolution for the application studied in this thesis.

all input/output applications. Each servo amplifier is a linear servo controller to control the current of each permanent magnet DC actuator.

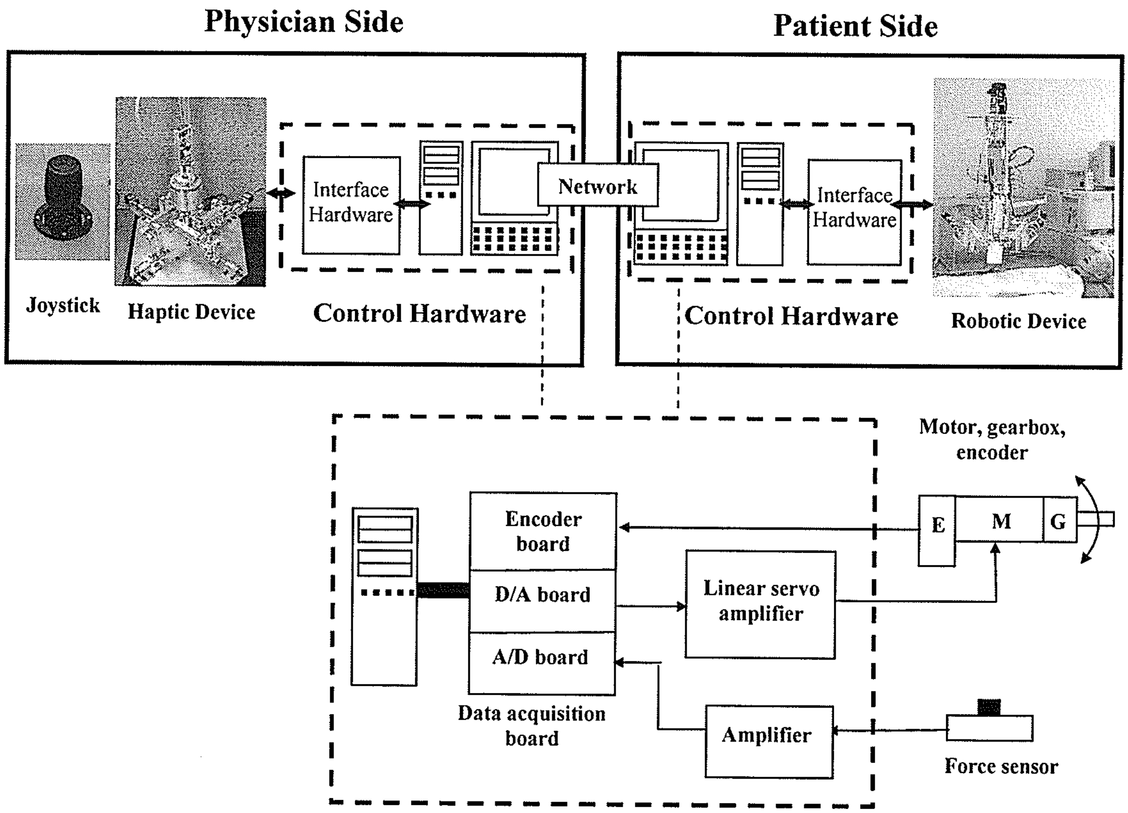

Figure 4-3. Schematic of computer interfacing.

In the proposed system, the physician is able to move and position an ultrasound probe on the entire body of the patient. Position control is preferable in applications calling for precise coordination of end-effector's movement. This method allows the physician to move the ultrasound probe as much as 25 mm for the maximum deviation of the joystick from its neutral position. Therefore, this method does not allow the physician to generate coarse motions over the patient's body. However, the physician is able to move the ultrasound probe over a long range of distance by multiple movements of the joystick.

A system capable of controlling the position of the robotic arm in remote side and at the same time reflecting forces to operator's hand by a haptic device is known as bilateral servo system (Kulishov and Lakota 1988). It is believed that this type of control architecture enhances task performance in remote ultrasound examinations. A bilateral servo system as shown in Figure 4-4 is implemented in the proposed robotic system between corresponding DoFs in the haptic device and the robotic wrist. The input for the subsystem that controls the position of the robotic wrist is haptic device position. This subsystem has the property of position servoing. Proportional plus derivative (PD) controllers have been implemented on the 4-DoF robotic wrist to track physician's hand movements. The input for the force servo subsystem (haptic side) is the measured force at the endpoint of the probe attached to the remote robotic wrist.

Force feedback to the physician's hand assists the physician to both maintain the probe contact and to adjust the applied pressure between the probe and the patient's body. Open-loop force feedback to physician hand is implemented in this subsystem. The shaft of any degree of freedom in the haptic and, in consequence, the respective shaft in the remote robotic wrist will remain stationary only if the slave contact force is equal to the reflected force to user. The user perceives at her/his haptic device the slave contact force scaled as much as n (see Figure 4-4). In the present system, n=1. The sampling frequency of control loop[2] is 1 kHz which is thirty times greater than the maximum frequency of the human wrist's motions.

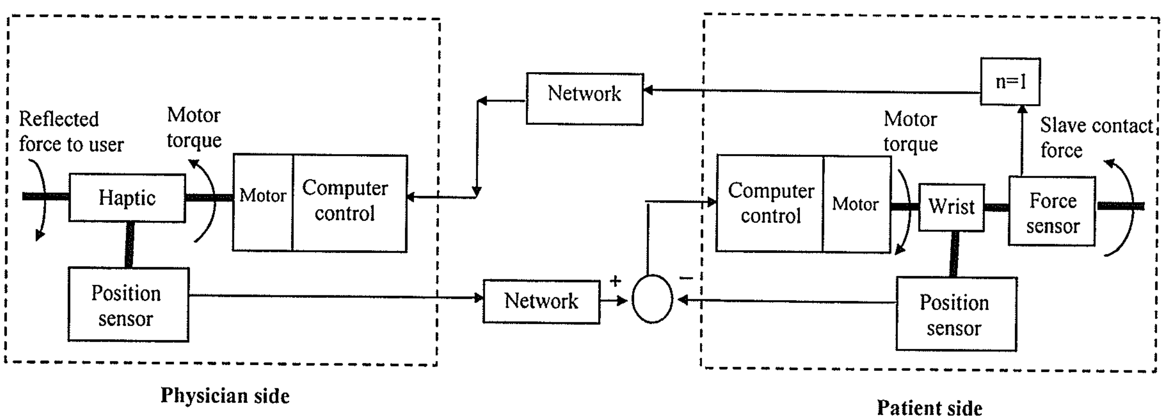

Figure 4-4. Block diagram of bilateral servo system used for position control of wrist and force control of haptic device.

[2] Nyquist rate suggests that sampling frequency of a signal should be at least two times greater the maximum frequency involved in the signal (Proakis and Manolakis 2007).

When the communication systems with constant or random round-trip delays used, several challenges and difficulties arise. Private fiber optic communication systems and Internet have constant and random round-trip delays, respectively. Most importantly, communication delays cause instability, loss of transparency, operator performance degradation, and desynchronization in real-time closed-loop bilateral tele-robotic systems (Anderson and Spong 1989; Niemeyer and Slotine 1998; Park and Kenyon 1999; Xi and Tarn 2000). However, these problems have not been addressed for the robotic system developed in this thesis. Dynamic modeling of the robotic wrist and haptic device considering nonlinearities such as backlash and friction is necessary for developing a practical control system in which instability and transparency of the robotic system are addressed (Lee and Spong 2006).

4.3 Ultrasound Imaging Tests

Experiments were performed with the robotic system on volunteers to show its capability to perform ultrasound examinations. An ultrasound technologist from Winnipeg Children Hospital used the robotic system to capture ultrasound images from volunteer's heart, kidney, liver and spleen. Images include long and short axes views of those organs (see Figures 4-5 and 4-6). The mechanical features of the entire robotic system were matched to what an ultrasound expert needed for ultrasound examination. Therefore, there was a very short training time of 2 to 5 minutes for the technologist to become familiar with the system. He was able to locate the ultrasound probe over the area of interest on the patient's body, and change the orientation of the probe to capture desired ultrasound images. Haptic feedback to his hand enabled him to maintain the contact between the ultrasound probe and the patient's body and obtain continuous ultrasound images. Moreover, haptic feedback was helpful for adjusting the amount of pressure between the probe and the patient's body. He was able to successfully capture the desired ultrasound images of the kidney, spleen and liver, and heart.

Figures 4-7 to 4-10 show position tracking responses of the robotic wrist during kidney examination by the ultrasound technologist. The steady-state position error of the robotic wrist appeared to be of limited importance for medical experts since they control the probe motion as a function of what they observe in the ultrasound image rather than a function of the position of the real probe relative to the body surface (Vilchis et al. 2003). Figure 4-11 shows open-loop force-tracking of the haptic device while the robotic wrist was moving an ultrasound probe on a volunteer during typical kidney examination.

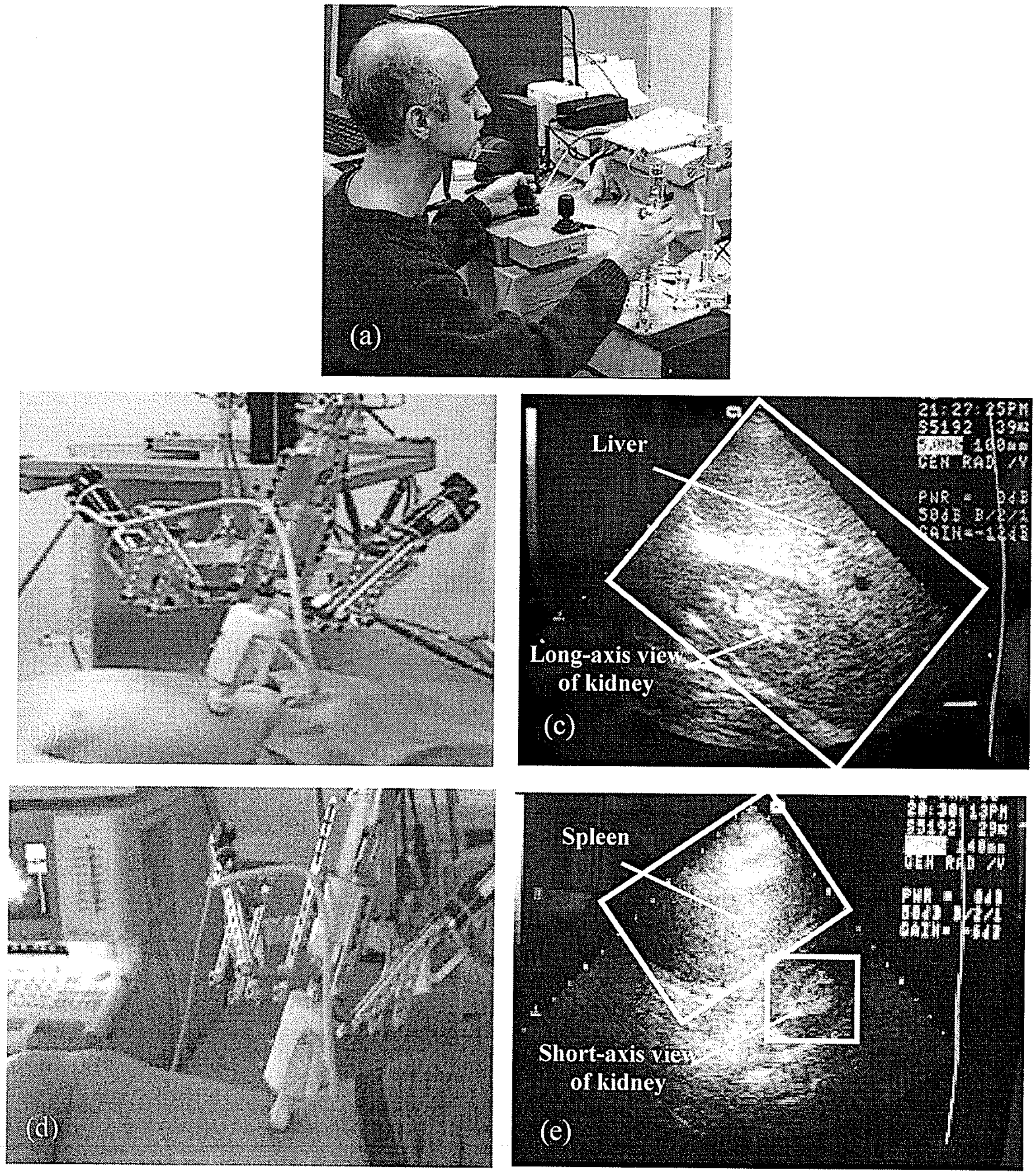

Figure 4-5. Remote ultrasound examination of kidney, spleen, and liver: (a) ultrasound technologist manipulating the hand-controller to capture ultrasound images; (b) 4-DoF wrist; (c) ultrasound image of kidney and liver; (d) 4-DoF wrist moving a volunteer; (e) ultrasound image of spleen and short axis view of kidney.

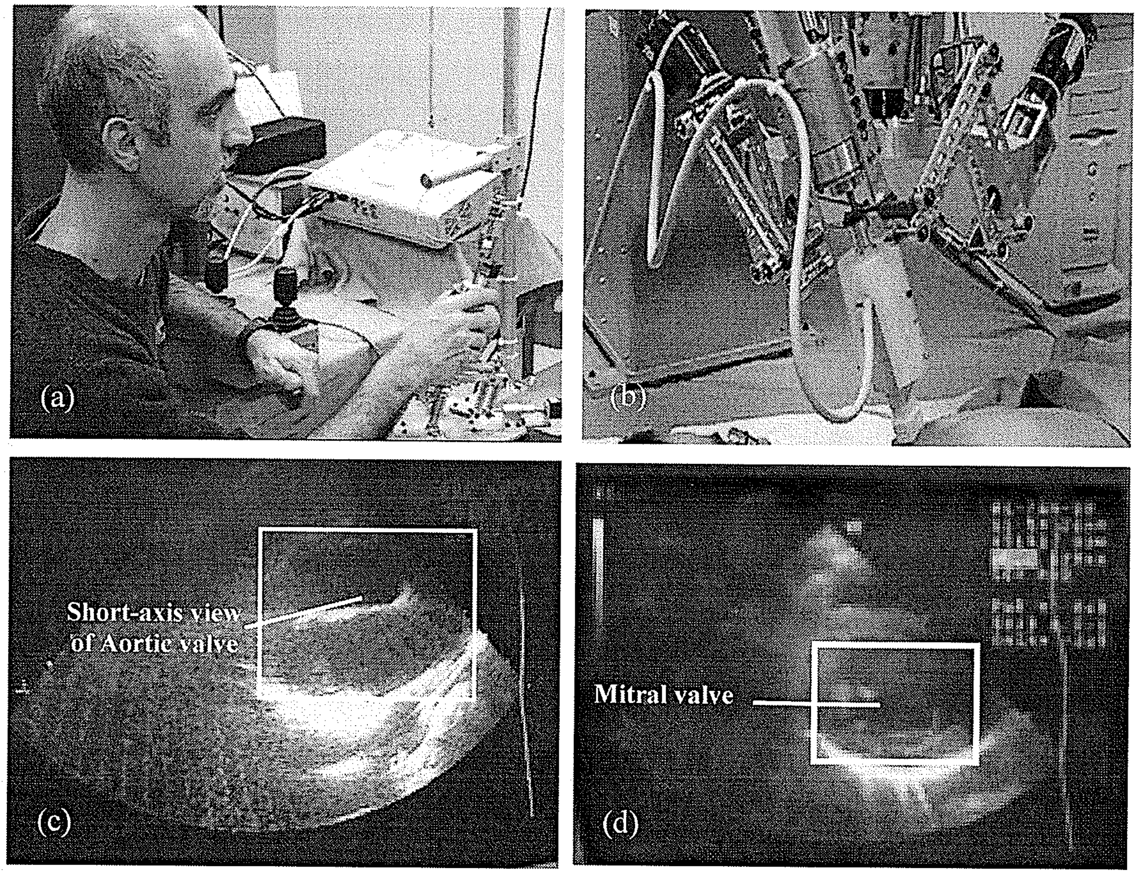

Figure 4-6. Remote ultrasound examination of heart: (a) ultrasound technologist manipulating the hand-controller to capture ultrasound images; (b) 4-DoF wrist moving on a volunteer; (c) short-axis image of Aortic valve; (d) image of Mitral valve.

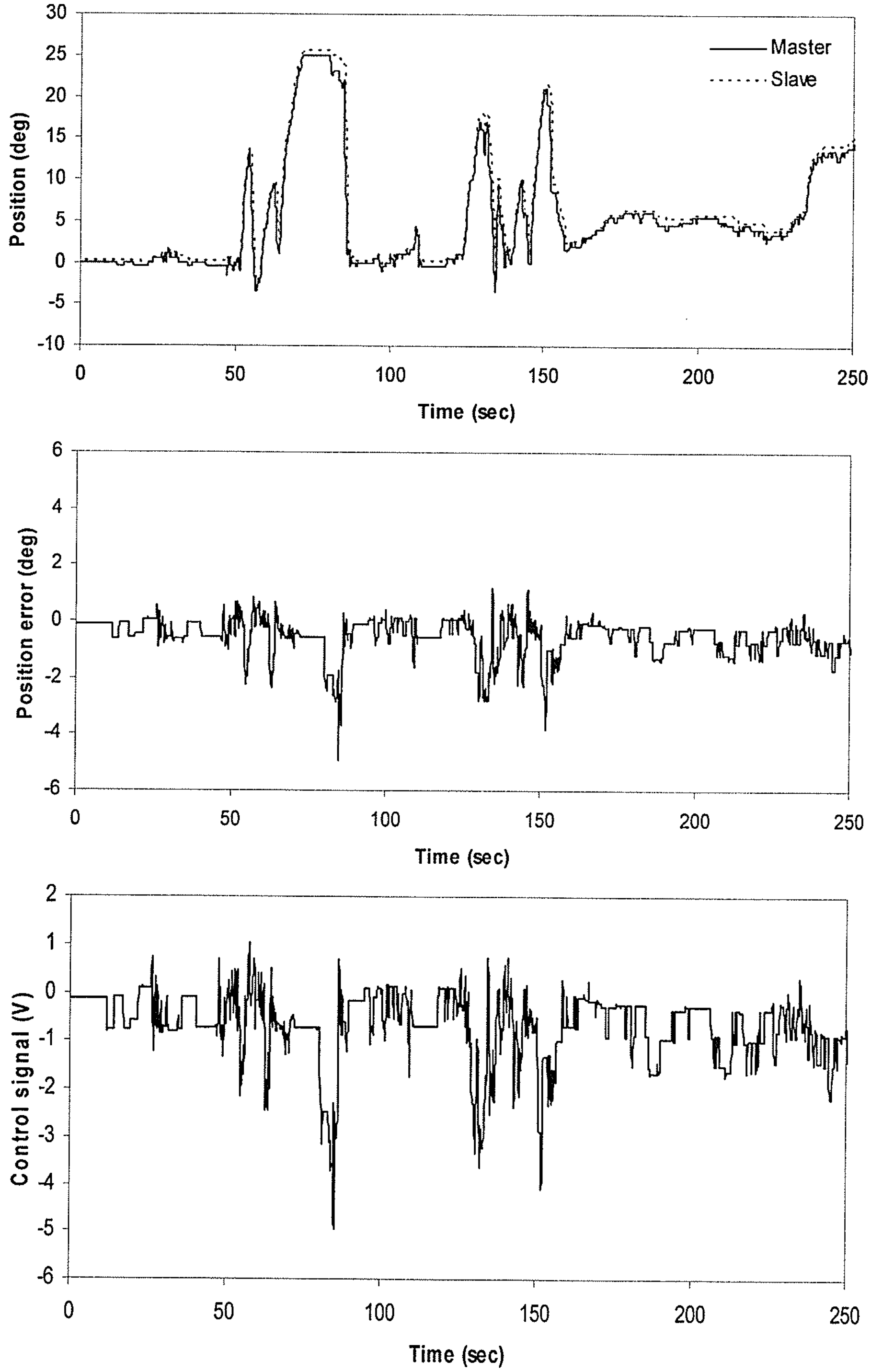

Figure 4-7. Typical position tracking response of pitch motion of ultrasound probe obtained by an ultrasound technologist during kidney examination (PD control gains: K_p=1.4 V/deg and K_v=0.06 Vs/deg).

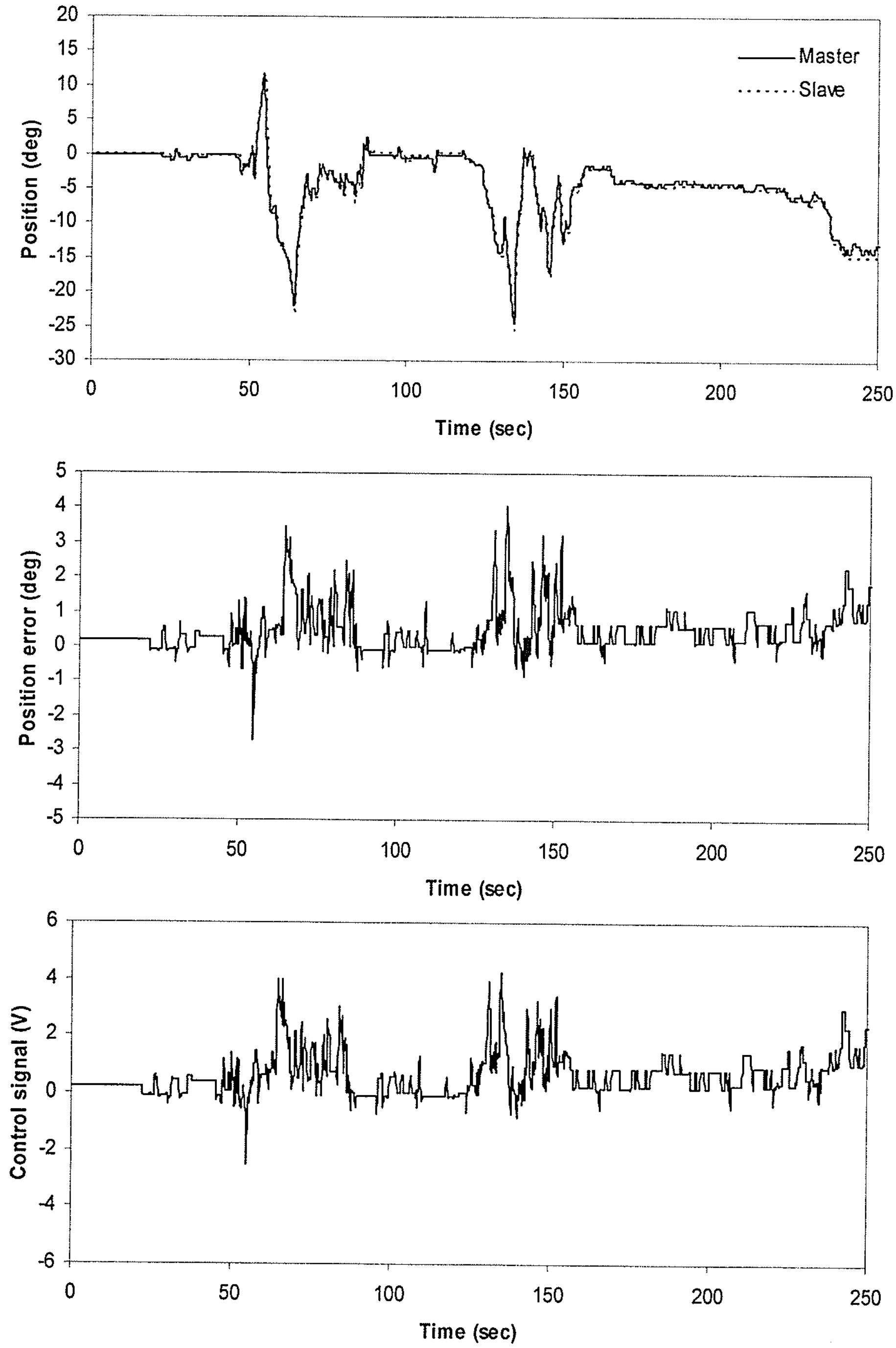

Figure 4-8. Typical position tracking response of yaw motion of ultrasound probe obtain ed by an ultrasound technologist in kidney examination (PD control gains: K_p=1.4 V/deg and K_v=0.06 Vs/deg).

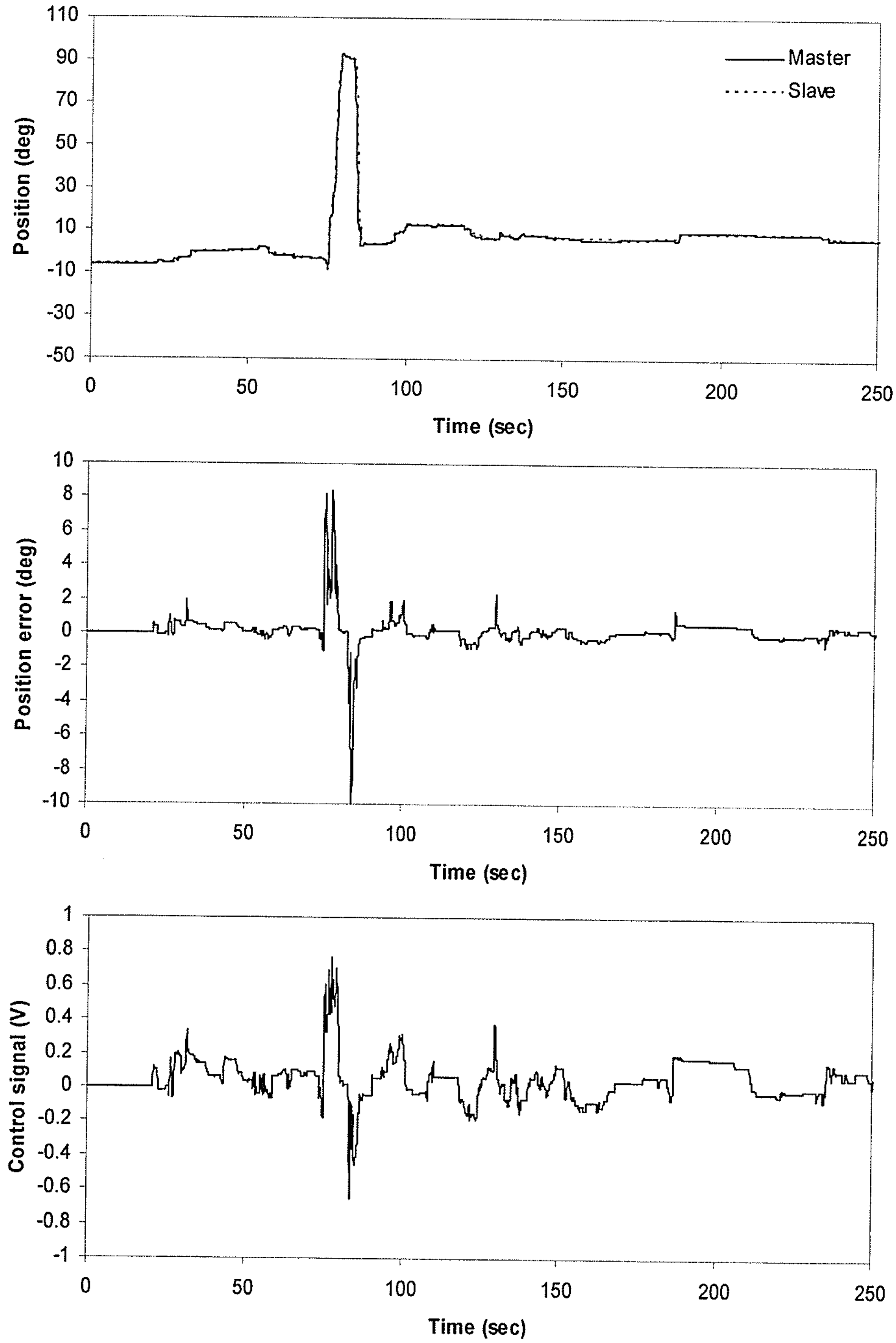

Figure 4-9. Typical position tracking response of rotational motion of ultrasound probe obtained by an ultrasound technologist during kidney examination (PD control gains: K_p=0.3 V/deg and K_v=0.03 Vs/deg).

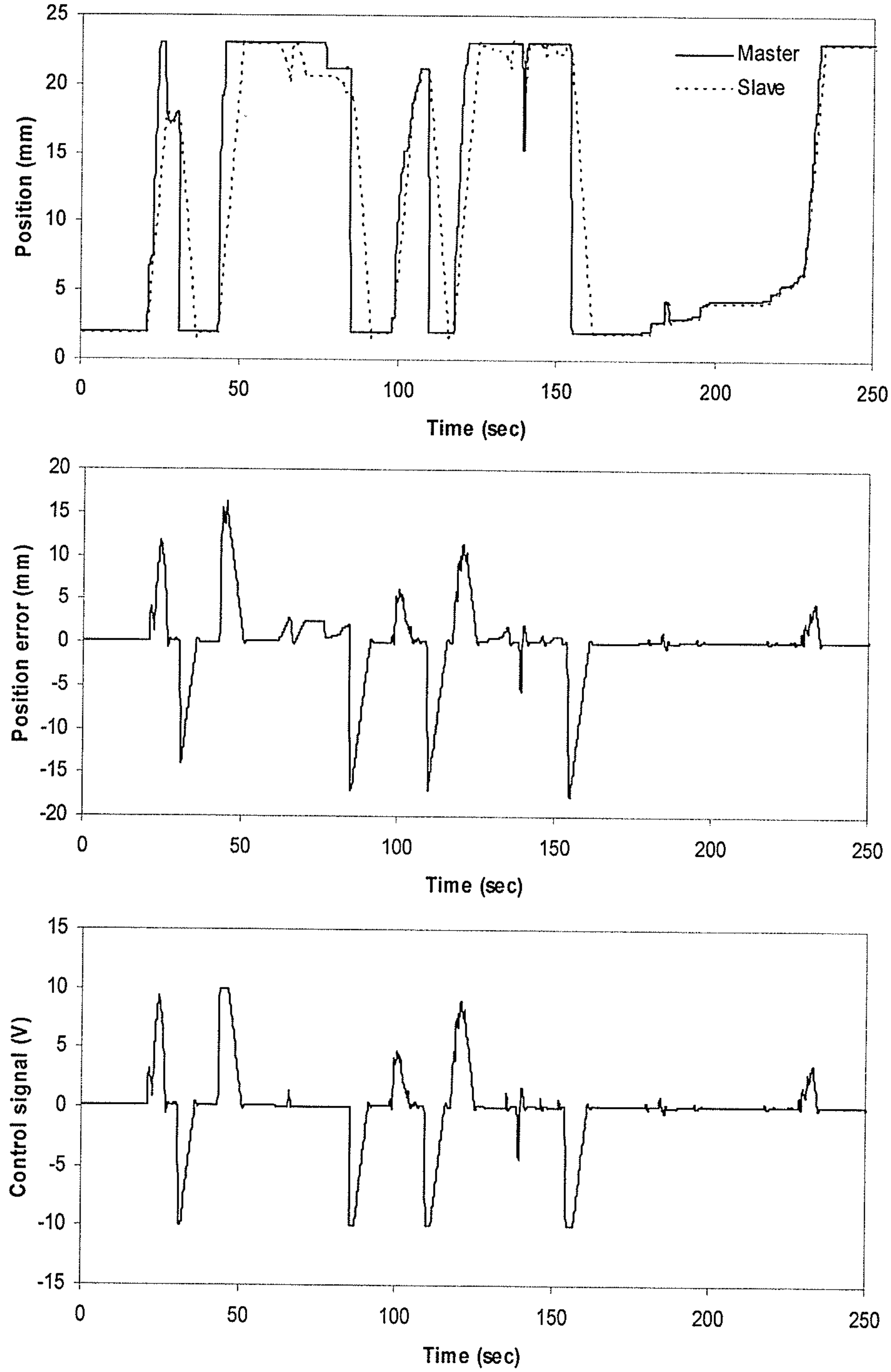

Figure 4-10. Typical position tracking response of palpating motion of ultrasound probe obtained by ultrasound technologist during kidney examination (PD control gains: K_p=0.8 V/mm and K_v=0.03 Vs/mm).

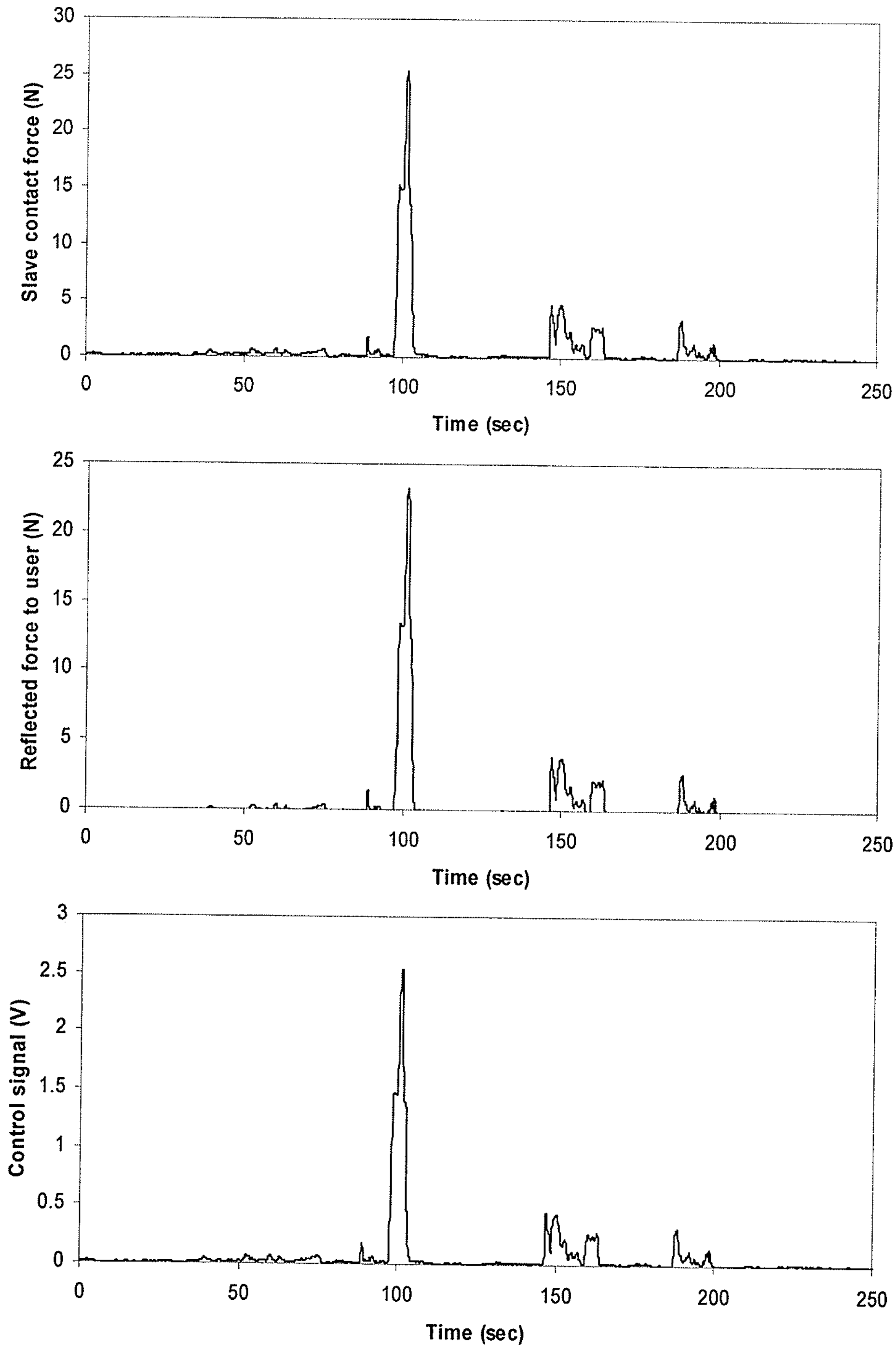

Figure 4-11. Typical force-tracking response between slave contact force and reflected force to ultrasound technologist hand along the axis of hand-grip during kidney examination.

Chapter 5

Conclusions

Ultrasound examination offers quick and reliable non-invasive examination. However the main drawback of current ultrasound techniques is that the quality of the examination is highly dependent on the operator's skills, which are often lacking in small medical centers and isolated areas. As a solution to this problem, a complete robotic system for remote ultrasound imaging has been developed in this thesis to assist specialized physicians to perform ultrasound examination on patients located in remote and isolated areas. The system consists of a 4-DoF robotic wrist and a 4-DoF hand-controller with force reflecting capability along the axis of the hand-grip. Their functionalities have been evaluated analytically and experimentally. From the robotic point-of-view, this is the most complete system for performing ultrasound imaging. The mechanical features of the entire robotic system were matched to what an ultrasound expert needed for ultrasound examination. Haptic feedback to operator's hand was helpful and enabled him to maintain the contact between the ultrasound probe and the patient's body and obtain continuous ultrasound images. Moreover, haptic feedback enabled the operator to adjust the amount of pressure between the probe and the patient's body. An ultrasound technologist from Winnipeg Children Hospital performed ultrasound imaging on few volunteers and he was able to locate the ultrasound probe over the area of interest on the patient's body, and change the orientation of the probe to capture images from desired anatomical targets. It was shown that meaningful ultrasound images of heart, kidney, spleen and liver can be obtained using the developed robotic system in this thesis.

5.1 Contributions of This Thesis

The developed robotic system features novel characteristics that have not been incorporated all in a single device. These features are described below.

1- Both the robotic wrist and the haptic device have been designed using parallel mechanisms to reduce the inertia of the moving elements by placing the actuators, as the main source of inertia, on the base. In the hand-controller, this characteristic improved the quality of force reflection to operators. In the robotic wrist, this feature reduced the inertial contact forces between the device and patient's body. This feature also facilitates the sterilization of the robotic wrist by placing the electric motors far from the ultrasound probe. This feature has not been considered in any other robotic devices designed for ultrasound imaging.

2- Kinematically decoupled DoFs is realizable in serial manipulators. However, it is far more difficult in parallel manipulators. Prior to this work, there was no parallel manipulator which had 4 kinematically decoupled DoFs. In this thesis, it was shown how the combination of dissimilar kinematic chains and decoupling ball bearings can lead to a parallel robotic wrist with kinematically decoupled DoFs. Kinematic decoupling in the proposed robotic wrist allowed one motion of the ultrasound probe by only actuating one kinematic chain which enhances the safety of manipulation. This is particularly important for the palpating motion of the robotic wrist in which the inertial forces of the moving parts involved in the contact force between the ultrasound probe and the patient's body can be reduced.

3- The force reflecting hand-controller has been statically balanced with a single tension spring. Other parallel manipulators with 3, 4 and 6 DoFs are statically balanced with 6 or 12 tension springs. The lower the numbers of springs, the less complex the mechanism is. Prior to this work, there was no parallel mechanism with 4 DoFs which was statically balanced with only one tension spring. Static balancing reduces physician's fatigue during remote manipulation since no operating effort for the actuators or the physicians, apart from acceleration and deceleration, is needed to move the device from one configuration to another configuration. Static balancing also improves the safety of remote examination in case of power failure or when the physician lets go of haptic.

4- The FCM of the haptic device and the RCM of the robotic wrist are necessary for 3-D ultrasound imaging. The FCM and RCM were created by hardware in the haptic and wrist mechanisms. They enhanced the safety of examination. In case of power failure, the FCM and RCM, keep the ultrasound probe in the limited workspace without causing injuries to the patient's body. There exist many parallel mechanisms with 3 DoFs having

FCM. However, prior to this work, there was no parallel mechanism with 4 DoFs which had either FCM or RCM. Hybrid parallel and serial mechanisms with 4 DoFs have previously been designed with RCM. In this thesis, it was shown how the usage of concentric universal telescoping joints and linkage mechanisms leads to a parallel robotic wrist with 4 DoFs having a RCM.

With respect to the remaining objectives of this thesis listed in Section 1.5 for the robotic wrist, the ultrasound probe moves in a conical workspace with a vertex angle as much as 50° which is free of any singular configuration. The palpating motion is about 32 mm and is able to generate palpating force up to 24 N. The maximum velocities of the probe during ultrasound examination for pitch, yaw, rotational, and palpating motions are 27 deg/s, 32 deg/s, 68 deg/s, and 3 mm/s, respectively. The weight of the moving elements of the 4-DoF wrist is 2.5 kg. Moving elements of the wrist except the ultrasound probe are far from the patient and there is access to the patient by the attending nurse.

With respect to the remaining objectives listed in this thesis for the haptic device, the device utilizes parallel mechanisms to enhance its structural rigidity. The workspace of the hand-controller is a cone with a vertex angle as much as 70°. The sliding motion of the hand-grip is 32 mm. The workspace of the device is singularity-free and all DoFs are backdriveable. The operator's hand gestures when she/he holds the hand-grip is similar to holding an ultrasound probe. The weight of the moving elements of the device is 452 gr. The DoFs in the haptic and the wrist have one-to-one position correspondence to reduce operator's mental load from thinking of the relative position between her/his hand and the probe.

5.2 Future Work

The following tasks can be performed to make the developed robotic system available for daily clinical practice.

- **Image Compression and Transmission**

Appropriate algorithms should be used for real-time compression, transmission and recovery of ultrasound images between physician and patient sides connected by a private and reliable Internet or ISDN communication systems.

- **Synchronization of Haptic and Ultrasound Images**

There is no guarantee that both haptic information and ultrasound images reach to the physician at the same time especially in the presence of communication delays. Therefore, the effect of network delays on the performance of remote ultrasound examination should be investigated.

- **Stability of the Robotic System**

Stability of the tele-robotic system must be guaranteed, in the presence of network delays, using one of the well-known methods such as passivity (Anderson and Spong 1989), wave-variables (Niemeyer and Slotine 1998), and event-based (Xi and Tarn 2000).

- **Clinical Evaluation**

Comprehensive clinical testing of the entire robotic system must be performed on patients to investigate the examination efficiency of the developed system when used for a large population of patients with different health conditions. The ultrasound images obtained by the robotic system must be similar with those obtained from standard ultrasound examinations performed directly on the patients.

- **Assessment of Patient's Satisfaction**

The ultrasound probe is in continuous contact with patient's body in ultrasound examination. Therefore, patient's satisfaction and comfort are crucial. For example, patient's satisfaction, in terms of fear of using the robotic wrist for examination or the amount pressure applied by the wrist must be examined through questionnaires during clinical testing of the developed system.

Appendix A:

Derivation of Eq. (2.2)

With reference to Figure a-1a, axis Z_{t1} is normal to axis X_t, and is located in the plane X_0Z_0. Axis Z_{t1} is also located in the plane containing axes Z_{t1} and Y_0. This plane is normal to axis X_t at point O. When the input shaft of the first pantograph rotates as much as θ_1, vector OF_1^1 rotates to OF_1^2 as much as β_1 (see Figures a-1a and a-1b). This motion happens in plane Y_0Z. The corresponding vector $O\widehat{F}_1^1$ rotates to $O\widehat{F}_1^2$ as much as θ_1 in plane Y_0Z_{t1} (see Figures a-1a and a-1d). The orientation of plane Z_0Y_0 with respect to plane $Z_{t1}Y_0$ is shown in Figure a-1c. The projections of vector OF_1^1 on axes Y_0 and Z_0 are shown as OM_1^2 and ON_1^2, respectively (Figures a-1a and a-1b). The projections of vector $O\widehat{F}_1^2$ on axes Y_0 and Z_{t1} are shown as OM_1^2 and $O\widehat{N}_1^2$, respectively (Figures a-1a and a-1d).

According to Figure a-1b, the following relationships hold:

$$OF_1^1 = OF_1^2 \tag{a.1a}$$

$$OM_1^2 = OF_1^1 \sin\beta_1 \tag{a.1b}$$

$$ON_1^2 = OF_1^1 \cos\beta_1 \tag{a.1c}$$

Referring to Figures a-1b, a-1c and a-1d, one can write:

$$O\widehat{N}_1^2 = ON_1^2 \cos\alpha \tag{a.2}$$

Substituting Eq. (a.1c) into Eq. (a.2):

$$O\widehat{N}_1^2 = OF_1^1 \cos\beta_1 \cos\alpha \tag{a.3}$$

With reference to Figure a-1d, the following relationship can be obtained:

$$\tan\theta_1 = \frac{OM_1^2}{O\widehat{N}_1^2} \tag{a.4}$$

Substituting Eqs. (a.1b) and (a.3) into Eq. (a.4), one can see:

$$\tan\theta_1 = \frac{\tan\beta_1}{\cos\alpha} \tag{a.5}$$

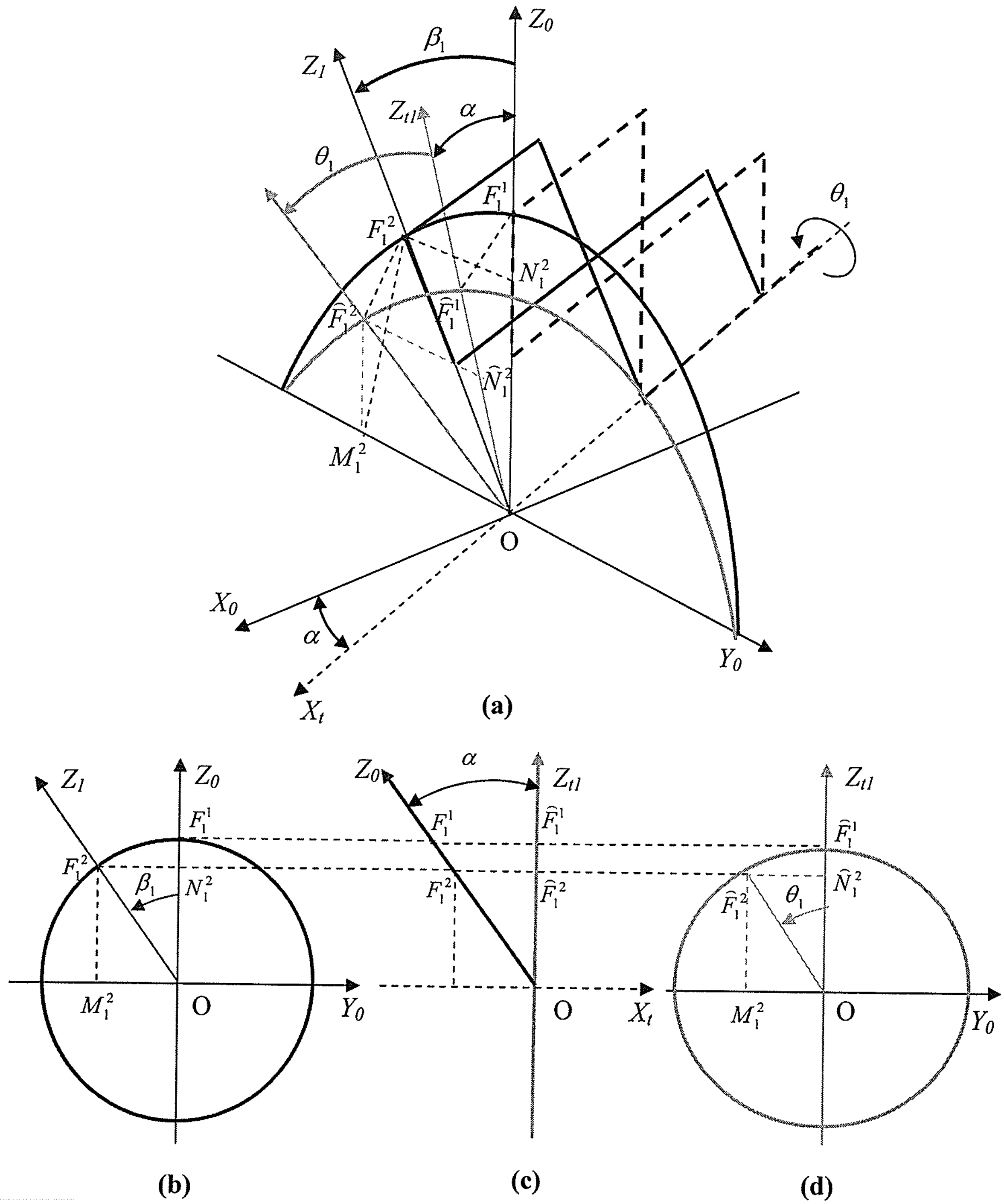

Figure a-1. (a) Relation between rotation, θ_1, of the input link about axis X_t and rotation of axis Z_0, β_1, about axis X_0; (b) projection on plane Z_0Y_0; (c) orientation of plane $Z_{t1}Y_0$ with respect to plane Z_0Y_0; (d) vector $O\widehat{F}_1^1$ rotates as much as θ_1 to reach to $O\widehat{F}_1^2$ in plane $Z_{t1}Y_0$ normal to axis X_t.

Appendix B:

Derivation of Eq. (2.6a)

With reference to Figure b-1a, axis Z_{t2} is normal to axis X_t and is located in the plane containing X_tZ_1. The normal to plane X_tZ_1 is defined by unit vector $\vec{S}$ (Figure b-1a). The axis Z_{t3} is located in the plane $Z_{t3}X_0$ which is normal to axis Y_t at point O. The axis Z_{t3} is also located in plane Z_0Y_0 (see Figures b-1a and b-1b). Figure b-1c shows the orientation of plane $Z_{t3}X_0$ with respect to plane Z_0X_0. When the input shaft of the second pantograph rotates as much as θ_2, in the plane normal to Y_t at point O (plane $Z_{t3}X_0$), the vector $O\hat{\hat{F}}_1^2$ moves to $O\hat{\hat{F}}_1^3$ where the angle between $O\hat{\hat{F}}_1^2$ and $O\hat{\hat{F}}_1^3$ is θ_2 (Figures b-1a and b-1b). This also causes axis Z_1 to rotate as much as β_2 to reach to axis Z_2 (Figures b-1a and b-1d). Therefore, the vector OF_1^2 moves to OF_1^3 in plane X_tZ_1 (see Figures b-1a and b-1d).

With reference to Figures b-1a and b-1b, the unit vector $O\hat{\hat{F}}_1^3$ has the projections on axes X_0 and Z_{t3}. These projections can be calculated as follows:

$$OW_1^3 = \sin\theta_2 \tag{b.1a}$$

$$OP_1^3 = \cos\theta_2 \tag{b.1b}$$

With reference to Figures b-1b and b-1c, vector OP_1^3 has projections on the axes Z_0 and X_0. Therefore, the unit vector $O\hat{\hat{F}}_1^3$ can be described in fixed frame $\{X_0Y_0Z_0\}$ as:

$$^0O\hat{\hat{F}}_1^3 = \left(\sin\theta_2 \quad \cos\theta_2\sin\alpha \quad \cos\theta_2\cos\alpha\right)^T \tag{b.2}$$

In the plane containing axes X_t and Z_1, axis Z_{t2} is normal to X_t at point O (Figures b-1a and b-1d). The unit vector $\vec{S}$ is normal to plane X_tZ_1. Axis Z_{t2} is located in plane X_tZ_1. Therefore, vector S is normal to axes Z_{t2} and X_t and the unit vector along axis Z_{t2} can be calculated as:

$$
{}^{0}Z_{t2} = {}^{0}X_t \times {}^{0}S = \begin{pmatrix} s_y \sin\alpha \\ -(s_x \sin\alpha + s_z \cos\alpha) \\ s_y \cos\alpha \end{pmatrix} \tag{b.3}
$$

where

$$
{}^{0}X_t = (\cos\alpha \quad 0 \quad -\sin\alpha)^T
$$

$$
{}^{0}S = (s_x \quad s_y \quad s_z)^T
$$

The projections of vector ${}^{0}O\hat{\hat{F}}_1^3$ on axes X_t and Z_{t2} (Figures b-1a and b-1d) can be calculated as:

$$
OQ_1^3 = {}^{0}O\hat{\hat{F}}_1^3 \cdot {}^{0}X_t = \sin\theta_2 \cos\alpha - \cos\theta_2 \cos\alpha \sin\alpha \tag{b.4.a}
$$

$$
OV_1^3 = {}^{0}O\hat{\hat{F}}_1^3 \cdot {}^{0}Z_{t2} = s_y \sin\alpha \sin\theta_2 - \sin\alpha \cos\theta_2 (s_x \sin\alpha + s_z \cos\alpha) + s_y \cos^2\alpha \cos\theta_2 \tag{b.4b}
$$

Therefore, with reference to Figure b-1d and using Eqs. (b.4a) and (b.4b), one arrives at Eq.(2.6a):

$$
\tan(\beta_2 - \eta) = \frac{OQ_1^3}{OV_1^3} = \frac{\sin\theta_2 \cos\alpha - \cos\theta_2 \cos\alpha \sin\alpha}{s_y \sin\alpha \sin\theta_2 - \sin\alpha \cos\theta_2 (s_x \sin\alpha + s_z \cos\alpha) + s_y \cos^2\alpha \cos\theta_2} \tag{b.5}
$$

where η can be calculated from the following relation:

$$
\cos\eta = {}^{0}Z_{t2} \cdot {}^{0}Z_1 = \sin\beta_1 (s_x \cos\alpha + s_z \sin\alpha) + s_y \cos\beta_1 \cos\alpha \tag{b.6}
$$

and ${}^{0}Z_1$ can be obtained from Eq. (2.1). Angle γ in Figure b-1d can be calculated from the following relationsship:

$$
\cos\gamma = {}^{0}Z_1 \cdot {}^{0}X_t = \sin\alpha \cos\beta_1 \tag{b.7}
$$

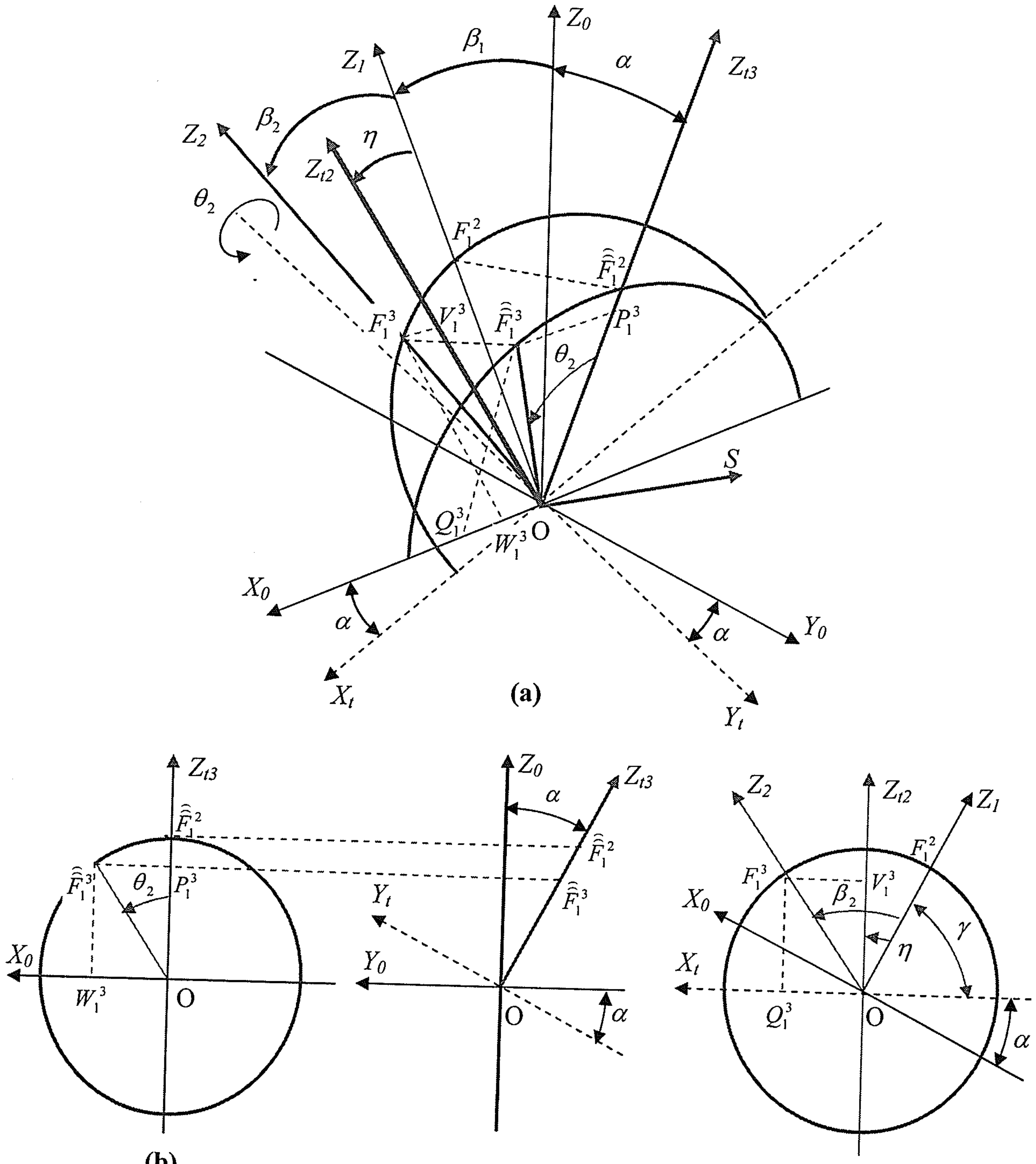

Figure b-1. (a) Relation between rotation, θ_2, of input link about axis Y_t and rotation of axis Z_1, β_2, around vector S; (b) unit vector $O\hat{\hat{F}}_1^2$ rotates in plane $Z_{t3}X_0$ as much as θ_2 to reach to $O\hat{\hat{F}}_1^3$ (c) orientation of plane $Z_{t3}X_0$ with respect to plane Z_0X_0; (d) axis Z_1 rotates in plane $Z_{t2}X_0$ as much as β_2.

Appendix C:

Derivation of the Jacobian Matrix of the Wrist

With reference to Figure 2-7, given actuators velocities $\dot{\theta}_1^m, \dot{\theta}_2^m, \dot{\theta}_3^m$, and $\dot{\theta}_4^m$, the objective is to find the velocity state of the moving frame $\{X_m Y_m Z_m\}$ attached to the ultrasound probe. Actuators and moving platform velocities are related together by a Jacobian matrix. The velocity vector of the moving platform $\{X_m Y_m Z_m\}$ can be described in the fixed frame $\{X_0 Y_0 Z_0\}$ by $[\vec{\omega}\ \vec{V}]^T$ where $\vec{\omega}$ and $\vec{V}$ are angular and linear velocity vectors, respectively.

The third and fourth DoFs are kinematically decoupled from the first two DoFs generated by pantographs. Their power trains idly follow the first two DoFs while transmitting motions to the combinatory module. Thus, the derivation of the Jacobian matrix of the first two DoFs are described first. The conventional velocity vector-loop method as described by Tsai (1999) has been used. Since the mechanism shown in Figure c-1 possesses only two rotations, the input vector can be written as $\Theta = [\dot{\theta}_1^m\ \ \dot{\theta}_2^m]^T$ and the output vector can be described by the angular velocity of the end-link EF, $\dot{X} = [\omega_x\ \ \omega_y]^T$.

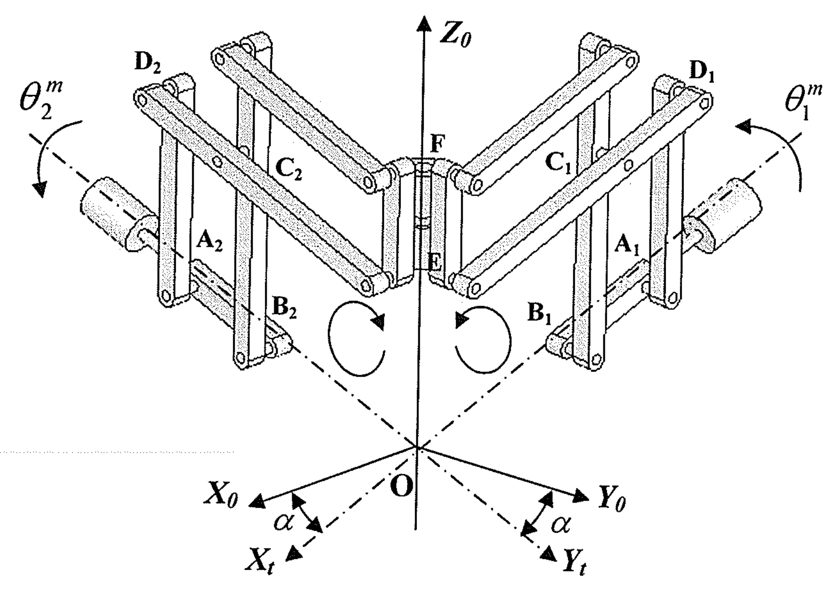

Figure c-1. Kinematic chain of two pantographs.

Referring to Figure c-1, a loop-closure equation for the ith pantograph $(i=1,2)$ can be written as:

$$\overrightarrow{OE}=\overrightarrow{OB_i}+\overrightarrow{B_iC_i}+\overrightarrow{C_iE} \qquad (i=1,2) \tag{c.1}$$

Taking derivative of Eq. (c.1) with respect to time yields a velocity vector-loop equation:

$$\overrightarrow{V_E}=\overrightarrow{\omega_{B_iC_i}}\times\overrightarrow{B_iC_i}+\overrightarrow{\omega_{C_iE}}\times\overrightarrow{C_iE} \qquad (i=1,2) \tag{c.2}$$

where $\overrightarrow{\omega_{B_iC_i}}$ and $\overrightarrow{\omega_{C_iE}}$ are the angular velocities of links B_iC_i and C_iE, respectively. In order to eliminate $\overrightarrow{\omega_{C_iE}}$ from Eq. (c.2), both sides of Eq. (c.2) are dot-multiplied by $\overrightarrow{C_iE}$.

$$\overrightarrow{C_iE}\cdot(\overrightarrow{V_E})=(\overrightarrow{B_iC_i}\times\overrightarrow{C_iE})\cdot\overrightarrow{\omega_{B_iC_i}} \qquad (i=1,2) \tag{c.3}$$

The polygon OB_iC_iE in Figure c-1 is a parallelogram. Therefore, the vectors $\overrightarrow{B_iC_i}$ and $\overrightarrow{C_iE}$ are equal to $\overrightarrow{OE}$ and $\overrightarrow{B_iO}$, respectively. Eq. (c.3) can then be written as:

$$\overrightarrow{C_iE}\cdot(\overrightarrow{V_E})=(\overrightarrow{OE}\times\overrightarrow{C_iE})\cdot\overrightarrow{\omega_{OE}} \qquad (i=1,2) \tag{c.4}$$

Using Eq. (2.8), vector $\overrightarrow{OE}$ in Figure c-1 can be written as:

$$\overrightarrow{OE}=\begin{bmatrix}e_x & e_y & e_z\end{bmatrix}^T=e.\begin{pmatrix}-a_{12}s\beta_1+a_{13}c\beta_1\\ -a_{22}s\beta_1+a_{23}c\beta_1\\ -a_{32}s\beta_1+a_{33}c\beta_1\end{pmatrix} \tag{c.5}$$

where $e=\sqrt{(e_x^2+e_y^2+e_z^2)}$ is the length of the vector $\overrightarrow{OE}$ (see Figure c-1). Taking derivative of Eq. (c.5) with respect to time, we have:

$$\overrightarrow{V_E}=\begin{bmatrix}\dot{e}_x & \dot{e}_y & \dot{e}_z\end{bmatrix}^T \tag{c.6}$$

where $\overrightarrow{C_1E}=\overrightarrow{B_1O}=\begin{bmatrix}-bc\alpha & 0 & bs\alpha\end{bmatrix}^T$ and $\overrightarrow{C_2E}=\overrightarrow{B_2O}=\begin{bmatrix}0 & -bc\alpha & bs\alpha\end{bmatrix}^T$ in which b is the length of vector $\overrightarrow{B_iO}$. By substituting Eq. (c.6) into the left-hand side of Eq. (c.4) we have:

$$\overrightarrow{C_iE}\cdot\overrightarrow{V_E}=\begin{pmatrix}-b\dot{e}_x c\alpha+b\dot{e}_z s\alpha\\ -b\dot{e}_y c\alpha+b\dot{e}_z s\alpha\end{pmatrix}=\begin{pmatrix}l_{11} & l_{12}\\ l_{21} & l_{22}\end{pmatrix}\begin{pmatrix}\dot{\theta}_1^m\\ \dot{\theta}_2^m\end{pmatrix}$$

where

$$l_{11}=-b(m_1m_9+m_2m_8m_9)c\alpha+b(m_5m_9+m_6m_8m_9)s\alpha\,; \qquad l_{12}=-bm_2m_7c\alpha+bm_6m_7s\alpha$$

$$l_{21}=-b(m_3m_9+m_4m_8m_9)c\alpha+b(m_5m_9+m_6m_8m_9)s\alpha\,; \qquad l_{22}=-bm_4m_7c\alpha+bm_6m_7s\alpha$$

and

$$m_1=\frac{-e\,c\alpha\,s^2\alpha\,s2\beta_1\,s\beta_2}{(1-s^2\alpha\,c^2\beta_1)^{3/2}}$$

$$m_2=\frac{e\,c\alpha\,c\beta_2}{(1-s^2\alpha\,c^2\beta_1)^{3/2}}$$

$$m_3=e(-c\beta_1\,c\beta_2-\frac{s\alpha\,c^2\beta_1\,s\beta_2}{(1-s^2\alpha\,c^2\beta_1)^{1/2}}+\frac{s^3\alpha\,s^2 2\beta_1\,s\beta_2}{2(1-s^2\alpha\,c^2\beta_1)^{3/2}})$$

$$m_4=e(s\beta_1\,s\beta_2-\frac{s\alpha\,s2\beta_1\,c\beta_2}{2(1-s^2\alpha\,c^2\beta_1)^{1/2}})$$

$$m_5=e(-s\beta_1\,c\beta_2-\frac{s\alpha\,s2\beta_1\,s\beta_2}{(1-s^2\alpha\,c^2\beta_1)^{1/2}}+\frac{s^3\alpha\,s2\beta_1\,s^2\beta_1\,s\beta_2}{(1-s^2\alpha\,c^2\beta_1)^{3/2}}) \tag{c.7}$$

$$m_6=e(-c\beta_1\,s\beta_2-\frac{s\alpha\,s^2\beta_1\,c\beta_2}{(1-s^2\alpha\,c^2\beta_1)^{1/2}})$$

$$m_7=\frac{(c\alpha-s\alpha)\,c^2(\beta_2-\eta)\,(1-s^2\alpha c^2\beta_1)^{1/2}}{(t\theta_2-s\alpha)^2 s\alpha\,c\beta_1\,c^2\theta_2}$$

$$m_8=(\frac{-2s^3\alpha\,s\beta_1\,c^2\beta_1\,(1-s^2\alpha\,c^2\beta_1)^{-1/2}-s\alpha\,s\beta_1\,(1-s^2\alpha\,c^2\beta_1)^{1/2}}{s^2\alpha\,c^2\beta_1})(\frac{t\theta_2-c\alpha}{t\theta_2-s\alpha})$$

$$m_9=\frac{c\alpha\,c^2\beta_1}{c^2\theta_1}$$

Note t denotes "tan" function. The right-hand side of Eq. (c.4) can be written as:

$$(\overrightarrow{OE}\times\overrightarrow{C_iE})\cdot\overrightarrow{\omega_{OE}}=\begin{pmatrix}(\overrightarrow{OE}\times\overrightarrow{C_1E})\\ (\overrightarrow{OE}\times\overrightarrow{C_2E})\end{pmatrix}\begin{pmatrix}\omega_x\\ \omega_y\end{pmatrix}=\begin{pmatrix}r_{11} & r_{12}\\ r_{21} & r_{22}\end{pmatrix}\begin{pmatrix}\omega_x\\ \omega_y\end{pmatrix}$$

where

$$r_{11} = be_y s\alpha\,;\; r_{12} = -b(e_x s\alpha + e_z c\alpha)\,;\; r_{21} = b(e_y s\alpha + e_z c\alpha)\,;\; r_{22} = -be_x s\alpha \tag{c.8}$$

Equating right-hand sides of Eqs. (c.7) and (c.8), we will have:

$$\begin{pmatrix}\omega_{1x}\\ \omega_{1y}\end{pmatrix} = \begin{pmatrix} r_{11} & r_{12}\\ r_{21} & r_{22}\end{pmatrix}^{-1}\begin{pmatrix} l_{11} & l_{12}\\ l_{21} & l_{22}\end{pmatrix}\begin{pmatrix}\dot{\theta}_1^m\\ \dot{\theta}_2^m\end{pmatrix} = \begin{pmatrix} n_{11} & n_{12}\\ n_{21} & n_{22}\end{pmatrix}\begin{pmatrix}\dot{\theta}_1^m\\ \dot{\theta}_2^m\end{pmatrix} \tag{c.9}$$

where

$$n_{11} = \frac{r_{22}l_{11} - r_{12}l_{21}}{r_{11}r_{22} - r_{12}r_{21}};\; n_{12} = \frac{r_{22}l_{12} - r_{12}l_{22}}{r_{11}r_{22} - r_{12}r_{21}}\;;\; n_{21} = \frac{r_{11}l_{21} - r_{21}l_{11}}{r_{11}r_{22} - r_{12}r_{21}}\;;\; n_{22} = \frac{r_{11}l_{22} - r_{21}l_{12}}{r_{11}r_{22} - r_{12}r_{21}}$$

The second component of $\vec{\omega}$ comes from the rotational velocity $\dot{\theta}_3$ of the ultrasound probe. The rotational velocity has projections on the axes of the fixed frame $\{X_0Y_0Z_0\}$. These projections can be obtained from the following Eq.:

$$\begin{bmatrix}\omega_{2x} & \omega_{2y} & \omega_{2z}\end{bmatrix}^T = Rot(\beta_2, S)Rot(\beta_1, X_0)\begin{bmatrix}0 & 0 & \dot{\theta}_3\end{bmatrix}^T = \begin{pmatrix}(-a_{12}s\beta_1 + a_{13}c\beta_1)\dot{\theta}_3\\ (-a_{22}s\beta_1 + a_{23}c\beta_1)\dot{\theta}_3\\ (-a_{32}s\beta_1 + a_{33}c\beta_1)\dot{\theta}_3\end{pmatrix} \tag{c.10}$$

The relationship between $\dot{\theta}_3$ and $\dot{\theta}_3^m$ can be found using Eqs. (2.9), (2.10), (2.11), and (2.12) as follows:

$$\dot{\theta}_3 = m_{10}\dot{\theta}_3^m + m_6 m_7 m_{11}\dot{\theta}_2^m + m_9 m_{11}(m_5 + m_6 m_8)\dot{\theta}_1^m \tag{c.11}$$

where

$$m_{10} = -\frac{c^2\phi_1\, c^2\theta_3}{c\phi_2\, c^2\theta_3^m};\; m_{11} = \frac{c^2\theta_3}{s\psi\, c\phi_2}(ac\psi\, t\phi_1\, t\theta_3^m - bc\psi\, t\phi_2\, t\theta_3)\,;\; a = \frac{OR}{QR};\; b = \frac{OQ}{OR}$$

Parameters m_5, m_6, m_7, m_8, and m_9 are given in Eq. (c.7). By adding the right-hand sides of Eqs. (c.9) and (c.10), we will have the angular velocity vector $\vec{\omega}$ described in fixed frame $\{X_0Y_0Z_0\}$:

$$\vec{\omega}=\begin{pmatrix}\omega_X\\ \omega_Y\\ \omega_Z\end{pmatrix}=\begin{pmatrix}\omega_{1x}+\omega_{2x}\\ \omega_{1y}+\omega_{2y}\\ \omega_{2z}\end{pmatrix}=\begin{pmatrix}(n_{11}+gm_9m_{11}(m_5+m_6m_8))\dot{\theta}_1^m+(n_{12}+gm_6m_7m_{11})\dot{\theta}_2^m+gm_{10}\dot{\theta}_3^m\\ (n_{21}+dm_9m_{11}(m_5+m_6m_8))\dot{\theta}_1^m+(n_{22}+dm_6m_7m_{11})\dot{\theta}_2^m+dm_{10}\dot{\theta}_3^m\\ fm_9m_{11}(m_5+m_6m_8)\dot{\theta}_1^m+fm_6m_7m_{11}\dot{\theta}_2^m+fm_{10}\dot{\theta}_3^m\end{pmatrix}$$

where

$$g=(-a_{12}s\beta_1+a_{13}c\beta_1)\ ;\ d=(-a_{22}s\beta_1+a_{23}c\beta_1);\ \ f=(-a_{32}s\beta_1+a_{33}c\beta_1) \qquad \text{(c.12)}$$

The linear velocity vector, $\vec{V}=[V_X \quad V_Y \quad V_Z]^T$, of the moving platform also has two components. The first component of $\vec{V}$ is due to the angular velocity $\vec{\omega}$ of moving platform $\{X_mY_mZ_m\}$, which can be described as:

$$[V_{1x} \quad V_{1Y} \quad V_{1Z}]^T=\vec{\omega}\times\vec{r}=[\omega_Y r_z-\omega_Z r_y \quad \omega_Z r_x-\omega_X r_z \quad \omega_X r_y-\omega_Y r_x]^{\mathrm{T}} \qquad \text{(c.13)}$$

where $\vec{r}$ is the palpating motion of the ultrasound probe describing the distance between frames $\{X_0Y_0Z_0\}$ and $\{X_mY_mZ_m\}$ in fixed frame $\{X_0Y_0Z_0\}$ (see Figure 2-7). Therefore $\vec{r}$ can be described as:

$$\vec{r}=[r_x \quad r_y \quad r_z]^T=Rot(\beta_2,S)Rot(\beta_1,X_0)[0 \quad 0 \quad r]^T=\begin{pmatrix}(-a_{12}s\beta_1+a_{13}c\beta_1)r\\ (-a_{22}s\beta_1+a_{23}c\beta_1)r\\ (-a_{32}s\beta_1+a_{33}c\beta_1)r\end{pmatrix} \qquad \text{(c.14)}$$

r is the magnitude of $\vec{r}$ and can be calculated by substituting Eq. (2.14) into Eq. (2.13):

$$r=\frac{nP}{2\pi}\tan^{-1}(\tan\theta_4^m\frac{\cos\phi_1}{\cos\phi_2}) \qquad \text{(c.15)}$$

where θ_4^m is the motor angular position which provides the palpating motion of the ultrasound probe.

By substituting Eqs. (c.14) and (c.15) into Eq. (c.13) we will have:

$$V_{1x}=(n_{21}r_z+m_9m_{11}(m_5+m_6m_8)(dr_z-fr_y))\dot{\theta}_1^m+(n_{22}r_z+m_6m_7m_{11}(dr_z-fr_y))\dot{\theta}_2^m$$
$$+m_{10}(dr_z-fr_y)\dot{\theta}_3^m$$

$$V_{1y}=(-n_{11}r_z+m_9m_{11}(m_5+m_6m_8)(fr_x-gr_z))\dot{\theta}_1^m+(-n_{12}r_z+m_6m_7m_{11}(fr_x-gr_z))\dot{\theta}_2^m$$
$$+m_{10}(fr_x-gr_z)\dot{\theta}_3^m$$

$$V_{1z} = (n_{11}r_y - n_{21}r_x + m_9 m_{11}(m_5 + m_6 m_8)(gr_y - dr_x))\dot{\theta}_1^m + (n_{12}r_y - n_{22}r_x + m_6 m_7 m_{11}(gr_y - dr_x))\dot{\theta}_2^m + m_{10}(gr_y - dr_x)\dot{\theta}_3^m \quad \text{(c.16)}$$

The second component of $\vec{V}$ is the effect of linear velocity (palpation velocity) $\dot{r}$ of the moving platform $\{X_m Y_m Z_m\}$. This linear velocity has projections on the axes of the fixed frame $\{X_0 Y_0 Z_0\}$. These projections are obtained as shown below:

$$\begin{bmatrix} V_{2x} & V_{2y} & V_{2z} \end{bmatrix}^T = Rot(\beta_2, S) Rot(\beta_1, X_0) \begin{bmatrix} 0 & 0 & \dot{r} \end{bmatrix}^T = \begin{pmatrix} (-a_{12}s\beta_1 + a_{13}c\beta_1)\dot{r} \\ (-a_{22}s\beta_1 + a_{23}c\beta_1)\dot{r} \\ (-a_{32}s\beta_1 + a_{33}c\beta_1)\dot{r} \end{pmatrix} \quad \text{(c.17)}$$

$\dot{r}$ is the magnitude of $\vec{\dot{r}}$ and can be calculated by:

$$\dot{r} = \frac{nP(m_9 m_{11}(m_5 + m_6 m_8)\dot{\theta}_1^m + m_6 m_7 m_{11}\dot{\theta}_2^m + m_{10}\dot{\theta}_4^m)}{2\pi} \quad \text{(c.18)}$$

In Eq. (c.18), $\dot{\theta}_4^m$ is the motor angular velocity which provides the palpating motion of the ultrasound probe.

By substituting Eq. (c.18) into Eq. (c.17) and some mathematical manipulation, the following relationships can be obtained:

$$\begin{aligned} V_{2x} &= \frac{gnP}{2\pi}(m_9 m_{11}(m_5 + m_6 m_8)\dot{\theta}_1^m + m_6 m_7 m_{11}\dot{\theta}_2^m + m_{10}\dot{\theta}_4^m) \\ V_{2y} &= \frac{dnP}{2\pi}(m_9 m_{11}(m_5 + m_6 m_8)\dot{\theta}_1^m + m_6 m_7 m_{11}\dot{\theta}_2^m + m_{10}\dot{\theta}_4^m) \\ V_{2z} &= \frac{fnP}{2\pi}(m_9 m_{11}(m_5 + m_6 m_8)\dot{\theta}_1^m + m_6 m_7 m_{11}\dot{\theta}_2^m + m_{10}\dot{\theta}_4^m) \end{aligned} \quad \text{(c.19)}$$

By adding Eqs. (c.16) and (c.19), we will have the linear velocity vector $\vec{V}$ of the moving frame $\{X_m Y_m Z_m\}$ described in fixed frame $\{X_0 Y_0 Z_0\}$:

$$\vec{V} = \begin{bmatrix} V_x & V_y & V_z \end{bmatrix}^T = \begin{bmatrix} V_{1x} + V_{2x} \\ V_{1y} + V_{2y} \\ V_{1z} + V_{2z} \end{bmatrix} \quad \text{(c.20)}$$

By considering Eqs. (c.12) and (c.20), the Jacobian matrix can be obtained:

$$\left[\vec{\omega} \quad \vec{V}\right]^T{}_{(6\times1)} = \left[J\right]_{(6\times4)} \cdot \left[\dot{\theta}_1^m \quad \dot{\theta}_2^m \quad \dot{\theta}_3^m \quad \dot{\theta}_4^m\right]^T$$

where

$$J_{11} = n_{11} + gm_9 m_{11}(m_5 + m_6 m_8);\ \ J_{12} = n_{12} + gm_6 m_7 m_{11};\ J_{13} = gm_{10};\ \ J_{14} = 0$$

$$J_{21} = n_{21} + dm_9 m_{11}(m_5 + m_6 m_8),\ \ J_{22} = n_{22} + dm_6 m_7 m_{11};\ J_{23} = dm_{10};\ J_{24} = 0$$

$$J_{31} = fm_9 m_{11}(m_5 + m_6 m_8);\ J_{32} = fm_6 m_7 m_{11};\ J_{33} = fm_{10};\ J_{34} = 0$$

$$J_{41} = n_{21} r_z + m_9 m_{11}(m_5 + m_6 m_8)(dr_z - fr_y + \frac{gnP}{2\pi})$$

$$J_{42} = (n_{22} r_z + m_6 m_7 m_{11}(dr_z - fr_y + \frac{gnP}{2\pi});\ \ J_{43} = m_{10}(dr_z - fr_y);\ J_{44} = \frac{gnP}{2\pi} m_{10}$$

$$J_{51} = -n_{11} r_z + m_9 m_{11}(m_5 + m_6 m_8)(fr_x - gr_z + \frac{dnP}{2\pi})$$

$$J_{52} = (-n_{12} r_z + m_6 m_7 m_{11})(fr_x - gr_z + \frac{dnP}{2\pi});J_{53} = m_{10}(fr_x - gr_z);\ J_{54} = \frac{dnP}{2\pi} m_{10}$$

$$J_{61} = (n_{11} r_y - n_{21} r_x + m_9 m_{11}(m_5 + m_6 m_8)(gr_y - dr_x + \frac{fnP}{2\pi})$$

$$J_{62} = n_{12} r_y - n_{22} r_x + m_6 m_7 m_{11}(gr_y - dr_x + \frac{fnP}{2\pi});J_{63} = m_{10}(gr_y - dr_x);\ J_{64} = \frac{fnP}{2\pi} m_{10}$$

(c.21)

Appendix D:

Derivation of Eq. (3.5)

With reference to Figure d-1a, Axis Y_1 is normal to axes X_0 and Z_0. Rotation θ_1''' transforms axis Z_0 to Z_1. Rotation θ_2''' transforms axis Z_1 to Z_2 as much as β. Therefore, it rotates vector OF_1^1 to OF_1^2 as much as β as shown in Figure d-1b. This motion happens in plane X_0Z_1. The corresponding vector $O\hat{F}_1^1$ rotates to $O\hat{F}_1^2$ as much as θ_2''' in plane X_0Z_0 as seen in Figures d-1a and d-1d. The orientation of plane Z_0X_0 with respect to plane Z_1X_0 is shown in Figure d-1c. The projections of vector OF_1^1 on axes X_0 and Z_1 are shown as OM_1^2 and ON_1^2, respectively. The projections of vector $O\hat{F}_1^2$ on axes X_0 and Z_0 are shown as OM_1^2 and $O\hat{N}_1^2$, respectively.

According to Figure d-1b, the following relationships hold:

$$OF_1^1 = OF_1^2 \tag{d.1a}$$

$$OM_1^2 = OF_1^1 \sin\beta \tag{d.1b}$$

$$ON_1^2 = OF_1^1 \cos\beta \tag{d.1c}$$

Referring to Figures d-1b, d-1c, and d-1d, we have:

$$O\hat{N}_1^2 = ON_1^2 \cos\alpha \tag{d.2}$$

Substituting Eq. (d.1c) into Eq. (d.2), we have:

$$O\hat{N}_1^2 = OF_1^1 \cos\beta \cos\alpha \tag{d.3}$$

With reference to Figure d-1d, we have the following relationship:

$$\tan\theta_2 = \frac{OM_1^2}{O\hat{N}_1^2} \tag{d.4}$$

Substituting Eqs. (d.1b) and (d.3) into Eq. (d.4), we have:

$$\tan\theta_2 = \frac{\tan\beta}{\cos\alpha} \tag{d.5}$$

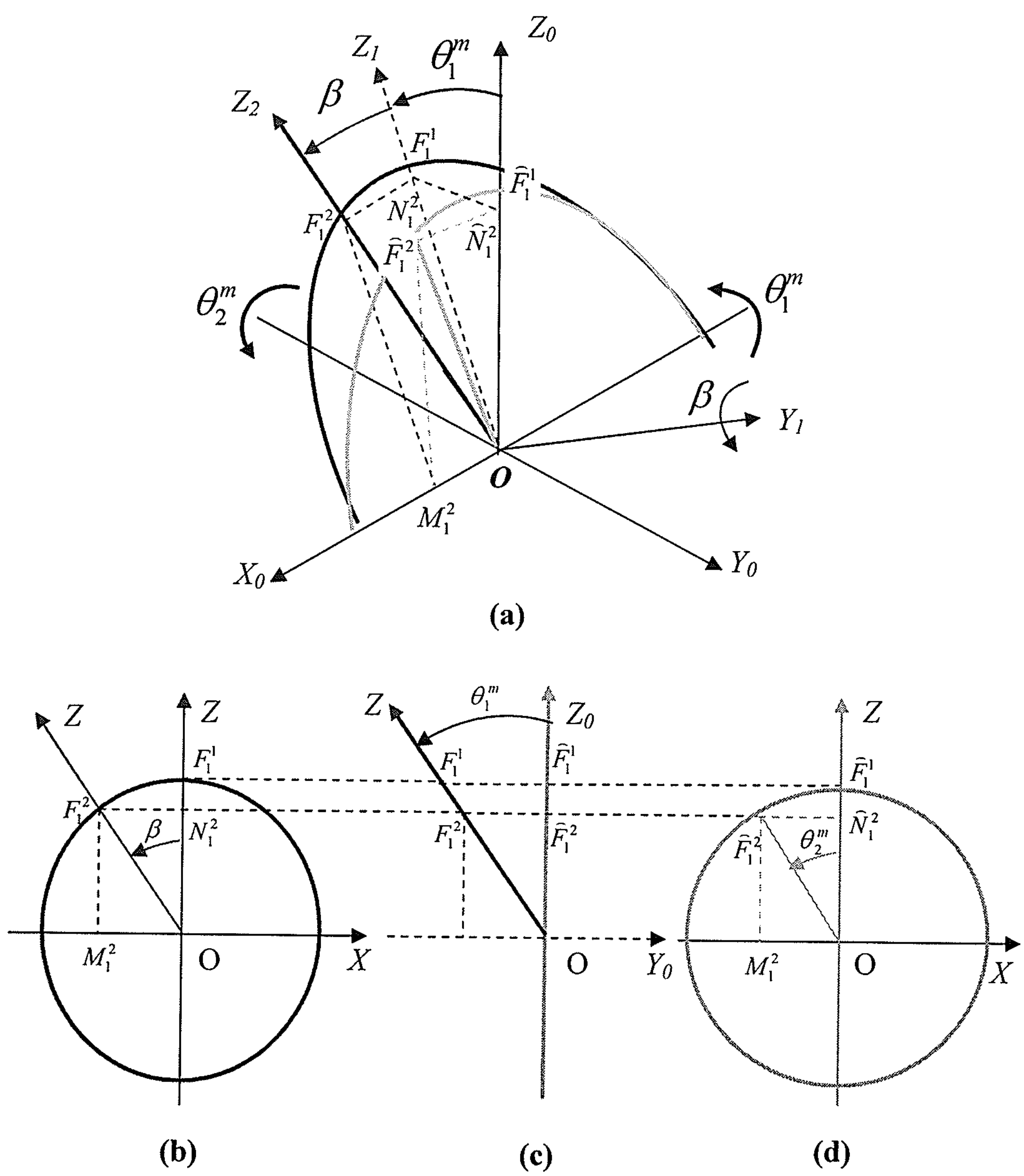

Figure d-1. (a) Relation between rotation, θ_2^m, of input link about axis Y_0 and rotation of axis Z_1, β, about axis Y_1; (b) projection on plane Z_1X_0; (c) orientation of plane Z_1X_0 with respect to plane Z_0X_0; (d) vector $O\hat{F}_1^1$ rotates as much as θ_2^m to reach to $O\hat{F}_1^2$ in plane Z_0X_0 normal to axis Y_0.

Appendix E:

Derivation of the Jacobian Matrix of the Hand-controller

With reference to Figure 3-8, the objective is to find the velocity state of the moving platform $\{X_m Y_m Z_m\}$ attached to the hand-grip given actuator velocities $\dot{\theta}_1^m$, $\dot{\theta}_2^m$, $\dot{\theta}_3^m$ and $\dot{\theta}_4^m$. The velocity vector of the moving platform $\{X_m Y_m Z_m\}$ can be described in the fixed frame $\{X_0 Y_0 Z_0\}$ as $[\vec{\omega}\ \vec{V}]^T$ where $\vec{\omega}$ and $\vec{V}$ are angular and linear velocity vectors, respectively. Note that third and fourth DoFs are kinematically decoupled from the first two DoFs generated by eight-bar mechanisms. This simplifies the derivation of the Jacobian matrix.

The angular velocity $\vec{\omega} = [\omega_X \quad \omega_Y \quad \omega_Z]^T$ of the moving platform $\{X_m Y_m Z_m\}$ attached to the hand-grip consists of two components. The first component, $\vec{\omega}_1 = [\omega_{1x} \quad \omega_{1y} \quad 0]^T$, comes from the angular motor velocities of $\dot{\theta}_1^m$ and $\dot{\theta}_2^m$ of the two eight-bar mechanism's actuators. The conventional velocity vector-loop method is used (Tsai 1999) to obtain the non-zero elements of the first component. This will be described below.

Referring to Figure e-1, a loop-closure equation can be written as:

$$\overrightarrow{OE} = \overrightarrow{OB_i} + \overrightarrow{B_iC_i} + \overrightarrow{C_iE} \qquad (i = 1,2) \qquad \text{(e.1)}$$

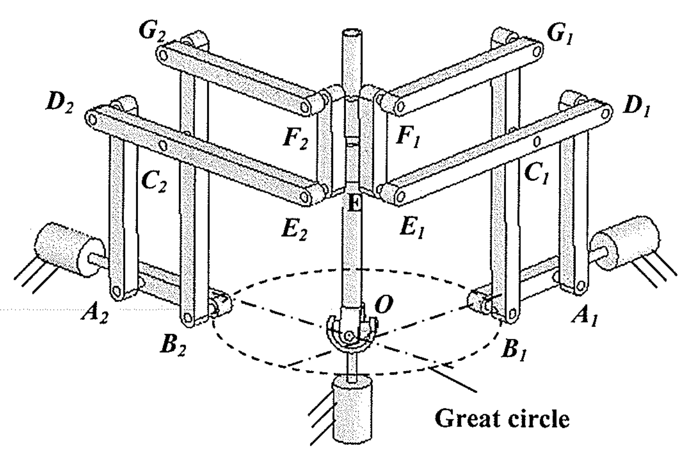

Figure e-1. Simplified structure of hand-controller.

Taking derivative of Eq. (e.1) with respect to time, yields the following velocity vector-loop equation:

$$\overrightarrow{V_E} = \overrightarrow{\omega_{B_iC_i}} \times \overrightarrow{B_iC_i} + \overrightarrow{\omega_{C_iE}} \times \overrightarrow{C_iE} \qquad (i = 1,2) \tag{e.2}$$

where $\overrightarrow{\omega_{B_iC_i}}$ and $\overrightarrow{\omega_{C_iE}}$ are the angular velocities of links B_iC_i and C_iE, respectively. In order to eliminate $\overrightarrow{\omega_{C_iE}}$ from Eq. (e.2), both sides of Eq. (e.2) are dot-multiplied by $\overrightarrow{C_iE}$.

$$\overrightarrow{C_iE} \cdot (\overrightarrow{V_E}) = (\overrightarrow{B_iC_i} \times \overrightarrow{C_iE}) \cdot \overrightarrow{\omega_{B_iC_i}} \qquad (i = 1,2) \tag{e.3}$$

Polygon OB_iC_iE is a parallelogram (see Figure e-1). Therefore, vectors $\overrightarrow{B_iC_i}$ and $\overrightarrow{C_iE}$ are equal to $\overrightarrow{OE}$ and $\overrightarrow{B_iO}$, respectively. Equation (e.3) can then be written as:

$$\overrightarrow{C_iE} \cdot (\overrightarrow{V_E}) = (\overrightarrow{OE} \times \overrightarrow{C_iE}) \cdot \overrightarrow{\omega_{OE}} \qquad (i = 1,2) \tag{e.4}$$

Referring to Eq. (3.7), vector $\overrightarrow{OE}$ in Figure e-1 is written as:

$$\overrightarrow{OE} = \begin{bmatrix} e_x & e_y & e_z \end{bmatrix}^T = e.\begin{pmatrix} s\beta \\ -c\beta\, s\theta_1^m \\ c\beta\, c\theta_1^m \end{pmatrix} \tag{e.5}$$

where $e = \sqrt{(e_x^2 + e_y^2 + e_z^2)}$ is the length of vector $\overrightarrow{OE}$ (see Figure e-1). Derivative of Eq. (e.5) will yield to the following relation:

$$\overrightarrow{V_E} = \begin{bmatrix} \dot{e}_x & \dot{e}_y & \dot{e}_z \end{bmatrix}^T = e\begin{pmatrix} \dot{\beta}\, c\beta \\ \dot{\beta}\, s\beta\, s\theta_1^m - \dot{\theta}_1^m c\beta\, c\theta_1^m \\ -\dot{\beta}\, s\beta\, c\theta_1^m - \dot{\theta}_1^m c\beta\, s\theta_1^m \end{pmatrix} \tag{e.6}$$

In fixed frame $\{X_0Y_0Z_0\}$, $\overrightarrow{C_1E} = \overrightarrow{B_1O} = \begin{bmatrix} b & 0 & 0 \end{bmatrix}^T$, $\overrightarrow{C_2E} = \overrightarrow{B_2O} = \begin{bmatrix} 0 & b & 0 \end{bmatrix}^T$ and b is the length of vector $\overrightarrow{B_iO}$. By substituting Eq. (e.6) into the left-hand side of Eq. (e.4) we will have:

$$\begin{pmatrix} \overrightarrow{C_1E}.\overrightarrow{V_E} \\ \overrightarrow{C_2E}.\overrightarrow{V_E} \end{pmatrix} = b\begin{pmatrix} \dot{e}_x \\ \dot{e}_y \end{pmatrix} = be\begin{pmatrix} \dot{\beta}\, c\beta \\ \dot{\beta}\, s\beta\, s\theta_1^m - \dot{\theta}_1\, c\beta\, c\theta_1^m \end{pmatrix} = \begin{pmatrix} l_{11} & l_{12} \\ l_{21} & l_{22} \end{pmatrix}\begin{pmatrix} \dot{\theta}_1^m \\ \dot{\theta}_2^m \end{pmatrix} \qquad \text{(e.7)}$$

where $\dot{\beta}$ is obtained from the derivative of Eq. (3.5):

$$\dot{\beta} = c^2\beta\,(-\dot{\theta}_1^m s\theta_1^m t\theta_2^m + \dot{\theta}_2^m \frac{c\theta_1^m}{c^2\theta_2^m})$$

and

$$l_{11} = -be\, c^3\beta\, s\theta_1^m\, t\theta_2^m$$

$$l_{12} = \frac{be\, c^3\beta\, c\theta_1^m}{c^2\theta_2^m}$$

$$l_{21} = -be\, c^2\beta\, s\beta\, s^2\theta_1^m\, t\theta_2^m - c\beta\, c\theta_1^m$$

$$l_{22} = \frac{be\, c^2\beta\, s\beta\, s\theta_1^m c\theta_1^m}{c^2\theta_2^m}$$

The right-hand side of Eq. (e.4) can be written as:

$$(\overrightarrow{OE}\times\overrightarrow{C_iE}).\overrightarrow{\omega_{OE}} = \begin{pmatrix} (\overrightarrow{OE}\times\overrightarrow{C_1E})^T \\ (\overrightarrow{OE}\times\overrightarrow{C_2E})^T \end{pmatrix}\begin{pmatrix} \omega_{1x} \\ \omega_{1y} \\ 0 \end{pmatrix} = \begin{pmatrix} r_{11} & r_{12} \\ r_{21} & r_{22} \end{pmatrix}\begin{pmatrix} \omega_{1x} \\ \omega_{1y} \end{pmatrix} \qquad \text{(e.8)}$$

where

$$r_{11} = 0$$

$$r_{12} = be\, c\beta\, c\theta_1^m$$

$$r_{21} = -be\, c\beta\, c\theta_1^m$$

$$r_{22} = 0$$

Equating right-hand sides of Eqs. (e.7) and (e.8), we will have:

$$\begin{pmatrix} \omega_{1x} \\ \omega_{1y} \end{pmatrix} = \begin{pmatrix} r_{11} & r_{12} \\ r_{21} & r_{22} \end{pmatrix}^{-1}\begin{pmatrix} l_{11} & l_{12} \\ l_{21} & l_{22} \end{pmatrix}\begin{pmatrix} \dot{\theta}_1^m \\ \dot{\theta}_2^m \end{pmatrix} = \begin{pmatrix} n_{11} & n_{12} \\ n_{21} & n_{22} \end{pmatrix}\begin{pmatrix} \dot{\theta}_1^m \\ \dot{\theta}_2^m \end{pmatrix} \qquad \text{(e.9)}$$

where

$$n_{11} = \frac{r_{22}l_{11} - r_{12}l_{21}}{r_{11}r_{22} - r_{12}r_{21}},\ n_{12} = \frac{r_{22}l_{12} - r_{12}l_{22}}{r_{11}r_{22} - r_{12}r_{21}},\ n_{21} = \frac{r_{11}l_{21} - r_{21}l_{11}}{r_{11}r_{22} - r_{12}r_{21}},\ n_{22} = \frac{r_{11}l_{22} - r_{21}l_{12}}{r_{11}r_{22} - r_{12}r_{21}}$$

The second component of $\vec{\omega}$, $\vec{\omega}_2 = \begin{bmatrix}\omega_{2x} & \omega_{2y} & \omega_{2z}\end{bmatrix}^T$, comes from the rotational velocity $\dot{\theta}_4^m$ of the hand-grip. The rotational velocity has projections on the axes of frame $\{X_0 Y_0 Z_0\}$. These projections can be obtained by the following equation:

$$\begin{bmatrix}\omega_{2x} & \omega_{2y} & \omega_{2z}\end{bmatrix}^T = Rot(X_0, \theta_1^m) Rot(Y_1, \beta) \begin{bmatrix}0 & 0 & \dot{\theta}_4^m\end{bmatrix}^T = \begin{bmatrix}\dot{\theta}_4^m s\beta \\ -\dot{\theta}_4^m \, c\beta \, s\theta_1^m \\ \dot{\theta}_4^m \, c\beta \, c\theta_1^m\end{bmatrix} \qquad \text{(e.10)}$$

The rotation matrices $Rot(X_0, \theta_1^m)$ and $Rot(Y_1, \beta)$ are given in Eqs. (3.3) and (3.4). Combining Eqs. (e.9) and (e.10), one can determine the angular velocity vector $\vec{\omega}$:

$$\vec{\omega} = \begin{bmatrix}\omega_X & \omega_Y & \omega_Z\end{bmatrix}^T = \begin{pmatrix} n_{11}\,\dot{\theta}_1^m + n_{12}\,\dot{\theta}_2^m + m_1\,\dot{\theta}_4^m \\ n_{21}\,\dot{\theta}_1^m + n_{22}\,\dot{\theta}_2^m + m_2\,\dot{\theta}_4^m \\ m_3\,\dot{\theta}_4^m \end{pmatrix} \qquad \text{(e.11)}$$

where

$m_1 = s\beta$

$m_2 = -c\beta \, s\theta_1^m$

$m_3 = c\beta \, c\theta_1^m$

The linear velocity vector $\vec{V} = \begin{bmatrix}V_X & V_Y & V_Z\end{bmatrix}^T$ of frame $\{X_m Y_m Z_m\}$ attached to the hand-grip has two components. The first component, $\vec{V}_1 = \begin{bmatrix}V_{1x} & V_{1y} & V_{1z}\end{bmatrix}^T$, is due to angular velocity $\vec{\omega}$ of moving platform $\{X_m Y_m Z_m\}$:

$$\begin{bmatrix}V_{1x} & V_{1y} & V_{1z}\end{bmatrix}^T = \vec{\omega} \times \vec{r} = \begin{bmatrix}(\omega_y r_z - \omega_z r_y) & (\omega_z r_x - \omega_x r_z) & (\omega_x r_y - \omega_y r_x)\end{bmatrix}^T \qquad \text{(e.12)}$$

where $\vec{r} = \begin{bmatrix} r_x & r_y & r_z \end{bmatrix}^T$ is the vector describing the distance between frames $\{X_0 Y_0 Z_0\}$ and $\{X_m Y_m Z_m\}$ in fixed frame $\{X_0 Y_0 Z_0\}$.

$$\vec{r} = \begin{bmatrix} r_x & r_y & r_z \end{bmatrix}^T = Rot(X_0, \theta_1^m) Rot(Y_1, \beta) \begin{bmatrix} 0 & 0 & r \end{bmatrix}^T = \begin{pmatrix} r\, s\beta \\ -r\, c\beta\, s\theta_1^m \\ r\, c\beta\, c\theta_1^m \end{pmatrix} \qquad \text{(e.13)}$$

By substituting Eqs. (3.8), (e.11) and (e.13) into Eq. (e.12) and some mathematical manipulation, we will have:

$$\begin{bmatrix} V_{1x} & V_{1y} & V_{1z} \end{bmatrix}^T = \begin{pmatrix} m_4\, \dot{\theta}_1^m + m_5\, \dot{\theta}_2^m \\ m_6\, \dot{\theta}_1^m + m_7\, \dot{\theta}_2^m \\ m_8\, \dot{\theta}_1^m + m_9\, \dot{\theta}_2^m \end{pmatrix} \qquad \text{(e.14)}$$

where

$$m_4 = \frac{d_3\, \theta_3^u\, n_{21}\, c\beta\, c\theta_1}{2}$$

$$m_5 = \frac{d_3\, \theta_3^u\, n_{22}\, c\beta\, c\theta_1}{2}$$

$$m_6 = -\frac{d_3\, \theta_3^u\, n_{11}\, c\beta\, c\theta_1}{2}$$

$$m_7 = -\frac{d_3\, \theta_3^u\, n_{12}\, c\beta\, c\theta_1}{2}$$

$$m_8 = -\frac{d_3\, \theta_3^u}{2}(n_{11}\, c\beta\, s\theta_1^m + n_{21}\, s\beta)$$

$$m_9 = -\frac{d_3\, \theta_3^u}{2}(n_{12}\, c\beta\, s\theta_1^m + n_{22}\, s\beta)$$

The second component of $\vec{V}$, $\vec{V}_2 = \begin{bmatrix} V_{2x} & V_{2y} & V_{2z} \end{bmatrix}^T$, is the result of linear velocity $\dot{\vec{r}}$ of frame $\{X_m Y_m Z_m\}$ attached to the hand-grip. This linear velocity has projections on the axes of frame $\{X_0 Y_0 Z_0\}$:

$$[V_{2x} \quad V_{2y} \quad V_{2z}]^T = Rot(X_0, \theta_1^{m})Rot(Y_1, \beta)[0 \quad 0 \quad \dot{r}]^T = \begin{bmatrix} \dot{r}\, s\beta \\ -\dot{r}\, c\beta\, s\theta_1^{m} \\ \dot{r}\, c\beta\, c\theta_1^{m} \end{bmatrix} \qquad \text{(e.15)}$$

where $\dot{r}$ is obtained from combined derivative of Eqs. (3.8), (3.9), and (3.10). Therefore, $\overrightarrow{V_2}$ can be determined by the following relation:

$$[V_{2x} \quad V_{2y} \quad V_{2z}]^T = \begin{pmatrix} m_{10}\,\dot{\theta}_1^{m} + m_{11}\,\dot{\theta}_2^{m} + m_{12}\,\dot{\theta}_3^{m} \\ m_{13}\,\dot{\theta}_1^{m} + m_{14}\,\dot{\theta}_2^{m} + m_{15}\,\dot{\theta}_3^{m} \\ m_{16}\,\dot{\theta}_1^{m} + m_{17}\,\dot{\theta}_2^{m} + m_{18}\,\dot{\theta}_3^{m} \end{pmatrix} \qquad \text{(e.16)}$$

where

$$m_{10} = -\frac{d_3\, s\beta\, c\beta\, c^2\theta_3^{u}\, t\theta_3\, s\theta_1^{m}}{2}(-c\beta\, s\beta\, c\theta_1^{m}\, t\theta_2^{m} + 1)$$

$$m_{11} = -\frac{d_3\, s^2\beta\, c^2\beta\, c^2\theta_3^{u}\, t\theta_3\, c^2\theta_1^{m}}{2\, c^2\theta_2^{m}}$$

$$m_{12} = \frac{d_3\, c\psi\, s\beta\, c^2\theta_3^{u}}{2\, c^2\theta_3^{m}}$$

$$m_{13} = \frac{d_3\, c^2\beta\, c^2\theta_3^{u}\, t\theta_3\, s^2\theta_1^{m}}{2}(-c\beta\, s\beta\, c\theta_1^{m}\, t\theta_2^{m} + 1)$$

$$m_{14} = \frac{d_3\, c^3\beta\, s\beta\, c^2\theta_3^{u}\, t\theta_3\, s\theta_1^{m}\, c^2\theta_1^{m}}{2\, c^2\theta_2^{m}}$$

$$m_{15} = -\frac{d_3\, c\psi\, c\beta\, c^2\theta_3^{u}}{2\, c^2\theta_3}$$

$$m_{16} = -\frac{d_3\, c^2\beta\, c^2\theta_3^{u}\, t\theta_3\, s\theta_1^{m}\, c\theta_1^{m}}{2}(-c\beta\, s\beta\, c\theta_1^{m}\, t\theta_2^{m} + 1)$$

$$m_{17} = -\frac{d_3\, c^3\beta\, s\beta\, c^2\theta_3^{u}\, t\theta_3\, c^3\theta_1^{m}}{2\, c^2\theta_2^{m}}$$

$$m_{18} = \frac{d_3\, c\psi\, c\beta\, c^2\theta_3^{u} c\theta_1^{m}}{2\, c^2\theta_3}$$

$$\theta_3 = \frac{\theta_3^{m}}{n}$$

Adding the right-hand sides of Eqs. (e.14) and (e.16), we will have:

$$\vec{V} = [V_X \quad V_Y \quad V_Z]^T = \begin{pmatrix} V_{1x} + V_{2x} \\ V_{1y} + V_{2y} \\ V_{1z} + V_{2z} \end{pmatrix} = \begin{pmatrix} (m_4 + m_{10})\dot{\theta}_1^m + (m_5 + m_{11})\dot{\theta}_2^m + m_{12}\dot{\theta}_3^m \\ (m_6 + m_{13})\dot{\theta}_1^m + (m_7 + m_{14})\dot{\theta}_2^m + m_{15}\dot{\theta}_3^m \\ (m_8 + m_{16})\dot{\theta}_1^m + (m_9 + m_{17})\dot{\theta}_2^m + m_{18}\dot{\theta}_3^m \end{pmatrix} \tag{e.17}$$

Considering Eqs. (e.20) and (e.26) together, the Jacobian matrix can be found from the following relation:

$$\begin{bmatrix} \vec{\omega} & \vec{V} \end{bmatrix}^T_{(6\times1)} = [J]_{6\times4} \begin{bmatrix} \dot{\theta}_1^m & \dot{\theta}_2^m & \dot{\theta}_3^m & \dot{\theta}_4^m \end{bmatrix}^T \tag{e.18}$$

where

$J_{11} = n_{11}$; $J_{12} = n_{12}$; $J_{13} = 0$; $J_{14} = m_1$

$J_{21} = n_{21}$; $J_{22} = n_{22}$; $J_{23} = 0$, $J_{24} = m_2$

$J_{31} = 0$; $J_{32} = 0$; $J_{33} = 0$; $J_{34} = m_3$

$J_{41} = m_4 + m_{10}$; $J_{42} = m_5 + m_{11}$; $J_{43} = m_{12}$; $J_{44} = 0$

$J_{51} = m_6 + m_{13}$; $J_{52} = m_7 + m_{14}$; $J_{53} = m_{15}$; $J_{54} = 0$

$J_{61} = m_8 + m_{16}$; $J_{62} = m_9 + m_{17}$; $J_{63} = m_{18}$; $J_{64} = 0$

Appendix F:

Technical Specifications of the Wrist and Haptic Device

Technical specifications of 4-DoF robotic wrist				
	Range of motion	**Motor**	**Gear ratio**	**Motor torque/force**
Yaw axis	± 25°	Maxon RE 36	111:1	88.5 mNm
Pitch axis	± 25°	Maxon RE 36	111:1	88.5 mNm
Rotational axis	± 90°	Maxon RE 25	84:1	29.3 mNm
Palpation axis	32 mm	Maxon RE 25	84:1	24 N (measured)
Footprint & height	(192 mm × 192 mm) and 750 mm			
Encoders resolutions	0.18 deg			
Weight of moving elements	2.5 kg			
Force sensor	LCMKD 50 N, by Omega			

Technical specifications of 4-DoF haptic device				
	Range of motion	**Motor**	**Cable reducer ratio**	**Motor torque/force**
Yaw axis	± 35°	-	-	-
Pitch axis	± 35°	-	-	-
Rotational axis	± 30°	-	-	-
Palpation axis	32 mm	Maxon RE 26	5:1	29.3 mNm
Footprint & height	(232 mm × 232 mm) and 280 mm			
Encoder resolutions	0.7 deg			
Weight of moving elements	452 gr			
Static balancing	With one tension spring with stiffness 0.4×10^{-3} kg/mm			
Static-friction break away force	0.26 N			

References

Agrawal, S.K., Gardner, G. and Pledgie, S. (2001). Design and fabrication of an active gravity balanced planner mechanism using auxiliary parallelograms. *ASME Transactions on Mechanical Design*, 123: 525-528.

Artobolevsky, I.I. (1979). Mechanisms in Modern Engineering Design. Moscow, Mir Publishers.

Anderson, R. J. and Spong, M.W. (1989). Bilateral control of teleoperators with time delay. *IEEE Transaction on Automatic Control,* 34(5): 694-501.

Asada, H. and CorGranito, J.A. (1985). Kinematic and static characterization of wrist joints and their optimal design. In *Proceedings of the IEEE International conference on Robot and Automata*, pp. 244-250.

Bassan, H., Hayes, T., Patel, R.V. and Moallem M. (2007). A novel manipulator for 3D ultrasound guided percutaneous needle insertion. In *Proceedings of the IEEE International Conference on Robotics and Automation,* pp. 10-14.

Baumann, R., Maeder, W., Glauser, D. and Claval, R. (1997). The PantoScope: a spherical remote-center-of-motion parallel manipulator for force reflection. In *Proceedings of the IEEE International Conference on Robotics and Automation*, pp. 718-723.

Bevrit, J., Moore, D.F, Norwood, J.Q., Rosenberg, L.B. and Levin, M.D. (2000). Hemispherical, high bandwidth mechanical interface for computer systems. US patent No. 6,024,576.

Birglen L, Gosselin C. and Pouliot N. (2002). ShaDe, a new 3-DOF haptic device. *IEEE Transactions on Robotics and Automation,* 18(2): 166-175.

Brooks and Thurston, L. (1990). Telerobotic response requirements. In *Proceedings of the IEEE International Conference on Systems, Man and Cybernetics*, pp. 113-120.

Carricato, M. and Castelli, V.P. (2004). A novel decoupled two-degrees-of-freedom parallel wrist. *International Journal of Robotics Research*, 23(6), 661-667.

Cavusoglu, M.C., Tendick, M.C. and Sastry, S.Sh. (1999). A laparoscopic telesurgical workstation. *IEEE Transactions on Robotics and Automation*, 15(4): 728-739.

Daniel, P.F., Siva, K.V. (1990). Specification and design ofl input devices for tele-operation. In *Proceedings of the IEEE International Conference on Robotics and Automation*, pp. 540-545.

Degoulange, E., Urbain, L., Caron, P., Boudet, S., Megnien, J.L., Pierrot, F. and Dombre, E. (1998). HIPROCRATE: an intrinsically safe robot for medical applications. In *Proceedings of the IEEE/RSJ, International Conference on Intelligent Robots and Systems*, pp. 959-964.

Delgorge, C., Courreges, F., Bassit, L.A., Novales, C., Rosenberger, C., Smith-Guerin, N., Bru, C., Gilabert, R., Vannoni, M., Poisson, G. and Vieyres, P. March. (2005). A tele-operated mobile ultrasound scanner using a light weight robot. *IEEE Transaction on Information Technology in Biomedicine,* 9(1): 50-58.

Duriez, Ch., Lamy, D. and Chaillou, Ch. (2001). A parallel manipulator as a haptic interface solution for amniocentesis simulation. In *Proceedings of the IEEE International Workshop on Robot and Human Interactive Communication*, pp. 176-181.

Faraz, A. and Payandeh, Sh. (1998). A robotic case study: Optimal design for laparoscopic positioning stands. *International Journal of Robotics Research,* 17(9): 986-995.

Fenster, A. and Downey, D.B. (1996). 3-D ultrasound imaging: a review. *IEEE Engineering in Medicine and Biology,* 15(6): 41-51.

Funda, J. and LaRose, D.A. and Taylor, H.T. (2001). US patent No. 6,201,984.

Gonzales, A., et al. (2001). TER: A system for robotic tele-echography. In *Proceedings of the International Conference of Medical Image Computing and Computer Assisted Intervention*, pp. 326-334.

Gosselin, C.M. and Hamel, J.F. (1994). The Agile Eye: A high performance three-degree-of-freedom camera-orienting device. In *Proceedings of the IEEE International conference on Robot and Automata*, pp. 781-786.

Gosselin, C.M. (1999). Static balancing of spherical 3-DoF parallel mechanisms and manipulators. *The International Journal of Robotics Research,* 18(8): 819-829.

Gosselin, C.M. and Wang, J. (2000). Static balancing of spatial six-degree-of-freedom parallel mechanisms with revolute actuators. *Journal of Robotic Systems*, 17(3): 159-170.

Gourdon, A., Poignet, Ph., Poisson, G., Vieyres, P. and Marche, P. (1998). A new robotic mechanism for medical application. In *Proceedings of the IEEE/ASME International. Conference on Advanced Intelligent Mechatronics*, pp. 33-38.

Guerin, N. S., Bassit, L. Al., Poisson, G., Delgorge, C., Arbeille, P. and Vieyres P. (2003). Clinical validation of a mobile patient-expert tele-echography system using ISDN lines. In *Proceedings of the IEEE-EMBS Information Technology Applications in Biomedicine [ITAB]*, pp. 23-26.

Hamlin, G.J. and Sanderson, A.C. (1994). A novel concentric multilink spherical joint with parallel robotics applications. In *Proceedings of the IEEE International Conference on Robotics and Automation*, pp. 1267-1272.

Hayward, V. (1995). Toward a seven axis haptic device. In *Proceedings of the IEEE International. Conference on Intelligent Robots and Systems 'Human Robot Interaction and Cooperative Robots'*, pp. 133-139.

Hayward, V., Gregorio, P., Astley, O., Greenish, S., Doyon, M., Lessard, L., McDougall, J., Sinclair, I., Boelen, S., Chen, X., Demers, J.P., Poulin, J., Benguigui, I., Almey, N., Makuc, B. and Zhang, X. (1998). Freedom-7: A high fidelity seven axis haptic device with application to surgical training. In *Proceedings of the Experimental Robotics V, Casals, A., de Almeida, A. T. (eds.), Lecture Notes in Control and Information Science*, pp. 445-456.

Herder, J.L. (2002). Some considerations regarding statically balanced parallel mechanisms. *Workshop on Fundamental Issues and Future Research Directions for Parallel Mechanisms and Manipulators*, pp. 40-45.

Hinkle, R. (1960). Kinematics of Machines. second edition, New Jercy, Prentice-Hall, Inc.

Hong, B. and Erdman, A.G. (2002). Spherical linkage apparatus, US patent No. 6,355,048.

Ikta, k. and Nokata, M. (1999). General evaluation method of safety for human-care robots. In *Proceedings of the IEEE International Conference on Robotics and Automation*, pp. 2065-2072.

Ishida, T., Takanishi, A. (2006). A robot actuator development with high backdriveability. 2006. In *Proceedings of the IEEE Conference on Robotics, Automation and Mechatronics,* pp.1-6.

Johnson, D.A. and Willems, P.Y. (1993). On the necessary and sufficient conditions for homokinetic transmission in chains of cardan joints. *ASME Journal of Mechanical Design,* 115: 255-261.

Khodabandehloo, K., Brett, P. N. and Buckingham, R.O. (2003). Computer Integrated Surgery: Technology and Clinical Application, "Special purpose actuators and architecture for surgery robots". Cambridge, MA, MIT press.

Kobayashi, K. (2001). New design method for spring balancers. *ASME Transactions on Mechanical Design*, 123: 494-500.

Koizumi, N., Warisawa, Sh., Hashizume, H. and Mitsuishi, M. (2008). Continuous path controller for remote ultrasound diagnostic system. *IEEE Transactions on Mechatronics*, 13(2), 206-218.

Kontaxakis, G., Walter, S. and Sakas, G. (2000). EU-TeleInViVo: an integrated portable telemedicine workstation featuring acquisition, processing and transmission over low-bandwidth lines of 3D ultrasound volume images. In *Proceedings of the IEEE EMBS International Conference on Information Technology Applications in Biomedicine*, pp. 158-163.

Kuleshov, V.S. and Lakota, N.A. (1988). Remotely Controlled Robots and Manipulators. Moscow, Mir Publishers.

Lee, D., Spong, M.W. (2006). Passive bilateral teleoperation with constant time delay. *IEEE Transactions on Robotics,* 22(2): 269-281.

Lee, J.H, Eom, K.S., Yi B.J. and Suh, I.H. (2001). Design of a new 6 DOF parallel haptic device. In *Proceedings of the IEEE International Conference on Robotics and Automation*, pp. 886-891.

Madhani, A.J., Niemeyer, G. and Salisbury, K. (1998). The Black Falcon: A teleoperated surgical instrument for minimally invasive surgery. In *Proceedings of the IEEE/RSJ International Conference on Intelligent Robots and Systems*, pp. 936-944.

Madhani, A.J. (1998). Design of teleoperated surgical instruments for minimally invasive surgery. Ph.D thesis, Department of Mechanical Engineering, MIT.

Marchal, M and Troccaz, J. (2004). A One-DOF Free-Hand Haptic Device for Robotic Tele-Echography. In *Proceedings of the International Conference Medicine Meets Virtual Reality (MMVR'12), Studies in Health Technology and Informatics Series*, pp.231-233.

Mason, M.T. and Salisbury, J.K. (1985). Robot Hands and the Mechanics of Manipulation. Cambridge, MA, MIT Press.

Massie, Th.H. and Salisbury, K. (1996). Force reflecting haptic interface. US patent No. 5,587,937.

Masuda, K., Kimura, E., Tateishi, N. and Ishihara, K. (2001). Three dimensional motion mechanism of ultrasound probe and its application for tele-echography system. In *Proceedings of the IEEE/RSJ, International Conference on Intelligent Robots and Systems*, pp. 1112-1116.

Mitsubishi, M., Warisawa, Sh., Tsuda, T., Higuchi, T., Koizumi, N., Hashizume, H. and Fujiwara K. (2001). Remote ultrasound diagnosis system. In *Proceedings of the IEEE International Conference on Robotics and Automation*, pp.1567-1574.

Morita, T. and Sugano, Sh. (1995). Design and development of a new robot joint using a mechanical impedance adjuster. In *Proceedings of the IEEE International Conference on Robotics and Automation,* pp. 2469-2475.

Muradali, D., Gold, W.L., Phillips, A. and Wilson, S. (1995). Can ultrasound probes and coupling gel be a source of nosocomial infection in patients undergoing sonography? An in vivo and in vitro study. *American Journal of Roentgenology,* 164: 1521-1524.

Najafi, F. (2004). Design and prototype of a robotic system for remote palpation and ultrasound imaging. M.Sc. thesis, Department of Mechanical and Manufacturing Engineering, University of Manitoba.

Najafi, F. and Sepehri N. (2007). Hand controller and wrist device. US patent No. 7,204,168.

Najafi, F. and Sepehri N. (2008). A novel hand-controller for remote ultrasound imaging. *Mechatronics*, 18(10): 578-590.

Niemeyer, G. and Slotine, J. (1991). Stable adaptive teleoperation. *IEEE Journal of Oceanic Engineering,* 16(1): 152-162.

Orlov, P. (1979). Fundamentals of Machine Design. Moscow, Mir Publishers.

Ouerfelli, M. and Kumar, V. (1994). Optimization of a spherical five-bar parallel drive linkage. *ASME Journal of Mechanical Design,* 116: 166-173.

Park, K. S., Kenyon, R. V. (1999). Effects of Network Characteristics on Human Performance in a Collaborative Virtual Environment. In *Proceedings of IEEE Virtual Reality Conference, Houston*, pp. 104-111.

Poignet, P., Dombre, E., Merigeaux, O. and Pierrot, F. (2003). Design and control issues for intrinsically safe medical robot. *Industrial Robot: An International Journal,* 30(1): 83-88.

Popov, E.P. (1976). Mechanics of Materials. New York, Prentice Hall.

Proakis, J.G. and Manolakis, D.G. (2007). Digital Signal Processing: Principals, Algorithms, and Applications. New Jersey, Pearson and Prentice Hall.

Rivin, E.I. (1988). Mechanical Design of Robots. New York, McGraw-Hill.

Rosheim, M.E. (1989). Robot Wrist Actuators. New York, John Wiley & Sons.

Salcudean, S.E., Zhu, W.H., Abolmaesumi, P., Bachmann, S. and Lawrence, P.D. (2000). A Robot System for Medical Ultrasound. In *Proceedings of the 9th International Symposium of Robotics Research (ISRR'99)*, pp. 195-202.

Sclater, N. and Chironis, N.P. (2001). Mechanisms and Mechanical Devices Sourcebook. New York, McGraw-Hill.

Sheridan, Th. B. (1992). Telerobotics, Automation, and Human Supervisory Control. Cambridge, MA, MIT Press.

Stanisic, M. M. and Duta, O. (1990). Symmetrically actuated double pointing systems–the basis of singularity free wrists. *IEEE Transaction on Robotics and Automation*, 6(5): 562-569.

Steger, R., Lin, K., Adelstein, B.D. and Kazerooni, H. (2004). Design of passively balanced spatial linkage haptic interface. *ASME Transactions on Mechanical Design*, 126: 984-991.

Stocco, L.J, Salcudean, S.E. and Sassani, F. (2001). Optimal kinematic design of a haptic pen. *IEEE/ASME transactions on Mechatronics*, 6(3): 210-220.

Sublett, J.W., Dempsey, B.J. and Weaver. (1995). Design and implementation of a digital tele-ultrasound system for real-time remote diagnosis. In *Proceedings of the IEEE Symposium on Computer-Based Medical System*, pp. 292-298.

Tahmasebi, A.M., Hashtrudi-Zad, K., Thompson, D. and Abolmaesumi, P. (2008). A framework for the design of a novel haptic-based medical training simulator. *IEEE Transactions on Information Technology in Biomedicine*, 12(5): 658-666.

Taylor, R.H., Funda, J. Grossman, D.D., Karidis, J.P. and Larose, D.A. (1995). US patent No. 5,397,323.

Taylor, R. and Stoianovici, D. (2003). Medical Robotics in Computer-Integrated Surgery. *IEEE Transactions on Robotics and Automation,* 19(5): 765-781.

Tidwell, P.H., Bandukwala, N., Dhande, S.G. and Reinholtz, C.F. (1994). Synthesis of Wrapping Cams. *ASME Transactions on Mechanical Design*, 116: 634-638.

Townsend, W.T. and Salisbury, J.K. (1988). The efficiency limit of belt and cable drives. *ASME Journal of Mechanisms, Transmissions, and Automation in Design,* 110: 303-307.

Tsai, L.W. (1999). Robot Analysis: The Mechanics of Serial and Parallel Manipulators. New York, John Wiley and Sons.

Vischer, P. and Clavel, R. (2000). Argos: A novel 3-DoF parallel wrist mechanism. *International Journal of Robotics Research,* 19(1): 5-11.

Vlachos, K., Papadopoulos, E. and Mitropoulos, D.N. (2003). Design and implementation of a haptic device for training in urological operations. *IEEE Transactions on Robotics and Automation,* 19(5): 801-809.

Vilchis, J., Troccaz, P., Cinquin, K., Masuda, F. and Pellissier. (2003). A new robot architecture for tele-echography. *IEEE Transaction. on Robotics and Automation, Special issue on Medical Robotics,* 119(5): 922-926.

Vilchis, G. A., Avila-Vilchis, J.C. and García-Torres, A. (2007). TERMI robot. *Fourth Congress of Electronics, Robotics and Automotive Mechanics*, pp. 464-469.

Wang, J. and Gosselin, C.M. (1999). Static balancing of spatial three-degree-of-freedom parallel mechanisms. *Mechanism and Machine Theory,* 34: 437-452.

Wang, J. and Gosselin, C.M. (2000). Static balancing of spatial four-degree-of-freedom parallel mechanisms. *Mechanism and Machine Theory,* 35: 563-592.

Wiitala, J. and Stanisic, M. M. (2000). Design of an overconstrained and dexterous spherical wrist. *ASME Journal of Mechanical Design,* 122: 347-353.

Xi, N. and Tarn, T.J. (2000). Stability analysis of non-time referenced internet-based telerobotic systems. *Robotics and Autonomous Systems,* 32: 173-178.

Yoon, J. and Ryu, J. (2001). Design, fabrication, and evaluation of a new haptic device using a parallel mechanism. *IEEE/ASME Transactions on Mechatronics,* 6(3): 221-230.